



**UNIVERSIDADE FEDERAL DO PARÁ  
INSTITUTO DE GEOCIÊNCIAS  
PROGRAMA DE PÓS-GRADUAÇÃO EM GEOLOGIA E GEOQUÍMICA**

**TESE DE DOUTORADO Nº 153**

**ACÚMULO E EXPORTAÇÃO DE CARBONO, NITROGÊNIO,  
FÓSFORO E METAIS EM CANAIS DE MARÉ DOS MANGUE-  
ZAIOS DE MARAPANIM, COSTA NORTE BRASILEIRA**

Tese apresentada por:

**CHRISTIENE RAFAELA LUCAS DE MATOS**  
Orientador: Prof. Dr. Marcelo Cancela Lisboa Cohen (UFPA)  
Coorientador: Dr. José Francisco Berrêdo Reis da Silva (MPEG)

---

**BELÉM - PA  
2020**

**Dados Internacionais de Catalogação na Publicação (CIP) de acordo  
com ISBD Sistema de Bibliotecas da Universidade Federal do Pará  
Gerada automaticamente pelo módulo Ficat, mediante os dados fornecidos  
pelo(a) autor(a)**

---

M425a Matos, Christiene Rafaela Lucas de

Acúmulo e exportação de carbono, nitrogênio, fósforo e metais em canais de maré dos manguezais de Marapanim, Costa Norte Brasileira / Christiene Rafaela Lucas de Matos. — 2020.  
xi, 91 f. : il. color.

Orientador(a): Prof. Dr. Marcelo Cancela Lisboa Cohen Coorientador(a): Prof. Dr. José F. Berrêdo  
Tese (Doutorado) - Programa de Pós-Graduação em Geologia e Geoquímica, Instituto de Geociências, Universidade Federal do Pará, Belém, 2020.

1. Diagênese recente. 2. Fontes de matéria orgânica. 3. Condições redox. 4. Fluxos difusivos. 5. Água intersticial. I. Título.

---

CDD 558.11



**Universidade Federal do Pará**  
**Instituto de Geociências**  
Programa de Pós-Graduação em Geologia e Geoquímica

**ACÚMULO E EXPORTAÇÃO DE CARBONO, NITROGÊNIO,  
FÓSFORO E METAIS EM CANAIS DE MARÉ DOS  
MANGUE-ZAIS DE MARAPANIM, COSTA NORTE  
BRASILEIRA**

**TESE APRESENTADA POR:**

**CHRISTIENE RAFAELA LUCAS DE  
MATOS**

**Como requisito parcial à obtenção do Grau de Doutora em Ciências na Área de GEOLOGIA e Linha de Pesquisa em GEOLOGIA MARINHA E COSTEIRA**

Data de Aprovação: 18 / 12 / 2020

Banca Examinadora:

Prof. Dr. Marcelo Cancela L. Cohen  
Orientador – UFPA

Prof. Dr. Paulo César Fonseca Giannini  
Membro – USP

Prof. Dr. Luiz Carlos Ruiz Pessenda  
Membro – USP

Prof. Dr. José Augusto Martins Corrêa  
Membro – UFPA

Prof. Dr. Nils Edvin Asp Neto  
Membro – UFPA

Ao querido,  
Professor Berrêdo

## AGRADECIMENTOS

À Universidade Federal do Pará, através do excelente programa de Pós-Graduação em Geologia e Geoquímica do Instituto de Geociências pela oportunidade de realizar este doutorado, pela utilização de sua infraestrutura, laboratórios, e em especial por disponibilizar sala para alunos, a qual foi fundamental para o desenvolvimento desta tese.

O presente trabalho foi realizado com o apoio da Coordenação de Aperfeiçoamento de Pessoal de Nível Superior – Brasil (CAPES) – Código de Financiamento 001. Agradeço a esta instituição pelo apoio financeiro, e pela concessão da bolsa PDSE que foi importante para a conclusão de parte desta tese e para minha formação como pesquisadora.

Ao Conselho Nacional de Desenvolvimento Científico e Tecnológico (CNPq) pela concessão da bolsa de doutorado. Agradeço esta instituição tão importante para realização deste trabalho, incluindo a taxa de bancada que viabilizou a compra de material para laboratório e campo, participação em congresso, dentre outros.

Ao pesquisador Dr. Berrêdo do Museu Paraense Emílio Goeldi quem primeiramente idealizou esse trabalho comigo. Obrigada por ter depositado sua confiança em mim, me incentivando e me orientando desde o início da minha vida acadêmica até agora como meu coorientador no doutorado, contribuindo significantemente em cada uma das fases da minha vida acadêmica. Seu conhecimento em geoquímica dos manguezais, experiência em trabalho de campo e liderança exemplar foram muito valiosos para esta pesquisa.

Ao meu orientador Profº Dr. Marcelo Cohen pela oportunidade e confiança em aceitar me orientar neste doutorado. Você me mostrou entusiasmo e dedicação para com meu projeto de tese, uma ótima relação orientador-aluno, o que permitiu concluir minha tese da melhor maneira possível.

Ao Profº Dr. Wilson Machado da Universidade Federal Fluminense pela parceria com esse trabalho, pelas ideias e sugestões durante a preparação e publicação dos artigos científicos. Obrigada pelo entusiasmo e dedicação a todos os projetos em que trabalhamos juntos, sua abordagem ao ensino e à pesquisa tem me inspirado muito.

Ao Profº Dr. Edouard Metzger pela parceria com esse trabalho, pelas ideias e sugestões durante a preparação e publicação dos artigos científicos. Por me receber tão bem na Universidade de Angers para o doutorado sanduíche.

Ao pesquisador Dr. Christian Sanders da “Southern Cross University” (SCU), por aceitar participar desse projeto. Você desempenhou um papel importante para garantir o sucesso desta pesquisa, contribuindo com análises isotópicas de C e N, datação e taxas de sedimentação.

Muito obrigada pela confiança depositada em mim, e pela grande ajuda durante a preparação e publicação dos artigos científicos.

Ao Museu Paraense Emílio Goeldi pelo apoio e estrutura (laboratorial e de campo) oferecidos para o desenvolvimento do meu doutorado.

Ao Instituto Evandro Chagas e seus funcionários do departamento de Meio Ambiente (Kelson, Mônica e Nelton) pelas análises de metais.

Ao LAMIGA pela análise granulométrica. E aos amigos Laís e Pabllo pelo suporte nas análises.

À amiga Profª Dra. Rut Diaz que sempre me recebe tão bem durante minha estadia em Niterói, obrigada por todo apoio nas análises de AVS e CRS.

Ao Profº Dr. José Augusto por me abrir as portas de seu laboratório, e me apoiar nas análises de cromatografia iônica.

À bolsista de iniciação científica Lyandra do MPEG por todo apoio laboratorial.

Ao Josué e ao Lucivaldo pelo apoio nas atividades de campo.

Ao colega Thiago Souza pelo apoio em um dos trabalhos de campo.

À minha família e meu namorado Tiago por me apoiar em mais um degrau da minha formação acadêmica.

## RESUMO

Neste estudo foi avaliado o potencial dos sedimentos de canais de maré de manguezais em acumular e exportar carbono, nutrientes (N e P), e metais (Fe e Mn), além de avaliar como a sazonalidade regional, chuva-estiagem, influenciam nos parâmetros físico-químicos, nos processos diagenéticos e nos fluxos de nutrientes e metais na interface água-sedimento (IAS). O estudo foi realizado no sistema estuarino do rio Marapanim (norte do Brasil), o qual é influenciado por extensas áreas de manguezais bem desenvolvidos, parte da maior floresta de manguezal contínua e mais bem preservada do mundo, situado aproximadamente a 200 km a oeste da foz do rio Amazonas. Os resultados desse trabalho estão apresentados em dois artigos. O primeiro trata sobre o potencial de estoques e acumulação de carbono orgânico total (COT), nitrogênio total (NT) e fosforo total (PT), além de investigar as potenciais fontes de matéria orgânica (MO) nos sedimentos de canais de maré dos manguezais de Marapanim. O segundo avaliou a influência da sazonalidade nas condições físico-químicas, nos processos diagenéticos e nos fluxos de nutrientes e metais ao longo da IAS dos canais de maré estudados. Durante a estação chuvosa, os valores de salinidade intersticial diminuíram como consequência do aumento da precipitação e da vazão do rio Marapanim, com uma zona de mistura-diluição intensa nos primeiros 15 cm de profundidade. O zoneamento redox dos sedimentos oscilou em resposta aos padrões de chuva, com as maiores concentrações de  $\text{Fe}^{2+}$  e  $\text{Mn}^{2+}$  em camadas mais profundas de sedimentos durante a estação seca. Em condições subóxicas, os sedimentos dos canais de maré atuam como uma fonte de  $\text{Fe}^{2+}$ ,  $\text{Mn}^{2+}$ ,  $\text{NH}_4^+$  e  $\text{PO}_4^{3-}$  para a coluna de água e esses fluxos foram impulsionados pela chuva. Os resultados indicaram que os sedimentos dos canais de maré dos manguezais de Marapanim são bastante eficazes na retenção de carbono, nutrientes e ferro na fase sólida do sedimento do que na exportação para as águas costeiras, enquanto contribuem significativamente para o ciclo oceânico de Mn. O potencial desses canais de marés para esses elementos está diretamente relacionado à granulometria, às fontes e susceptibilidade de degradação da MO. A variabilidade temporal na formação da pirita revelou que os mecanismos de retenção da fase sólida também são suscetíveis a efeitos sazonais, com menores concentrações de enxofre redutível ao cromo (CRS, principalmente fração pirita) na estação de estiagem. Portanto, mostramos que essas variabilidades sazonais implicam em mudanças substanciais nas propriedades físico-químicas e nos processos diagenéticos, afetando a liberação de metais e nutrientes na IAS e seus acúmulo no sedimento.

**Palavras-chave:** Diagênese recente. Variação sazonal. Fontes de matéria orgânica. Condições redox. Fluxos difusivos. Água intersticial.

## ABSTRACT

In this study, we assessed the potential of intertidal mudflat sediments along mangrove forest to accumulate and export carbon, nutrients (N and P) and metals (Fe and Mn), in addition to examine the influence of the Amazonian seasonal rainfall patterns on the physicochemical conditions, diagenetic processes and exchange of nutrients and metals along the sediment-water interface (SWI) in intertidal mudflats fringed by pristine mangroves. The study was carried out in the Marapanim River estuarine system (northern Brazil), which is fringed by extensive areas of well-developed mangroves, part of the largest continuous and best preserved mangrove forest in the world, located approximately 200 km from west of the mouth of the Amazon River. The results of this work are presented in two articles. The first deals with the potential of stocks and accumulation of COT, NT and PT in intertidal mudflat sediments, in addition we investigate the potential sources of sedimentary organic matter (OM). The second assesses the influence of seasonal rainfall pattern on physicochemical properties, the diagenetic processes and the diffusive fluxes of nutrients at the SWI in the Marapanim mangrove creeks. During wet season the salinity values decreased as a consequence of the increase in rainfall, with a dilution-mixing zone in the top sediment (<15 cm). In the dilution-mixing zone, Fe (III) and Mn (IV) reduction are the dominant anaerobic respiratory processes in the sediments. The redox zonation of sediments oscillated in response to the rainfall patterns, with the highest concentrations of  $\text{Fe}^{2+}$  and  $\text{Mn}^{2+}$  in deeper sediment layers during the dry season. Under suboxic conditions, the mudflat sediments act as a source of  $\text{Fe}^{2+}$ ,  $\text{Mn}^{2+}$ ,  $\text{NH}_4^+$ , and  $\text{PO}_4^{3-}$  to the water column, and these fluxes were driven by rainfall. The results indicated that mangrove-fringed mudflats are quite effective in retaining carbon, nutrients and iron in sediment solid phases than exporting to the coastal waters, while can potentially be a significant contributor to the oceanic Mn cycle. The potential of these mangrove creeks to accumulate these elements is directly related to grain size, sources and susceptibility of OM degradation. In addition, temporal variability in pyrite formation revealed that the solid phase retention mechanisms are also susceptible to seasonal effects, with lower concentrations of chromium-reducible sulfur (CRS, mainly pyrite fraction) during the dry season. Therefore, we show that these seasonal variabilities implied substantial changes of physicochemical properties and the diagenetic processes, affecting the release of metals and nutrients from the SWI and their accumulation in the sediment.

**Keywords:** Early diagenesis. Seasonal changes. Organic matter source. Redox conditions. Diffusive fluxes. Pore water.

## LISTA ILUSTRAÇÕES

Figura 1 - Média global de estocagem de carbono ( $Mg\ C\ ha^{-1}$ ) em marismas, prados marinhos e ecossistemas de manguezais. Figura modificada de Alongi (2014). ....	7
Figura 2 - Taxas anuais de acumulação de carbono em florestas de manguezal globalmente. Figura modificada de Alongi (2020). ....	8
Figura 3 - Diagrama conceitual de especiação de Fe sob diferentes condições redox e de pH de sedimentos. Adaptado de Sippo <i>et al.</i> 2020.....	11
Figura 4 - Modelo de representação das zonas biogeoquímicas dentro do sedimento marinho (modificado de Jørgensen; Kasten, 2006). Os nomes de cada zona foram propostos por Froelich, et al. (1979). Os picos de concentração são arbitrários e os perfis refletem a sequência em que cada processo de mineralização é dominante.....	12
Figura 5 - Ciclo do nitrogênio em ecossistemas de manguezal. DRNA significa redução dissimilatória de nitrato para amônio (RDNA). Adaptado de Fernandes <i>et al.</i> (2012).....	14
Figura 6 - Localização da área de estudo e pontos de amostragens P1, P2 e P3.....	16
Figura 7 - Distribuição das precipitações pluviométricas (médias mensais) no estuário do rio Marapanim entre os anos de 2008 a 2018. A linha em vermelho representa os valores médios do ano estudado. Fonte: HidroWeb (2020). .....	17
Figura 8 – Fotos dos manguezais de Marapanim. (a) Rhyzophora, (b) bosque misto de Laguncularia e Avicennia e (c) <i>Spartina brasiliensis</i> em planície lamosa.....	19
Figura 9 – Foto da planície lamosa dos canais de maré do ponto 1 (a) e do ponto 2 (b) na maré baixa.....	20
Figura 10 - Leitura do pH e Eh no testemunho. ....	21
Figura 11 - Extração de água intersticial do sedimento utilizando o sistema Rhyzon® e separação das amostras para análise em <i>glove bag</i> sob atmosfera de $N_2$ .....	22
Figura 12 - Instrumentação para titulação potenciométrica de pequenos volumes de água intersticial. ....	25

## SUMÁRIO

<b>AGRADECIMENTOS .....</b>	<b>v</b>
<b>RESUMO.....</b>	<b>vii</b>
<b>ABSTRACT .....</b>	<b>viii</b>
<b>LISTA ILUSTRAÇÕES.....</b>	<b>ix</b>
<b>1 INTRODUÇÃO .....</b>	<b>1</b>
<b>2 OBJETIVOS .....</b>	<b>3</b>
2.1 GERAL.....	3
2.2 ESPECÍFICOS.....	3
<b>3 REFERENCIAL TEÓRICO .....</b>	<b>4</b>
3.1 FONTES DA MATÉRIA ORGÂNICA SEDIMENTAR .....	4
3.2 ACÚMULO E ESTOQUE DE C, N e P EM SEDIMENTOS DE MANGUEZAIS .....	5
3.3 DIAGÊNESE DA MO SEDIMENTAR.....	9
<b>3.3.1 Fluxos de metais e nutrientes na interface água-sedimento .....</b>	<b>13</b>
<b>4 ÁREA DE ESTUDO .....</b>	<b>16</b>
4.1 LOCALIZAÇÃO DA ÁREA DE ESTUDO .....	16
4.2 CLIMA .....	17
4.3 GEOLOGIA.....	17
4.3 O ESTUÁRIO DO RIO MARAPANIM .....	18
<b>5 MATERIAIS E MÉTODOS .....</b>	<b>20</b>
5.1 PROCEDIMENTOS DE AMOSTRAGEM .....	20
<b>5.1.1 Sedimento .....</b>	<b>20</b>
<b>5.1.2 Parâmetros Físico-Químicos.....</b>	<b>21</b>
<b>5.1.3 Extração da água de fundo e da água intersticial.....</b>	<b>21</b>
<b>5.1.4 Vegetação e fitoplâncton .....</b>	<b>23</b>
<b>5.1.5 Aquisição de imagens de drone e processamento .....</b>	<b>24</b>
<b>5.2 ANÁLISES QUÍMICAS .....</b>	<b>24</b>
<b>5.2.1 Água de fundo e intersticial .....</b>	<b>24</b>
5.2.1.1 Alcalinidade.....	25
5.2.1.2 Fosfato ( $\text{PO}_4^{3-}$ ).....	25
5.2.1.3 Amônio ( $\text{NH}_4^+$ ).....	26
5.2.1.4 Sulfeto ( $\sum \text{H}_2\text{S}$ ).....	26
5.2.1.5 Sulfato ( $\text{SO}_4^{2-}$ ) e cloreto ( $\text{Cl}^-$ ) .....	27
5.2.1.6 Metais dissolvidos ( $\text{Fe}^{2+}$ e $\text{Mn}^{2+}$ ).....	27

<b>5.2.2 Sedimentos.....</b>	28
5.2.2.1 Pré-tratamento .....	28
5.2.2.2 Porosidade e densidade.....	28
5.2.2.3 Granulometria.....	28
5.2.2.4 Geocronologia e Taxa de sedimentação .....	29
5.2.2.5 Composição elementar e isotópica da matéria orgânica.....	29
5.2.2.6 Fósforo total (PT) .....	30
5.2.2.7 Fe e Mn reativos .....	30
5.2.2.8 Enxofre total (ST).....	31
5.2.2.8 Destilação AVS-CRS .....	31
5.2.2.9 Morfologia da pirita.....	31
<b>5.3 FLUXOS DIFUSIVOS NA INTERFACE ÁGUA-SEDIMENTO.....</b>	31
<b>5.4 ANÁLISES ESTATÍSTICA.....</b>	32
<b>6 RESULTADOS E DISCUSSÕES.....</b>	33
6.1 ARTIGO 1: CARBON AND NUTRIENT ACCUMULATION IN TROPICAL MANGROVE CREEKS, AMAZON REGION .....	34
6.2 ARTIGO 2: CONTRASTING SEASONAL RECYCLING OF METALS AND NUTRIENTS IN PORE WATER OF MANGROVE CREEKS, AMAZON REGION .....	47
<b>7 CONCLUSÕES.....</b>	80
<b>REFERÊNCIAS.....</b>	82

## 1 INTRODUÇÃO

Os manguezais são ecossistemas costeiros de transição entre os ambientes terrestre e marinho que ocupam os litorais tropicais e subtropicais entre aproximadamente 30° N e 30° S de latitude. Os avanços na biogeoquímica dos manguezais foram impulsionados pela construção de dois paradigmas antagônicos. Por um lado, a hipótese de que os manguezais podem atuar como sumidouros, armazenando uma quantidade significativa de carbono (Alongi 2020), nutrientes (Breithaupt *et al.* 2014, Sanders *et al.* 2014) e metais (Marchand *et al.* 2011, Thanh-Nho *et al.* 2019) em seus sedimentos. O alto acúmulo da matéria orgânica (MO) em sedimentos de manguezais aumenta a atividade microbiana intensa, muitas vezes levando à depleção de oxigênio nos poucos milímetros superiores do sedimento (Glud 2008, Kristensen *et al.* 1994, Meiggs e Taillefert 2011). Este processo favorece a prevalência de vias anaeróbicas de mineralização da MO (Alongi 1995, Kristensen *et al.* 2011). Em condições anaeróbicas, a redução do sulfato microbiano e a redução do ferro são consideradas as principais vias de mineralização do carbono orgânico durante a diagênese inicial (Ku *et al.* 2008, Kristensen *et al.* 2011, Pan *et al.* 2019).

A degradação anaeróbica da MO sedimentada e a remineralização no sedimento libera nutrientes inorgânicos ( $\text{NH}_4^+$  e  $\text{PO}_4^{3-}$ ) e metais ( $\text{Fe}^{2+}$  e  $\text{Mn}^{2+}$ ) na água intersticial, e os mecanismos de transporte (por exemplo, difusão, advecção e bioturbação) podem induzir a sua transferência para a água sobrejacente e o retorno à zona eufótica, que é muito importante para a produção de fitoplâncton em muitos estuários (Paul *et al.* 2008, Holloway *et al.* 2016). Portanto, os sedimentos dos manguezais também podem atuar como reatores biogeoquímicos que reciclam nutrientes e metais. Estudos anteriores relataram que a troca das águas intersticiais com canais de maré que drenam manguezais pode ser uma fonte significativa de carbono (Taillardat *et al.* 2018, Webb *et al.* 2019), elementos traço (Holloway *et al.* 2016, Sanders *et al.* 2015), e nutrientes (Tait *et al.* 2017, Taillardat *et al.* 2019a), em manguezais para os estuários adjacentes e águas costeiras em escala global. Esta troca de elementos dissolvidos pode ocorrer essencialmente por meio de fluxos difusivos através da interface sedimento-água (IAS) durante a inundação, ou infiltração das águas intersticiais nas colunas de água dos canais durante as marés baixas e vazantes (Bouillon *et al.* 2007, Ovalle *et al.* 1990).

Os manguezais desenvolvidos sob o regime climático da Amazônia estão sujeitos a altas precipitações anuais, altas temperaturas e macromarés semidiurnas. A alta pluviosidade leva a grandes entradas de água doce e alta descarga fluvial, causando flutuações extremas na salinidade dos estuários e canais de maré. Consequentemente, a biogeoquímica dessas águas muda

em escalas temporais (sazonais, marés, diurnos) e espaciais devido às diferenças sazonais de descargas fluviais e entradas de MO de diferentes fontes (principalmente manguezais e fitoplâncton). Estudos anteriores relataram que a sazonalidade de precipitação das chuvas pode levar a mudanças sazonais nas propriedades físicas e químicas (Alongi *et al.* 2004, Berrêdo *et al.* 2016, Marchand *et al.* 2004), na distribuição química da água intersticial (Lee *et al.* 2008, Taillardat *et al.* 2019, Wu *et al.* 2015) e nos fluxos de metais e nutrientes na interface água-sedimento (Adame *et al.* 2010, Alongi *et al.* 2001, Rao *et al.* 2018, Yasui *et al.* 2016,).

O estuário do rio Marapanim faz parte do sistema estuarino amazônico localizado no norte do Brasil, situado a aproximadamente 200 km a oeste do rio Amazonas. Ao longo do estuário do rio Marapanim ocorrem extensas áreas de manguezais bem desenvolvidos, parte da maior floresta de manguezal contínua e mais bem preservada do mundo (Kauffman *et al.* 2018, Nascimento *et al.* 2013). As florestas de manguezais contêm um sistema de canais de maré intrincados de diferentes comprimentos e sinuosidade (Silva *et al.* 2009). Dentro deste contexto, este trabalho avaliou o potencial dos sedimentos de canais de maré de manguezais em acumular e exportar carbono, nitrogênio, fósforo, ferro e manganês, além de avaliar os efeitos da sazonalidade sobre os parâmetros físico-químicos, processos diagenéticos e os fluxos de metais e nutrientes na interface água-sedimento.

## 2 OBJETIVOS

### 2.1 GERAL

Avaliar o potencial dos sedimentos de canais de maré do manguezal de Marapanim-PA em acumular carbono orgânico, nitrogênio, fósforo, ferro e manganês em seus sedimentos, além de avaliar a influência da sazonalidade regional sobre as condições físico-químicas, os processos diagenéticos e os fluxos de nutrientes na interface água-sedimento.

### 2.2 ESPECÍFICOS

- (1) Determinar a taxa de sedimentação e a geocronologia dos sedimentos dos canais de maré.
- (2) Determinar as concentrações e taxas de acúmulo de carbono, nitrogênio, fósforo, ferro e manganês nos sedimentos dos canais de maré.
- (3) Identificar as fontes de matéria orgânica sedimentar através das assinaturas de isótopos estáveis de carbono e nitrogênio ( $\delta^{13}\text{C}$  e  $\delta^{15}\text{N}$ ).
- (4) Determinar as propriedades físico-químicas (pH, Eh, salinidade) e o fracionamento granulométrico dos sedimentos dos canais de maré.
- (5) Identificar as principais vias de decomposição da matéria orgânica sedimentar durante a diagênese recente através dos perfis de  $\text{Mn}^{2+}$ ,  $\text{Fe}^{2+}$ ,  $\text{SO}_4^{2-}$ ,  $\text{H}_2\text{S}$ , alcalinidade,  $\text{NH}_4^+$ , e  $\text{PO}_4^{3-}$  nas águas intersticiais, e AVS (monosulfetos de Fe; FeS), CRS (fração pirita) e ST (enxofre total).
- (6) Determinar a influência das variáveis físico-químicas e dos processos de mineralização da MO nos fluxos de nutrientes e metais na interface água-sedimento (IAS).
- (7) Determinar a influência das mudanças sazonais na variabilidade de espécies dissolvidas nos perfis de água intersticial, nos parâmetros físico-químicos e nos fluxos de nutrientes na IAS.

### 3 REFERENCIAL TEÓRICO

#### 3.1 FONTES DA MATÉRIA ORGÂNICA SEDIMENTAR

Os sedimentos costeiros recebem material orgânico de fontes autóctones (derivadas de fontes *in situ*, como plantas que crescem na superfície do sedimento) e de fontes alóctones (material orgânico transportado para o sedimento de outro lugar, como com a maré ou um rio). Por exemplo, em sedimentos de manguezais, o componente autóctone dominante é derivado de material vegetal vascular *in situ*. Os sedimentos superficiais altamente orgânicos desenvolvem-se no limite mais terrestre, onde a inundação periódica das marés permite uma cobertura vegetal extensa. Em contraste, planícies de maré são frequentemente inundadas por longos períodos, a vegetação vascular está ausente e a matéria orgânica particulada (MOP) alóctone derivada das marés é a fonte dominante de material orgânico nos sedimentos superficiais. Fontes alóctones incluem carbono orgânico particulado fluvial e marinho (COP; principalmente derivado de água doce ou fitoplâncton marinho e matéria orgânica terrígena) e carbono orgânico dissolvido (COD) (Lamb *et al.* 2006).

As razões entre o carbono orgânico total e o nitrogênio total (COT/NT) e as assinaturas de isótopos estáveis de carbono e nitrogênio ( $\delta^{13}\text{C}$  e  $\delta^{15}\text{N}$ ) têm sido amplamente utilizadas como indicadores geoquímicos eficazes para estimar as proporções relativas de MO de origem terrestre e marinha em sedimentos estuarinos e costeiros (Kusumaningtyasa *et al.* 2019, Lamb *et al.* 2006, Liu *et al.* 2015, Ranjan *et al.* 2011, Vilhena *et al.* 2018). Estudos anteriores mostraram que a MO terrestre é preservada, armazenada e se acumula de forma mais eficiente do que a MO de origem marinha em sedimentos (Hedges *et al.* 1997, Kusumaningtyasa *et al.* 2019, Ranjan *et al.* 2011, Watanabe & Kuwae 2015), devido à preservação seletiva de MO refratária em detrimento de componentes lábeis, que é mais suscetível à degradação por microrganismos (Hedges *et al.* 1997, Zonneveld *et al.* 2010). Portanto, identificar a fonte da MO é importante na avaliação da eficácia dos ecossistemas de manguezais como sumidouros de carbono, uma vez que a variabilidade da origem da MO armazenada nos sedimentos contribui de forma diferente para o soterramento de carbono a longo prazo.

A análise dos isótopos  $\delta^{13}\text{C}$  e  $\delta^{15}\text{N}$  baseia-se no fato de que a composição isotópica da MO produzida durante a fotossíntese difere consideravelmente entre os produtores primários. Assim, a assinatura  $\delta^{13}\text{C}$  da MO sedimentar é usada principalmente para estimar a proporção entre plantas terrestres C<sub>3</sub> e C<sub>4</sub> e material marinho/terrestre, respectivamente (Meyers 1997, 2003). Por exemplo, as plantas C<sub>3</sub> são assumidas como tendo TOC/TN > 12 (Meyers 1997),  $\delta^{13}\text{C}$  entre -32 ‰ e -21 ‰ (Deines 1980) e  $\delta^{15}\text{N}$  em torno de 0,4 ± 0,9 ‰ (Peterson & Howarth

1987), enquanto a MO de origem marinha é caracterizada por TOC/TN entre 5 e 7 (Redfield *et al.* 1963),  $\delta^{13}\text{C}$  de -16 ‰ a -23 ‰ (Meyers 1994) e  $\delta^{15}\text{N}$  em torno de  $8,6 \pm 1,0$  ‰ (Peterson e Howarth 1987). Os valores de  $\delta^{13}\text{C}$  de vários componentes vegetativos em plantas de mangue são semelhantes aos de plantas C<sub>3</sub>, que variam de -25 ‰ a -30 ‰ (Muzuka & Shunula 2006). A composição média de  $\delta^{15}\text{N}$  na vegetação de manguezal varia de -1,5 ‰ a 3,2 ‰ (Muzuka & Shunula 2006).

As proporções relativas da MO de origem terrestre/manguezal e marinha em sedimentos podem ser estimadas usando o modelo de mistura de dois *end-members* como descrito em Schutlz & Calder (1976):

$$F_{\text{terr}} = (\delta^{13}\text{C}_{\text{mar}} - \delta^{13}\text{C}_{\text{sed}})/(\delta^{13}\text{C}_{\text{mar}} - \delta^{13}\text{C}_{\text{terr}}) \times 100 \text{ and } F_{\text{mar}} = 100 - F_{\text{terr}} \quad (1)$$

onde  $F_{\text{terr}}$  é a contribuição da fração terrestre/manguezal,  $F_{\text{mar}}$  é a contribuição da fração marinha,  $\delta^{13}\text{C}_{\text{sed}}$  é o valor do intervalo de sedimentos e  $\delta^{13}\text{C}_{\text{terr}}$  e  $\delta^{13}\text{C}_{\text{mar}}$  são os valores de *end-members* terrestre e marinho, respectivamente. Neste estudo, estimamos os valores de  $\delta^{13}\text{C}$  do *end-member* terrestre (uma média das plantas que dominam no manguezal de Marapanim) e marinho (MO derivada do fitoplâncton) em  $-29,9 \pm 1,0$  ‰ ( $n = 18$ ) e  $-23,9 \pm 0,7$  ‰ ( $n = 3$ ), respectivamente, a partir de nossos resultados.

### 3.2 ACÚMULO E ESTOQUE DE C, N e P EM SEDIMENTOS DE MANGUEZAIS

Sistemas estuarinos são influenciados pela vegetação costeira. Ecossistemas de vegetação costeira, como os manguezais, os pântanos salgados e as comunidades de ervas marinhas são reconhecidos como ecossistemas de “carbono azul” devido à sua capacidade de sequestrar carbono em uma taxa muito maior do que as florestas terrestres (Nellemann *et al.* 2009, McLeod *et al.* 2011). Embora as florestas de manguezal ocupem <1% da área costeira global, esses ecossistemas sequestram e armazenam grandes quantidades de carbono orgânico na biomassa vegetal e nos sedimentos, contribuindo com 10 - 15% para o armazenamento de carbono nos sedimentos costeiros (Alongi 2014, Dittmar *et al.* 2006, Jennerjahn & Ittekkot 2002). Portanto, sua conservação é valiosa no que diz respeito à mitigação das mudanças climáticas, removendo o CO<sub>2</sub> atmosférico (Duarte *et al.* 2013). Além disso, eles oferecem serviços ecossistêmicos essenciais, como proteção costeira contra deslizamentos de terra, tempestades e tsunamis; recursos pesqueiros; entre outros.

Duas medidas importantes para determinar a taxa de sequestro de carbono orgânico são o conteúdo de carbono orgânico do sedimento (Corg) e a taxa de acumúlo de sedimento (SAR). O primeiro termo fornece informações sobre o estoque de Corg sequestrado em sedimentos (Howard *et al.* 2014), e as avaliações de estoque permitem calcular o potencial de CO<sub>2</sub> sendo liberado na degradação e desmatamento (Kusumaningtyas *et al.* 2019). O SAR é usado para medir as taxas de acúmulo de Corg, que abordam a questão de quanto Corg é sequestrado em um período específico e quantifica a capacidade de drenagem contínua (Arias-Ortiz *et al.* 2018). A partir da série de decaimento <sup>238</sup>U, o método de datação <sup>210</sup>Pb tem sido um traçador ideal para datar sedimentos aquáticos depositados durante os 100 anos anteriores, permitindo a determinação das taxas de acumulação de TOC em ecossistemas de vegetação costeira (Marchio *et al.* 2016, Sanders *et al.* 2016, Sasmito *et al.* 2020, Smoak *et al.* 2013).

A média total dos estoques de Corg do ecossistema de manguezal é de  $738.9 \pm 27.9$  Mg Corg ha<sup>-1</sup> ( $\pm 1$ ); a média da biomassa de Corg acima do sedimento (viva e morta) é de  $109.3 \pm 5.0$  Mg Corg ha<sup>-1</sup> ( $\pm 1$ ); a média da biomassa de C abaixo do sedimento (raízes vivas e mortas) é de  $80.9 \pm 9.5$  Mg Corg ha<sup>-1</sup> ( $\pm 1$ ), e a média de Corg estocado no sedimento é de  $565.4 \pm 25.7$  Mg Corg ha<sup>-1</sup> ( $\pm 1$ ) (Alongi 2020). Sendo assim, os sedimentos de manguezais acumulam aproximadamente 75% do Corg do ecossistema, enquanto 15% restante forma parte das folhas e ramos de manguezais e os 10% restante pode fazer parte da biomassa formada pelas raízes e outras estruturas subsuperficiais da vegetação (Alongi 2014) (Figura 2). Há uma variabilidade considerável nessas estimativas, refletindo a ampla gama de idades e tipos geomorfológicos de florestas, de plantações jovens a florestas maduras não perturbadas. Além disso, é altamente provável que os estoques de C do solo sejam subestimados na maioria dos estudos, pois outros estudos mediram estoques consideráveis de C do solo abaixo de 1 m de profundidade (Alongi 2020). Kauffman *et al.* (2018) calcularam uma média total de estoque de Corg de 511 Mg Corg ha<sup>-1</sup> para os manguezais do norte do Brasil, relativamente baixo para a média global. Ainda assim, os estoques de carbono nos manguezais da Amazônia são pelo menos duas vezes maiores do que os estoques atribuídos à floresta amazônica (Kauffman *et al.* 2018), o que ressalta seu valor potencial para mitigar as emissões de gases de efeito estufa.

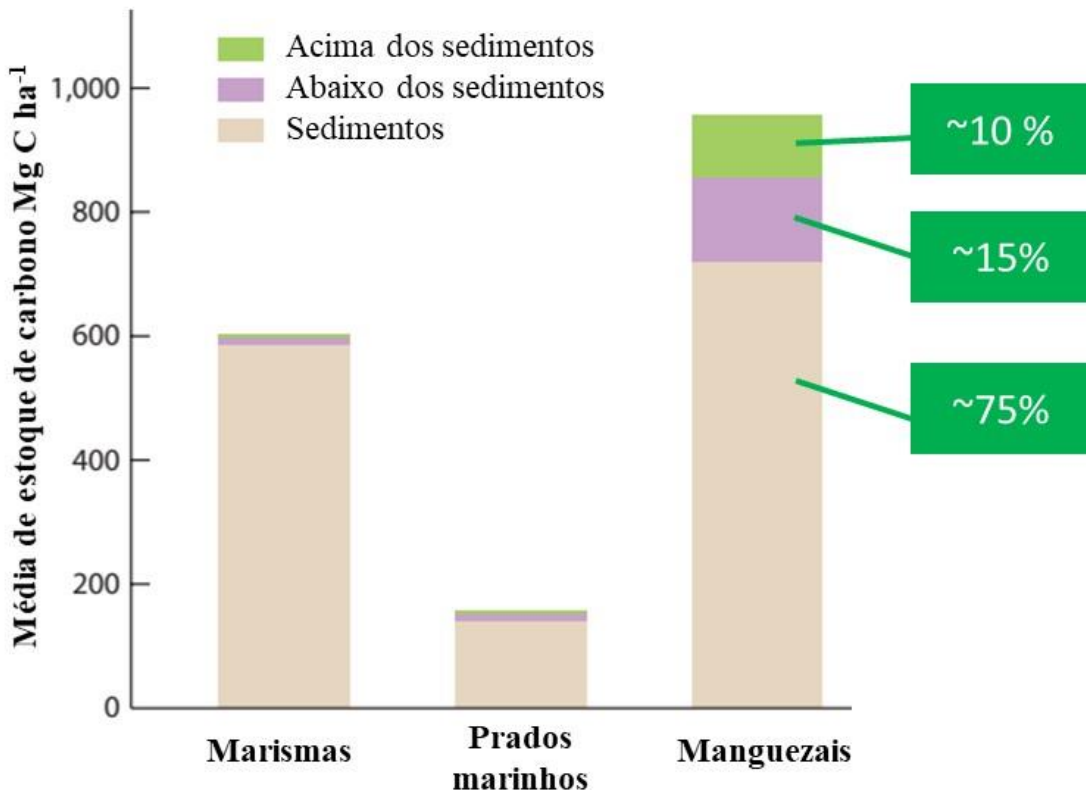


Figura 1 - Média global de estocagem de carbono ( $\text{Mg C ha}^{-1}$ ) em marismas, prados marinhos e ecossistemas de manguezais. Figura modificada de Alongi (2014).

Taxas de acúmulo de carbono, derivadas das taxas de acúmulo do solo, em manguezais são em média  $179,6 \text{ g C m}^{-2} \text{ a}^{-1}$  (Alongi 2020), com taxas variando amplamente de 1 a  $1722,2 \text{ g C m}^{-2} \text{ a}^{-1}$  (Figura 2). Essa grande faixa de variação reflete o alto nível de variabilidade nas taxas de acumulação do solo e taxas de sequestro de carbono entre manguezais de diferentes idades, tipos e locais. Segundo Perez *et al.* (2018) a distribuição de taxa de acumulação de carbono dentro das florestas e locais adjacentes (margem e planícies lamosas) de ecossistemas de manguezal não exibiu diferenças significativas com a latitude, pois é provável que essas taxas sejam uma função de vários fatores inter-relacionados, como florestamento, frequência de inundação das marés, elevação das marés, geomorfologia, composição de espécies, granulometria, captação e entrada do rio e extensão de insumos antrópicos (Perez *et al.* 2018, Alongi 2020). A maioria das taxas mais altas foram medidas em florestas maduras próximas a deltas de rios e em florestas em bacias hidrográficas altamente impactadas, como por exemplo as altas taxas de  $1020$  e  $1023 \text{ g C m}^{-2} \text{ a}^{-1}$  nos estuários de Jiulongjiang, China, e Cubatão, Brasil, respectivamente (Alongi *et al.* 2005, Sanders *et al.* 2014).

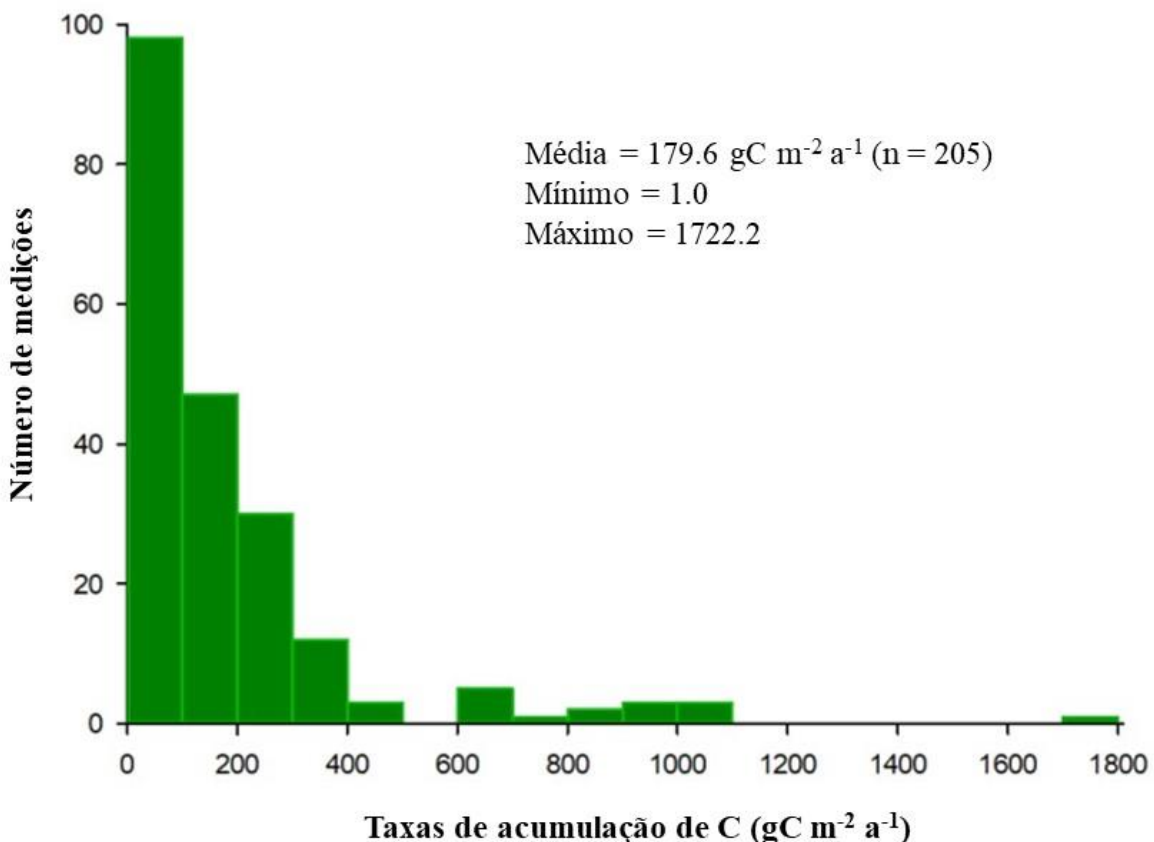


Figura 2 - Taxas anuais de acumulação de carbono em florestas de manguezal globalmente. Figura modificada de Alongi (2020).

Como as taxas de acumulação de carbono podem refletir condições locais, mais dados regionais são necessários, em diferentes regimes de marés, para reduzir as incertezas, ajudar na escala latitudinal e restringir os orçamentos de carbono regionais e globais. Além da maior extensão existente de florestas tropicais, a Amazônia brasileira possui uma das maiores áreas de manguezais do mundo. Embora a preservação da floresta amazônica tenha sido objeto de intensos esforços de conscientização nas últimas décadas, menos atenção tem sido dada aos manguezais da Amazônia.

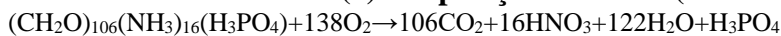
Determinar os estoques e taxas de acumulação de nitrogênio e fosforo também é importante para avaliar como esses nutrientes se correlacionam com o estoque e acúmulo de carbono. Por exemplo, Breithaup *et al.* (2014) observaram que solos de manguezal com altas taxas de acumulação de NT e PT podem levar ao aumento da remineralização do carbono do solo, contribuindo para as baixas taxas de enterramento de carbono. No entanto, Matos *et al.* (2020) observaram que em sedimentos de canais de marés de manguezais, os estoques e acumulação de COT foram maiores nos pontos de amostragem onde eram maiores os estoques e acumulação de NT e PT, devido às altas taxas de sedimentação ( $1,5 \pm 03$  cm ano<sup>-1</sup>), que contribui significantemente para preservar a MO.

### 3.3 DIAGÊNESE DA MO SEDIMENTAR

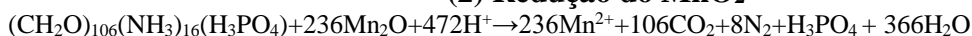
O processo de decomposição biogeoquímica da MO sedimentar mediada por micro-organismos é conhecido como diagênese recente da MO (Henrichs 1992). As reações biogeoquímicas regulam a mineralização e a preservação da MO, a regeneração de nutrientes e a formação de minerais autigênicos. Perfis de água intersticial de espécies dissolvidas servem como um indicador sensível das reações diagenéticas recente (Berner 1980). O sedimento de estuários tropicais recebe grandes quantidades de MO e experimentam alta sedimentação de MO alóctone e autóctone junto com condições quentes que sustentam taxas de respiração bentônica elevadas. Devido esse alto *input* de MO, as taxas de mineralização sedimentar são altas e o oxigênio é rapidamente esgotado nos primeiros milímetros do sedimento (Glud 2008, Meiggs e Taillefert 2011). Isso favorece a predominância de vias anaeróbicas de mineralização da MO (Alongi, 1995, Kristensen *et al.* 2011).

A degradação anaeróbica da MO depende da taxa de sedimentação, qualidade e quantidade da MO, profundidade de penetração do oxigênio, a granulometria do sedimento e disponibilidade de aceitadores de elétrons, como nitrato ( $\text{NO}_3^-$ ), óxidos de ferro (Fe (III)) e manganês (Mn (IV)), sulfato ( $\text{SO}_4^{2-}$ ) e dióxido de carbono ( $\text{CO}_2$ ) em sedimentos (Canfeld 1994, Froelich *et al.* 1979, Schubert *et al.* 2000). A sequência prevista das reações, juntamente com a estimativa dos seus rendimentos de energia livre por mole de MO é descrita na Tabela 1. Em sedimentos de manguezais, ricos em carbono orgânico, a redução de  $\text{NO}_3^-$  levando à produção de  $\text{N}_2$  (desnitrificação) é limitada a uma fina camada oxigenada e, portanto, não desempenha um papel importante na mineralização da MO em sedimentos costeiros (Jørgensen 1983). A redução do sulfato microbiano para  $\Sigma\text{H}_2\text{S}$  ( $= \text{H}_2\text{S} + \text{HS}^- + \text{S}^{2-}$ ) e a redução de (hidróxidos de ferro para  $\text{Fe}^{2+}$  são consideradas as principais vias de mineralização do carbono orgânico e processos biogeoquímicos durante a diagênese recente, que geralmente está associada à ativação de nutrientes (Kristensen *et al.* 2011, Ku *et al.* 2008, Pan *et al.* 2019).

Tabela 1 – Reações de oxidação da matéria orgânica sedimentar

**(1) Respiração aeróbica (consumo de O<sub>2</sub>)**

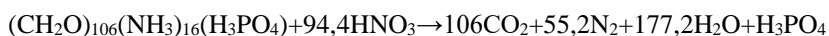
$\Delta G_r = -3.190 \text{ kJ mol}^{-1}$

**(2) Redução do MnO<sub>2</sub>**

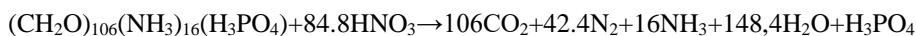
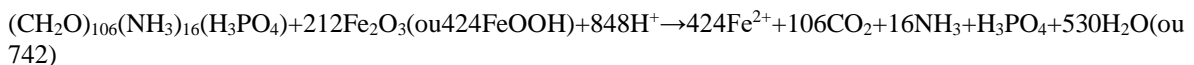
$\Delta G_r = -3090 \text{ kJ mol}^{-1}$  (Birnessite)

$-3050 \text{ kJ mol}^{-1}$  (Nsutite)

$-2920 \text{ kJ mol}^{-1}$  (Pyrolusite)

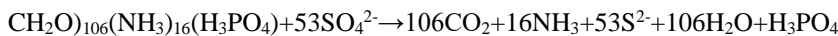
**(3a) Desnitrificação**

$\Delta G_r = -3.030 \text{ kJ mol}^{-1}$

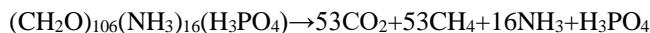
**(3b) Redução do NO<sub>3</sub><sup>-</sup>****(4) Redução do Fe<sub>2</sub>O<sub>3</sub>**

$\Delta G_r = -1410 \text{ kJ mol}^{-1}$  (Hematita, Fe<sub>2</sub>O<sub>3</sub>)

$-1330 \text{ kJ mol}^{-1}$  (Goethita, FeOOH)

**5) Redução do SO<sub>4</sub><sup>2-</sup>**

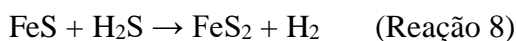
$\Delta G_r = -380 \text{ kJ mol}^{-1}$

**(6) Metanogênese**

$\Delta G_r = -350 \text{ kJ mol}^{-1}$

Fonte: Froelich *et al.* (1979).

Parte do sulfeto produzido pela sulfato-redução bacteriana pode reagir com o Fe<sup>2+</sup> para formar sulfetos de ferro metaestáveis, como por exemplo FeS amorfó (reação 7), mackinawita (FeS), greigita (Fe<sub>3</sub>S<sub>4</sub>) e pirrotita (FeS<sub>1,1</sub>) (Morse *et al.* 1987, Otero e Macias 2002) e, finalmente, formar pirita à temperatura ambiente (reação 8) (Berner 1970), que geralmente é restrita pelo fornecimento de matéria orgânica decomposta, sulfato dissolvido e minerais de ferro detriticos reativos em sedimentos marinhos (Berner 1984). Por exemplo, a pirita pode formar-se diretamente pela adição de enxofre elementar ou polisulfeto para FeS (Reações 7 e 8).



Em ambientes de maré, entretanto, fatores adicionais devem ser considerados. As correntes de maré e a ação das ondas podem afetar o estado de oxidação dos sedimentos diretamente pelo aumento do transporte advectivo da água intersticial e partículas. Durante a maré

baixa, o oxigênio pode penetrar mais profundamente no sedimento por meio da bioturbação de atividade das raízes e fauna (Ferreira *et al.* 2007, Kristensen 2008, Kristensen & Alongi 2006). Devido à entrada de oxigênio, a oxidação do sulfeto reduzido pode ocorrer em manguezais, e até o enxofre da pirita pode ser reoxidado para sulfato, liberando ácido para a água intersticial (Reação 9) (Ding *et al.* 2014, Ferreira *et al.* 2007, Holmer *et al.* 1994). Um diagrama conceitual dos processos de formação e oxidação da pirita sob diferentes condições redox e de pH dos sedimentos pode ser observado na Figura 9.

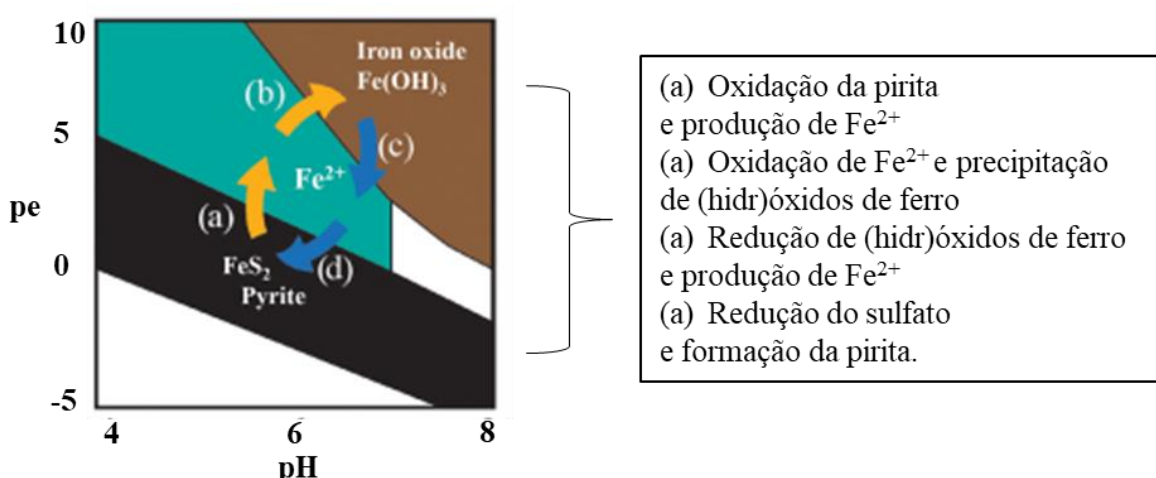


Figura 3 - Diagrama conceitual de especiação de Fe sob diferentes condições redox e de pH de sedimentos. Adaptado de Sippo *et al.* (2020).

O ciclo do enxofre está intimamente ligado aos reservatórios de ferro reativo (Thamdrup 2000). Os óxidos de ferro reativos presentes nos sedimentos podem oxidar eficientemente os sulfetos reduzidos. Isso sugere que a ciclagem de compostos de enxofre reduzidos é altamente dinâmica em sedimentos de florestas de mangue. A quantidade de sulfetos enterrados é normalmente extraída em duas categorias principais, os sulfetos voláteis em ácido (AVS - *acid volatile sulfide*) e reduzíveis com cromo (CRS - *chromium reduction sulfide*). A fração AVS consiste principalmente de compostos de H<sub>2</sub>S e FeS dissolvidos, e a fração CRS é principalmente de pirita. A pirita parece ser o componente de enxofre inorgânico mais importante em sedimentos de manguezal, atingindo quantidade de 50-100 vezes maiores do que AVS (Alongi *et al.* 1998, Holmer *et al.* 1994, 1999, Kristensen *et al.* 1991, 1992).

Froelich *et al.* (1979) associaram os processos de mineralização com a definição de zona redox dentro de um registro sedimentar, baseado na investigação de perfis de água intersticial. A Fig. 3 mostra um modelo de perfil vertical de água intersticial correspondente a cada

espécie produzida e consumida nestas zonas redox e uma relação destas zonas com a classificação quanto ao potencial de redução do sedimento. A camada de sedimento onde predomina a respiração aeróbica é referida como zona óxica, nesta zona as concentrações de Mn e Fe dissolvidos ( $\text{Fe}^{2+}$  e  $\text{Mn}^{2+}$ ) são relativamente baixas devido à formação de suas fases sólidas oxidadas ( $\text{MnO}_2$  e  $\text{FeOOH}$ ). Abaixo da zona óxica os sedimentos são referidos como sub-óxicos, estes são bem caracterizados por um pico de Mn e Fe dissolvidos que são reduzidos na ausência de oxigênio e, portanto, mobilizados para a fase dissolvida. Abaixo da zona sub-óxica, os sedimentos são referidos como anóxicos, e nesta zona do sedimento ocorre a redução do sulfato e diminuição das concentrações de Fe dissolvido devido à formação de sulfetos de ferro insolúveis ( $\text{FeS}_2$ ; Rivera-Duarte & Flegal 1997). A interpretação dos processos geoquímicos que ocorrem nos sedimentos é auxiliada pelos valores de pH, que geralmente diminuem devido à mineralização microbiana do carbono orgânico aparecendo como uma interface entre as camadas óxica e anóxica.

Zona	Química da água intersticial	Processo de mineralização
Óxica	$\text{O}_2$	Respiração Óxica Redução do Nitrato
Subóxica (pós-óxico)	$\text{NO}_3^-$ $\text{Mn}^{2+}$ $\text{Fe}^{2+}$	Redução do Manganês Redução do Ferro
Anóxica (sulfídrico)	$\text{SO}_4^{2-}$	Redução do Sulfato
(metânico)	$\text{H}_2\text{S}$ $\text{CH}_4$	Oxidação anaeróbica do metano Metanogênese

Figura 4 - Modelo de representação das zonas biogeocíquimicas dentro do sedimento marinho (modificado de Jørgensen & Kasten 2006). Os nomes de cada zona foram propostos por Froelich, et al. (1979). Os picos de concentração são arbitrários e os perfis refletem a sequência em que cada processo de mineralização é dominante.

### 3.3.1 Fluxos de metais e nutrientes na interface água-sedimento

Estudos anteriores relataram que a troca das águas intersticiais com canais de maré que drenam manguezais pode ser uma fonte significativa de elementos traço (Holloway *et al.* 2016, Sanders *et al.* 2015), e nutrientes (Tait *et al.* 2017, Taillardat *et al.* 2019), em manguezais para os estuários adjacentes e águas costeiras em escala global. Esta troca de elementos dissolvidos pode ocorrer essencialmente por meio de fluxos difusivos através da interface água-sedimento durante a inundação, ou infiltração das águas intersticiais nas colunas de água dos canais durante as marés baixas e vazantes (Bouillon *et al.* 2007, Ovalle *et al.* 1990).

O manganês (Mn) é um micronutriente essencial para os organismos marinhos e é um componente central nos processos fotossintéticos. O Ferro (Fe) é considerado um requisito biológico vital para todos os organismos marinhos (Sunda 2002). As exportações de Fe e Mn dissolvidos de manguezais podem desempenhar um papel importante nos orçamentos de metais traço oceânicos, mas a magnitude desses fluxos permanece amplamente desconhecida (Holloway *et al.* 2016, Sanders *et al.* 2012). Alternativamente, os manguezais podem ser drenos eficientes de metais traço essenciais (Bayen 2012, Lewis *et al.* 2011, Machado *et al.* 2002). Processos biogeoquímicos como adsorção, oxidação, redução e precipitação frequentemente determinam se os sistemas de mangue são um sumidouro ou fonte de metais (Bayen 2012, Hatje *et al.* 2003, Machado *et al.* 2002). Devido a processos biogeoquímicos e hidrológicos, os manguezais podem liberar Fe e Mn acumulados para águas superficiais adjacentes (Alongi *et al.* 2001, Bayen 2012, Lewis *et al.* 2011, Sanders *et al.* 2012). Por exemplo, estudos na Austrália mostraram que canais de maré de manguezais são capazes de exportar grandes quantidades de Mn dissolvido, que são maiores do que os fluxos estimados de fontes ribeirinhas e atmosféricas, demonstrando que canais de manguezais podem ter um papel importante no ciclo oceânico de Mn (Holloway *et al.* 2016).

A decomposição bacteriana pode mineralizar nutrientes orgânicos em amônio ( $\text{NH}_4^+$ ) (Feller *et al.* 2003) (Fig. 4). O amônio é responsável pela forma de nitrogênio mais facilmente assimilável para absorção pela vegetação (Fernandes *et al.* 2012). No entanto, a assimilação de  $\text{NH}_4^+$  da vegetação via raízes está competindo com a atividade microbiana e a adsorção de partículas de sedimento (Deborde *et al.* 2015, Fernandes *et al.* 2012). O amônio também pode ser transformado como nitrato ( $\text{N}-\text{NO}_3^-$ ) via nitrito ( $\text{N}-\text{NO}_2^-$ ) durante a nitrificação (Fig. 4). Considerando o oxigênio limitado disponível nos sedimentos dos manguezais, essa transformação não é direta e é mais provável de ocorrer na coluna d'água do canal de maré (Gleeson *et al.* 2013). Por muito tempo, acreditou-se que as vias de transformação de nitrato em manguezais

eram limitadas à desnitrificação que ocorre no sedimento em condições redutoras (Twilley & Rivera-Monroy 2009). No entanto, os estudos mais recentes identificaram a redução dissimilatória do nitrato para amônio (DNRA) em vez da desnitrificação como a principal via de transformação do nitrato (Fernandes *et al.* 2012, Maher *et al.* 2016). Essa hipótese é consistente com a teoria de que os manguezais são altamente eficientes na preservação de nutrientes em seu sistema como uma adaptação ao ambiente limitado por nutrientes. Enquanto desnitrificação transforma  $\text{NO}_3^-$  em  $\text{N}_2\text{O}$  e  $\text{N}_2$  que induz uma perda de N no sistema, DNRA converte nitrato em amônio levando a uma conservação do átomo de N no sistema.

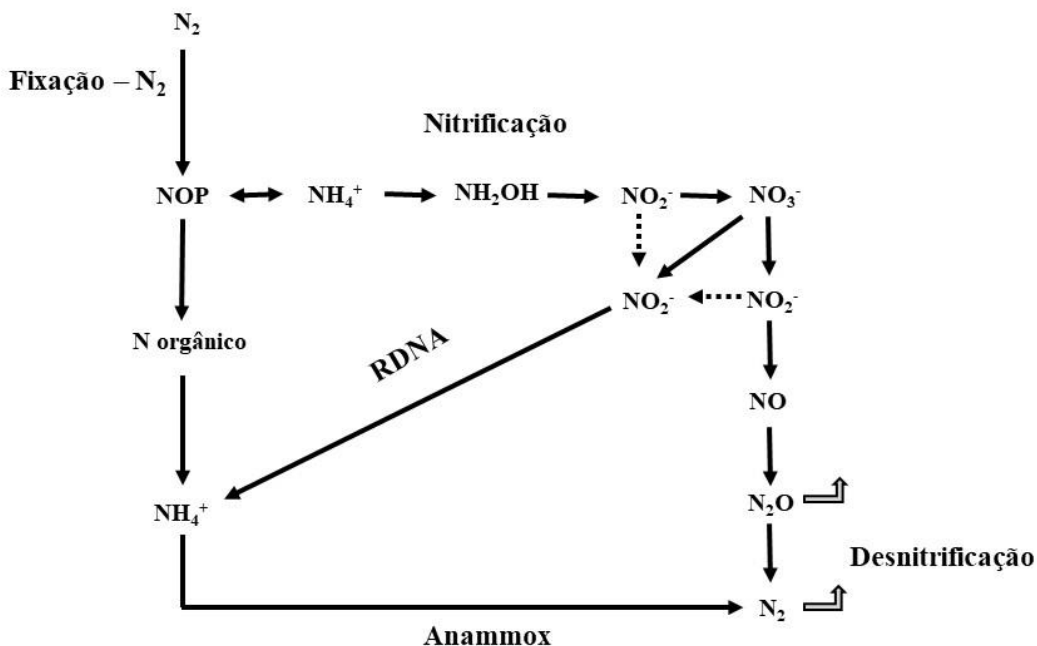


Figura 5 - Ciclo do nitrogênio em ecossistemas de manguezal. DRNA significa redução dissimilatória de nitrato para amônio (RDNA). Adaptado de Fernandes *et al.* (2012).

O ciclo do fósforo em ambientes de manguezal segue caminhos semelhantes aos do ciclo do nitrogênio, com interações próximas entre a vegetação, as bactérias e os sedimentos para a produção, transformação e assimilação (Twilley & Rivera-Monroy 2009). No entanto, apenas uma forma inorgânica dissolvida de fósforo pré-existe, que é o ortofosfato ( $\text{P}-\text{PO}_4^{3-}$ ). Uma diferença principal entre o ciclo do nitrogênio e do fósforo é a forte interação entre o fósforo inorgânico e o ferro. Em sedimentos aeróbicos, o ferro adsorve a maior parte do fósforo inorgânico que pode ser posteriormente liberado durante a dissolução como fósforo inorgânico dissolvido (Deborde *et al.* 2015, Holmer *et al.* 1994).

No período de chuvas, a drenagem continental também influí na qualidade das águas estuarinas e no transporte de nutrientes e material particulado (Gomes *et al.* 2013). Portanto, pode-se esperar que no período chuvoso ocorra maior concentração de nutrientes, favorecendo

a produção fitoplanctônica, e que, no período seco, as águas costeiras influenciem a qualidade das águas estuarinas, com baixa turbidez, alto teor de oxigênio e pH levemente alcalino (Moura e Nunes 2016). Variações sazonais também podem afetar os fluxos de Fe e Mn dissolvidos na IAS, por exemplo, durante a estação de estiagem, a falta de inundações frequentes das marés pode resultar na oxidação de sedimentos durante períodos prolongados de exposição, e a mobilização do Fe e Mn dissolvidos pode acontecer em camadas mais profundas dos sedimentos (Marchand *et al.* 2005), limitando assim os fluxos de Fe e Mn dissolvidos na IAS.

## 4 ÁREA DE ESTUDO

### 4.1 LOCALIZAÇÃO DA ÁREA DE ESTUDO

A área de estudo está situada no norte do estuário do rio Marapanim, no município de Marapanim, costa nordeste do estado do Pará, a 120 km de Belém, e a leste da desembocadura do rio Amazonas (Amazônia Oriental), limitada pelas coordenadas 00°32'30"S/00°52'30"S e 47°28'45"W/ 47°45'00"W (Figura 5).

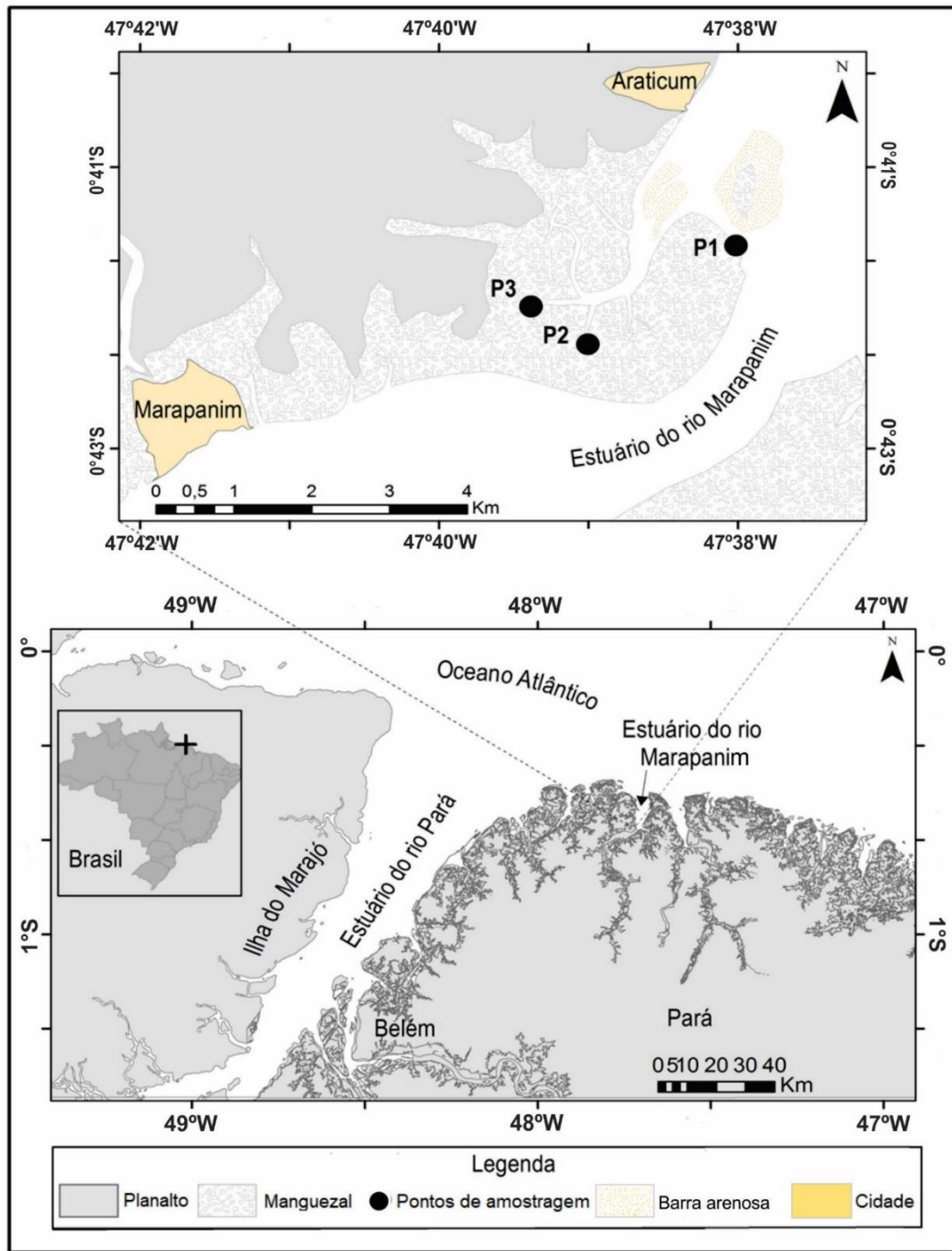


Figura 6 - Localização da área de estudo e pontos de amostragens P1, P2 e P3.

## 4.2 CLIMA

O clima da região é o tropical chuvoso, do tipo climático Am (na classificação de Köppen). A região está situada em baixa latitude e caracteriza-se por calor e umidade constantes, destacando-se os altos índices pluviométricos, com fortes pancadas de chuva (Martorano *et al.* 1993). A temperatura média anual situa-se em torno de 27,7 ° C, com umidade relativa do ar entre 80 a 85 %, intimamente associada ao regime de precipitação pluviométrica, cujas médias anuais situam-se próximo de 2500 mm. Uma sazonalidade marcante caracteriza as chuvas da região, podendo-se distinguir claramente duas estações neste setor da costa: a mais chuvosa, que ocorre entre janeiro a junho, com médias mensais anuais entre 199 a 576 mm e outra, menos chuvosa, entre julho a dezembro, com 5 a 153 mm (Figura 6).

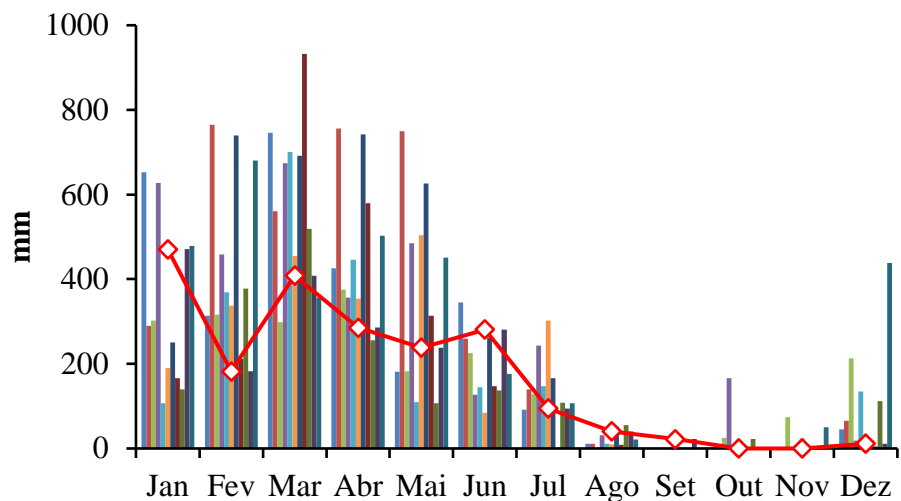


Figura 7 - Distribuição das precipitações pluviométricas (médias mensais) no estuário do rio Marapanim entre os anos de 2008 a 2018. A linha em vermelho representa os valores médios do ano estudado. Fonte: HidroWeb (2020).

## 4.3 GEOLOGIA

Os sedimentos de manguezais do estuário do rio Marapanim são formados a partir do intemperismo tropical dos sedimentos terciários da Formação Barreiras, em geral latossolos amarelos (Oliveira Júnior *et al.* 1997). Parte da sedimentação lamosa que constitui os manguezais foi depositada sobre barras arenosas dispostas ao longo do rio Marapanim. Esses sedimentos, assim sobrepostos, foram colonizados posteriormente pela vegetação característica dos manguezais. O material clástico (principalmente quartzo, caulinita e óxidos de ferro), transportado e depositado sobre barras de areia formadas ao longo do estuário, se junta às contribuições

marinhas (íons alcalinos e alcalino terrosos), com teores variados de matéria orgânica e abundantes diatomáceas. Esse material é retrabalhado por processos de degradação e formação mineralógica, resultando em fases mineralógicas sulfetadas (pirita), aluminossilicatadas (esmectita e feldspatos-K) e quartzo (Berrêdo 2006, 2008). Os minerais pesados mais importantes são zircão, turmalina, estaurolita, cianita, rutilo, ilmenita e raramente, anatásio, andaluzita, topázio, granada e anfibólio (Vilhena *et al.* 2010). Com o prosseguimento da estiagem e a exposição prolongada dos sedimentos, principalmente nas marés de quadratura, ocorre uma gradual concentração dos fluxos intersticiais e a precipitação da halita, a formação de cristais de gipso e jarosita e a precipitação de oxi-hidróxidos de ferro na porção superior dos sedimentos (Berrêdo 2006).

#### 4.3 O ESTUÁRIO DO RIO MARAPANIM

O estuário apresenta morfologia estuarina em forma de funil. O canal principal do rio Marapanim tem extensão de mais de 70 km e largura de 8 km na foz, com abertura para o oceano Atlântico, sujeito à incursão das ondas oceânicas e macromarés semidiúras que têm amplitude de 3,5 m durante a maré de quadratura e mais de 6 m durante as marés de sizígia (Silva *et al.* 2009). As águas salinas penetram aproximadamente 62 km na foz do estuário durante a estação seca e 42 km durante a estação chuvosa (Berrêdo *et al.* 2008). Dentro do funil, observa-se canais de maré com baixa sinuosidade, onde ocorrem depósitos de planície de maré lamosa e barra de maré (arenosa e lamosa). A temperatura da água do estuário varia de 27 a 30 °C. Os valores de pH indicam condições alcalinas durante a estação seca (7,9 a 8,0) e ligeiramente ácidas durante a estação chuvosa (5,7 a 6,7). A salinidade na baixa e alta descarga fluvial varia de 24 a 3, respectivamente, no canal estuarino (Berrêdo *et al.* 2008).

O estuário faz parte da Reserva Extrativista Marinha Mestre Lucindo, uma região protegida de Unidade de Conservação. Ao longo do estuário do rio Marapanim ocorrem extensas áreas de manguezais bem desenvolvidos, parte da maior floresta de manguezal contínua e mais bem preservada do mundo (Nascimento *et al.* 2013, Kauffman *et al.* 2018). O estuário contém 130 km<sup>2</sup> de floresta de mangue contínua e intocada (Vilhena *et al.* 2013). As espécies dominantes de mangue são *Rhizophora mangle*, *Avicennia germinans* e *Laguncularia racemosa*. As árvores são altas (até aproximadamente 35 m), geralmente distribuídas em bosques mistos de *Rhizophora spp.* e *Avicennia germinans*. *Laguncularia racemosa* é encontrada na franja do manguezal. *Spartina brasiliensis* ocupa posição pioneira em áreas de acreção de planícies lamaçentas. Os manguezais são tipicamente de intermaré, submersos regularmente sob as marés

de sizígia. Nas marés de quadratura, contudo, extensas áreas ficam expostas por vários dias, efeito intensificado principalmente na estiagem, devido à redução da descarga hídrica do rio Marapanim (Berrêdo 2006).

A bacia hidrográfica de Marapanim se estende por uma área de 2.500 km<sup>2</sup> (Silva *et al.* 2009), sem desenvolvimento industrial, onde vivem cerca de 28.000 pessoas. Como outras cidades costeiras da Amazônia brasileira, a economia da cidade de Marapanim baseia-se principalmente no uso sustentável dos recursos naturais, principalmente a pesca (caranguejos, camarões, moluscos e peixes), bem como o comércio e o turismo (ICMBio 2018, Fernandes *et al.* 2019, Kjerfve & Lacerda 1993).

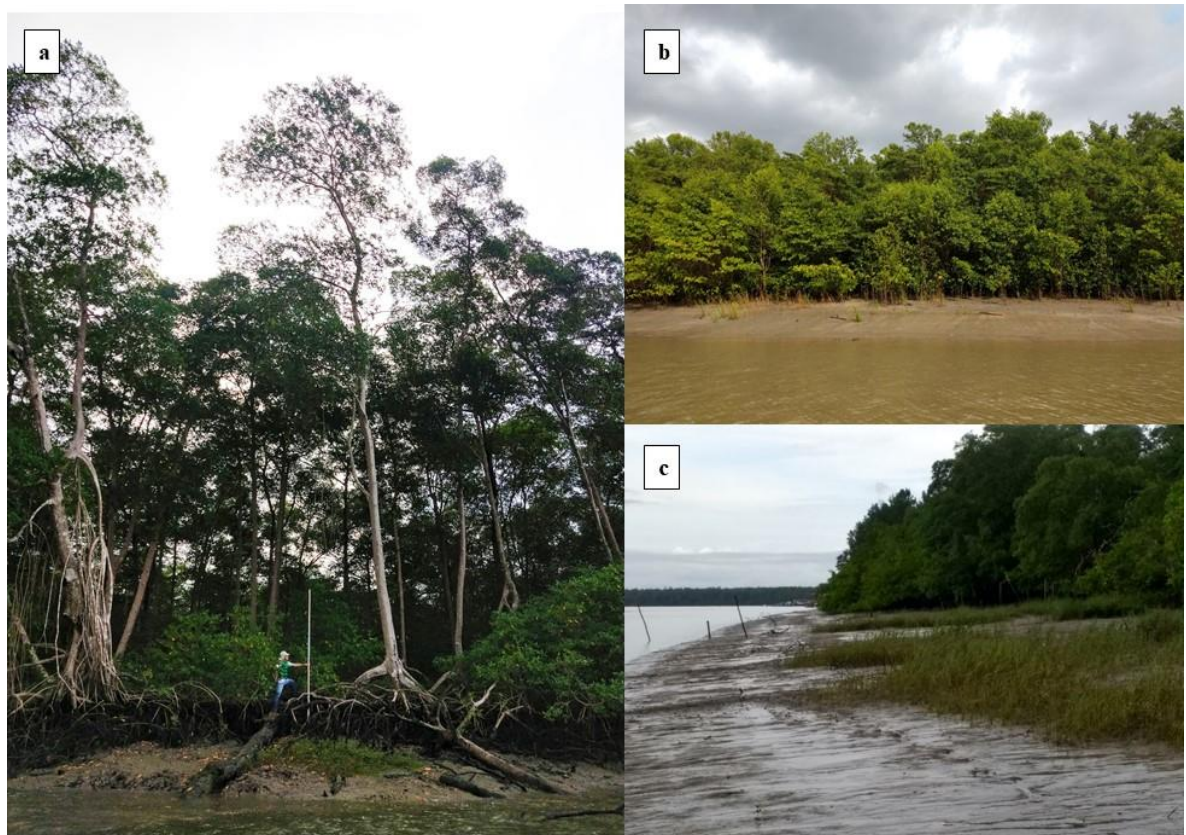


Figura 8 – Fotos dos manguezais de Marapanim. (a) *Rhizophora*, (b) bosque misto de *Laguncularia* e *Avicennia* e (c) *Spartina brasiliensis* em planície lamosa.

## 5 MATERIAIS E MÉTODOS

### 5.1 PROCEDIMENTOS DE AMOSTRAGEM

Os locais de amostragem foram numerados de acordo com sua distância do canal principal do Rio Marapanim, com o número 1 na margem do rio Marapanim (Figura 8a), e os números 2 e 3 (Figura 8b) em dois canais secundários de maré dispostos ao longo da floresta de manguezal de Marapanim. A distância entre os sites P1 e P2 é de 2,3 km, enquanto o site P3 está localizado a cerca de 1 km do site P2. As posições geográficas dos testemunhos são: P1 ( $22^{\circ}58.507'S$  e  $41^{\circ}58.990'W$ ), P2 ( $22^{\circ}93.056'S$  e  $43^{\circ}11.092'W$ ) e P3 ( $22^{\circ}54.680'S$  e  $43^{\circ}50.749'W$ ).



Figura 9 – Foto da planície lamosa dos canais de maré do ponto 1 (a) e do ponto 2 (b) na maré baixa.

#### 5.1.1 Sedimento

As coletas de amostras foram realizadas no período de maior (abril/2017) e menor (setembro/2017) precipitação. Em cada ponto de amostragem foram coletados (através de mergulho autônomo) dois testemunhos, mediante a inserção de tubo de acrílico (50 cm de comprimento,  $\varnothing = 8$  cm) verticalmente no substrato durante a maré baixa de quadratura ( $< 1m$ ), para recuperar  $\sim 35$  cm da camada sedimentar, incluindo a água de fundo. Imediatamente após a coleta os testemunhos foram acomodados em caixa de isopor sendo transportados ao laboratório (improvisado próximo a área de coleta) para posteriores tratamentos e análises. Um testemunho foi destinado às leituras de pH e Eh, e extração da água intersticial, e o segundo testemunho para as análises no sedimento.

Os testemunhos destinados para as análises no sedimento foram fatiados em intervalos de 1 cm até 6 cm de profundidade, a seguir em intervalos de 2 cm até a profundidade de 20 cm,

e finalmente em intervalos de 5 cm até a profundidade de 35 cm. Dentro de um *glove bag* sob atmosfera de N<sub>2</sub>, uma fração de sedimento úmido (~10 g) foi estocada em tubos de polietileno e fixada com 15 mL de acetato de zinco Zn(Ac)<sub>2</sub> 20 %, para a determinação de sulfetos voláteis em ácido (AVS = FeS + ΣH<sub>2</sub>S) e *chromium reducible sulfur* (CRS = FeS<sub>2</sub> + S<sub>0</sub>), o restante das amostras foi acondicionado em sacos de plásticos, preservadas em gelo e posteriormente transportadas para o laboratório, até posterior análises.

### 5.1.2 Parâmetros Físico-Químicos

A salinidade, pH e Eh (mV) das amostras de sedimentos foram medidas *in situ*. Os testemunhos para a medição dos parâmetros físico-químicos foram coletados em tubos previamente perfurados ( $\varnothing = 1$  cm, em intervalos de 2 em 2 cm, em duas sessões verticais). A leitura do pH e potencial redox (Eh) foram feitas inicialmente na água de fundo, após esta leitura foi retirada toda a água de fundo sobrejacente ao sedimento para continuar com a leitura do pH e Eh no testemunho (Figura 9). Isto foi necessário para que não houvesse escape de água de fundo para o restante do testemunho. Para as leituras de pH e Eh utilizou-se o pHmetro da marca Metrohm 826 pH mobile. A salinidade foi obtida por refratômetro de campo manual da marca Atago.



Figura 10 - Leitura do pH e Eh no testemunho.

### 5.1.3 Extração da água de fundo e da água intersticial

Os testemunhos para extração de água intersticial foram mantidos na vertical e fixados em suporte universal. A água de fundo foi coletada em triplicata. A água de fundo e intersticial,

para as análises das espécies dissolvidas de  $\text{Fe}^{2+}$ ,  $\text{Mn}^{2+}$ ,  $\text{SO}_4^{2-}$ ,  $\text{Cl}^-$ ,  $\text{NH}_4^+$ ,  $\text{PO}_4^{3-}$ ,  $\Sigma\text{H}_2\text{S}$  ( $\Sigma\text{H}_2\text{S} = \text{H}_2\text{S} + \text{HS}^- + \text{S}_0 + \text{S}_x^{2-}$ ) e alcalinidade, foram extraídas através do sistema Rhyzon® (SeeBerg-Elverfeldt *et al.* 2005, Shotbolt 2010) (Figura 10). Os rizomas, com uma seção filtradora de 7 cm e 1  $\mu\text{m}$  de porosidade, foram conectados a seringas de 20 mL que permitiram a extração da água de fundo e intersticial sem causar problemas de oxidação da amostra. A inserção dos rizomas para a extração da água de fundo foi de 3 cm acima da interface água-sedimento, extraíndo-se em média 14 mL de água, em torno de 5 minutos. Para a extração da água intersticial, as seringas foram deixadas no sedimento durante 4 horas, em média 13 mL foram extraídos, e a resolução da inserção dos rizomas nos testemunhos foi de 2 cm até 20 cm de profundidade, de 5 cm até o final dos perfis.

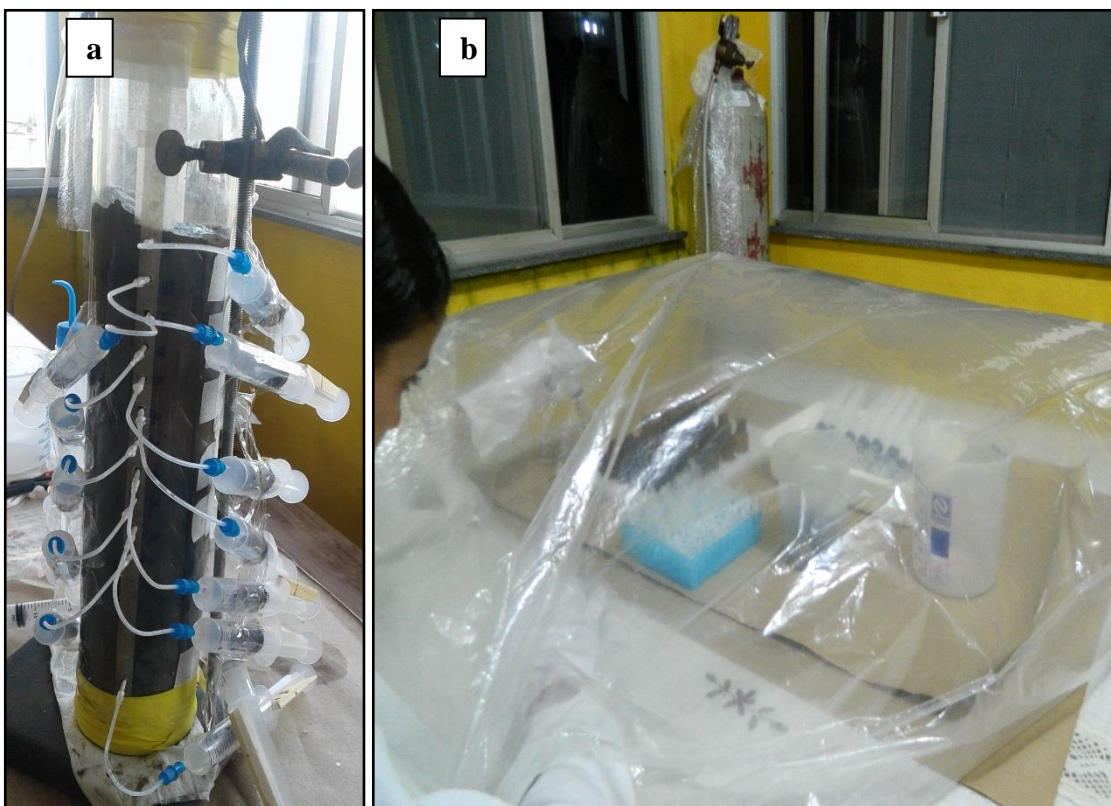


Figura 11 - Extração de água intersticial do sedimento utilizando o sistema Rhyzon® e separação das amostras para análise em *glove bag* sob atmosfera de  $\text{N}_2$

Para evitar oxidação das amostras, após finalizada a extração das águas intersticiais, as seringas foram colocadas dentro do *glove bag* sob atmosfera de  $\text{N}_2$  (Figura 8b), as amostras contidas nas seringas foram separadas em alíquotas, acondicionadas e fixadas de acordo com a Tabela 2. Em seguida, as amostras para análises de amônio foram congeladas e as demais foram refrigeradas a 4°C, até posteriores análises químicas.

Tabela 2 - Parâmetros de espécies dissolvidas, volumes das alíquotas de água de fundo e intersticial, tipo de frascos utilizados e soluções fixadoras adicionadas nas respectivas alíquotas.

Parâmetros	Volume (mL)	Frascos	Fixadores
Sulfeto	1	Eppendorf	100µL de Zn(Ac) <sub>2</sub> 5%
Metais	2	Eppendorf	100µL de HNO <sub>3</sub> 1%
Fosfato	1	Âmbar	10µL de HCl PA
Cloreto + Sulfato	1	Eppendorf	-
Amônio	1	Âmbar	-
Alcalinidade	2	Âmbar	-

De acordo com Seeberg-Elverfeldt *et al.* (2005) a resolução vertical mínima dentro de um perfil de água intersticial com a utilização de Rhizons é equivalente à área de drenagem próxima a seção filtradora. Uma primeira estimativa da área de influência pode ser calculada através do raio ( $r$ ) do tubo que contém o sedimento (cilindro do testemunho), o qual representa a alíquota de sedimento correspondente a amostra de água intersticial extraída. Assim, o raio desta área de drenagem pode ser calculado através da Equação 1.

$$r = \sqrt{\frac{V_{\text{amostra}}}{\phi \cdot \pi \cdot l}} \quad (\text{Equação 1})$$

Sendo que  $V_{\text{amostra}}$  é o volume de amostra coletado em mL,  $\phi$  é a porosidade do sedimento e  $l$  é o comprimento da seção filtradora em cm, que neste caso é 7 cm.

Os volumes de água intersticial coletados nos sedimentos de Marapanim foram em média 13 mL, com raio drenagem <1 cm. Assim, todos os valores encontrados para os raios de drenagem estão dentro do intervalo de resolução utilizado, não abrangendo as profundidades adjacentes (superiores e inferiores). Segundo este resultado, foi considerado neste trabalho que as amostras de água intersticial coletas de fato representam os intervalos de profundidade a qual foram atribuídas.

#### 5.1.4 Vegetação e fitoplâncton

A coleta do fitoplâncton e da vegetação foi realizada apenas durante a estação de maior precipitação (maio de 2017). Aproximadamente 15 folhas frescas de seis diferentes árvores adultas de cada espécie dominante de mangue (*Rhizophora* spp., *Avicennia germinans* e *Laguncularia racemosa*) foram coletadas. As folhas foram lavadas em água desionizada para retirada das partículas sedimentares aderidas e do sal, em seguida as amostras foram congeladas e

liofilizadas. As amostras de fitoplâncton foram coletadas ao longo dos canais de maré do manguezal durante as marés de cheia ( $n = 3$ ); arrastes horizontais foram realizados na superfície da água (profundidade máxima de 50 cm), utilizando uma malha de plâncton padrão, com abertura de malha de 64  $\mu\text{m}$ . Esta abertura de malha é a mais utilizada nos estuários amazônicos devido à forte hidrodinâmica local (Paiva *et al.* 2006). Cada amostra foi observada em microscópio binocular após ser lavada em água deionizada e submetida a peneiramento úmido (abertura de malha 20  $\mu\text{m}$ ) para remoção de partículas contaminantes (folhas e cascas) ou possíveis predadores do zooplâncton. Por fim, as amostras foram congeladas e liofilizadas.

### **5.1.5 Aquisição de imagens de drone e processamento**

Uma terceira etapa de campo foi realizada em novembro de 2019 para aquisição de imagens de alta resolução (3 cm) da área de estudo, as quais foram obtidas usando um Drone Phantom 4 DJI (câmera digital FC 330 4K/12MP). Os dados planialtimétricos foram processados pelos softwares Agisoft Photoscan versão 1.6.1 (AgisoftPhotoScan, 2018) e Global Mapper versão 19 (GlobalMapper 2017). Os dados planialtimétricos de dez pontos de controle de solo foram adquiridos por um smartphone conectado a uma Antena Trimble Catalyst com um Sistema Global de Navegação por Satélite (GNSS) diferencial. Uma correção submétrica ( $\pm 30$  cm), fornecida pelo website da Trimble mediante o pagamento de uma assinatura (<https://geospatial.trimble.com/catalyst-subscriptions>), foi aplicada aos dados GNSS. A vegetação foi classificada manualmente por fotointerpretação no Software Global Mapper. Árvores de *Rhizophora*, *Avicennia* e *Laguncularia* foram identificadas de acordo com a cor, geometria e textura do dossel. Este trabalho seguiu os procedimentos descritos pelo desenvolvedor de software (Agisoft 2018, "Global Mapper User's Manual" 2020) e adaptado para áreas de manguezal (Cohen *et al.* 2018, 2019).

## **5.2 ANÁLISES QUÍMICAS**

### **5.2.1 Água de fundo e intersticial**

As análises das espécies dissolvidas  $\text{NH}_4^+$ ,  $\text{PO}_4^{3-}$ ,  $\Sigma\text{H}_2\text{S}$ , sílica e alcalinidade foram realizadas no Laboratório de análises químicas do Museu Paraense Emílio Goeldi;  $\text{SO}_4^{2-}$  e  $\text{Cl}^-$  foram determinados por cromatografia no Laboratório de cromatografia do Instituto de Geociências da UFPA. Elementos maiores e menores ( $\text{Fe}^{2+}$ ,  $\text{Mn}^{2+}$ ,  $\text{Na}^+$ ,  $\text{K}^+$ ,  $\text{Ca}^{2+}$  e  $\text{Mg}^{2+}$ ) foram determinados por ICP-OES no Laboratório de análises químicas do Instituto Evandro Chagas.

### 5.2.1.1 Alcalinidade

A alcalinidade foi determinada imediatamente após a extração da água de fundo e intersticial, por titulação potenciométrica de 2 mL de amostra com HCl 0,01 N (Figura 9), adaptado do método de Gran (1952), seguida por plotagem dos pontos da curva de titulação. O método de Gran (1952) baseia-se no fato de que a principal reação, após o ponto de neutralização, é o aumento de  $[H^+]$  devido à adição de um excesso de ácido. Assim, basta estabelecer essa reta a partir de 4-5 pontos obtidos após o ponto de equivalência ( $pH \approx 3,8$ ), é possível traçar a reta correspondente à função de Gran, que é uma regressão linear, contra o volume de HCl adicionado.



Figura 12 - Instrumentação para titulação potenciométrica de pequenos volumes de água intersticial.

### 5.2.1.2 Fosfato ( $PO_4^{3-}$ )

O método de determinação dos ortofosfatos baseia-se na reação em meio ácido do ortofosfato, com o ácido molíbdico, produzindo ácido fosfomolíbdico. O ácido fosfomolíbdico é reduzido pelo ácido ascórbico um dos redutores mais convenientes, uma vez que foi introduzido antimônio, para acelerar sua ação redutora. O tempo de desenvolvimento da cor não ultrapassa 10 minutos. A absorbância foi determinada por espectrofotometria no comprimento de onda de 885 nm, conforme o método de Gieskes *et al.* (1991).

### 5.2.1.3 Amônio ( $\text{NH}_4^+$ )

O íon amônio reage com o fenol, em meio alcalino, para formar um complexo azul, o indofenolato, cuja absorbância é medida em 630 nm, no espectrofotômetro, conforme o método de Gieskes *et al.* (1991).

### 5.2.1.4 Sulfeto ( $\sum\text{H}_2\text{S}$ )

O método colorimétrico padrão de determinação do sulfeto dissolvido é baseado na reação do N,N-dimetil-p-fenileno diamina com  $\text{H}_2\text{S}$  em presença de  $\text{Fe}^{3+}$ , que conduz à formação de um complexo colorido, o azul de metileno, cuja absorbância é medida, no espectrofotômetro, em um comprimento de onda de 670 nm (Cline, 1969). Este método permite determinar a concentração total, ou seja, a soma das três formas:  $\text{H}_2\text{S}$ ,  $\text{HS}^-$  e  $\text{S}^{2-}$ . Portanto, neste trabalho as diferentes formas de sulfeto na água intersticial serão expressas como  $\sum\text{H}_2\text{S}$ .

### **Avaliação dos métodos de análise por espectrofotômetro**

Os métodos, como antes descritos, são clássicos e amplamente utilizados, no entanto necessita verificação da resposta do espectrofotômetro e soluções utilizadas, assim como as estimativas do limite de detecção, a recuperação e o desvio padrão para todos os métodos utilizados. A recuperação consistiu em se aplicar o método analítico a uma solução padrão de concentração conhecida (Tabela 3). Caso método associado ao espectrofotômetro estiver com uma resposta positiva, o resultado obtido estará próximo ao esperado. Para cada analito foram feitas quintuplicatas, onde tirou-se a média e o desvio padrão (DP).

Na Tabela 3 são apresentadas as concentrações esperadas e as recuperações para cada analito, bem como o limite de detecção e desvio padrão dos métodos. Para todas as variáveis estudadas, as recuperações dos métodos estão próximas aos valores esperados, dentro de uma faixa de erro aceitável, isto é, 80-120% de acordo com Standard methods: for examination of water and wastewater (Apha 2006).

Tabela 3 - Avaliação dos métodos analíticos por espectrofotômetro, recuperação, DP e LD.

Analito	Padrão	Concentração ( $\mu\text{M}$ )	Recuperação %	DP	LD ( $\mu\text{M}$ )
Sulfeto	ZnS	10	98	0,06	0,03
Amônio	NH <sub>4</sub> Cl	70	102	2,7	2,6
Fosfato	KH <sub>2</sub> PO <sub>4</sub>	10	97	0,6	0,24

#### 5.2.1.5 Sulfato ( $\text{SO}_4^{2-}$ ) e cloreto ( $\text{Cl}^-$ )

As concentrações de  $\text{SO}_4^{2-}$  e  $\text{Cl}^-$  foram determinadas através da cromatografia iônica, modelo Dionex-DX- 120, com alíquotas diluídas em 1:500 com água Milli-Q. Para a aquisição dos dados, foi empregado o software Chromeleon. O método utilizado está de acordo com o descrito no método 9056A Standard Methods for the Examination of Water & Wasterwater.

#### 5.2.1.6 Metais dissolvidos ( $\text{Fe}^{2+}$ e $\text{Mn}^{2+}$ )

As concentrações de  $\text{Fe}^{2+}$  e  $\text{Mn}^{2+}$  dissolvidos na água de fundo e intersticial (diluição simples de 10 vezes) foram determinadas por ICP-OES VISTA-MPX. O controle de qualidade foi efetuado pela análise do material de referência TMDA-51.4 “Trace Elements in Water” (Environmental Canada), 1640a e 1643e “Trace Elements in Natural Water” (National Institute of Standards & Tecnology-NIST), nas mesmas condições utilizadas para as amostras (n=6). As concentrações obtidas dos metais encontram-se dentro do intervalo de variação certificado, portanto considera-se que a metodologia utilizada foi adequada (Tabela 4).

Tabela 4 - Média das concentrações de  $\text{Fe}^{2+}$  e  $\text{Mn}^{2+}$  ( $\mu\text{M}$ ) obtidas e certificadas nos padrões TMDA-51.4, 1640a e 1643e.

MRC	Concentração	Fe	Mn
1640a	Obtida	0,67	0,67
	Certificada	0,65	0,74
	Recuperação (%)	104	91
1643b	Obtida	1,70	0,59
	Certificada	1,68	0,69
	Recuperação (%)	101	85
TMDA 51,2	Obtida	2,4	1,22
	Certificada	2,2	1,52
	Recuperação (%)	113	81

## 5.2.2 Sedimentos

### 5.2.2.1 Pré-tratamento

As amostras de sedimento (úmidas) foram pesadas diretamente no erlenmeyer e levadas a peso constante em estufa a 50°C. Os pesos das amostras úmidas e secas foram anotados para o cálculo da porosidade do sedimento. Uma parte da amostra seca foi descarbonatada através da reação com ácido clorídrico (HCl) 1N até as amostras ficarem com o pH abaixo de 2. Após a descarbonatação completa, a amostra foi transferida para um tubo falcon previamente pesado e identificado, em seguida foi lavada adicionando-se água destilada no tubo e a centrifugando por 5 minutos a 3500 rpm. O sobrenadante foi descartado e o processo (lavagem e centrifugação) repetido pelo menos 3 vezes (até que o pH da água de lavagem = 7). As amostras foram secas em estufa a 50°C até peso constante.

### 5.2.2.2 Porosidade e densidade

A porosidade do sedimento foi definida e calculada como a fração de volume de água no sedimento úmido. O volume de água foi determinado pela diferença nos pesos das amostras de sedimento antes e após a secagem do sedimento úmido a 60 °C até peso constante. A densidade aparente seca (DBD, g cm<sup>-3</sup>) foi determinada como o peso do sedimento seco (g) dividido pelo volume inicial (cm<sup>3</sup>) da amostra.

### 5.2.2.3 Granulometria

As análises granulométricas foram determinadas no Laboratório de Mineralogia e Geocíquímica Aplicada (LAMIGA) da UFPA. Para determinar as distribuições das frações granulométricas utilizou-se o Analisador de Partículas a Laser, ANALYSETTE 22, FRITSCH. Para esta análise uma amostra de ~2g foram previamente tratadas com peróxido de hidrogênio (H<sub>2</sub>O<sub>2</sub>) em placa aquecedora para remoção da matéria orgânica. Para auxiliar na dispersão das partículas após o ataque à matéria orgânica, adiciona-se hexametafosfato de sódio (Na<sub>16</sub>P<sub>14</sub>O<sub>43</sub> – 9 g.L<sup>-1</sup>) e, submetem-se as amostras à agitação por 24 horas. Foi utilizado o software GRADISTAT 9.1 (Blott & Pye 2001) para o tratamento dos resultados, onde a escala granulométrica foi modificada de Udden (1914) e Wentworth (1922), com a classificação de argila (<2μm), silte (2-63μm) e areia (> 63 μm).

#### 5.2.2.4 Geocronologia e Taxa de sedimentação

Todas as datações das amostras de sedimento foram realizadas na National Marine Science Centre da Southern Cross University, na Austrália. Para datar os sedimentos, as atividades de radionuclídeos da série de decaimento  $^{238}\text{U}$  foi medida em um detector de gama de poços de germânio de alta pureza (HPGe) com eficiência de 40% acoplado a um analisador multicanal. Os sedimentos em cada intervalo foram selados em tubos gama por pelo menos três semanas para estabelecer o equilíbrio secular entre o  $^{226}\text{Ra}$  e seus produtos filhos  $^{214}\text{Pb}$  e  $^{214}\text{Bi}$ . As atividades de  $^{210}\text{Pb}$  foram determinadas pela medição direta de picos gama de 46,5 KeV, enquanto a atividade de  $^{226}\text{Ra}$  foi calculada pela média dos picos de suas filhas  $^{214}\text{Pb}$  e  $^{214}\text{Bi}$  (295,2 KeV) (351,9 KeV) (609,3 KeV) (Sanders *et al.* 2016). O excesso de atividade  $^{210}\text{Pb}$  ( $^{210}\text{Pb}_{\text{ex}}$ ) foi estimado subtraindo o  $^{226}\text{Ra}$  da atividade total de  $^{210}\text{Pb}$ . A taxa de acumulação de sedimentos (TAS) foi calculada de acordo com o método de Concentração Inicial Constante (CIC), uma vez que uma diminuição líquida de valor inferior nas atividades  $^{210}\text{Pb}_{\text{ex}}$  foi observada em todos os três núcleos, implicando em uma taxa consistente de sedimentação (Appleby e Oldfield 1992). As taxas de acumulação (0-35 cm) e estoques (para 0-30 cm) de COT, NT e PT foram estimados para cada intervalo de profundidade (cm), usando valores de TAS (cm a<sup>-1</sup>), DBD (g cm<sup>-3</sup>) e COT, NT bem como conteúdo de PT (g g<sup>-1</sup>), respectivamente:

$$\text{Taxa de acumulação (g.m}^{-2}.\text{ano}^{-1}) = [\text{TAS}] \times [ps] \times [\text{teor de COT, NT ou PT}]$$

$$\text{Stocks (g.m}^{-2}) = [ps] \times [\text{profundidade}] \times [\text{teor de COT, NT ou PT}]$$

#### 5.2.2.5 Composição elementar e isotópica da matéria orgânica

A composição elementar e isotópica do carbono orgânico total (COT) e nitrogênio total (NT) nitrogênio dos sedimentos, folhas e fitoplâncton, foram medidas para identificar as fontes de MO que contribuem para a caracterização da coluna sedimentar em cada ponto de amostragem. Uma subamostra de cada intervalo do testemunho foi acidificada para remover o material carbonato; em seguida, foi lavado em água desionizada, seca (60 °C) e moída em pó antes das análises de TOC e  $\delta^{13}\text{C}$ . TN e  $\delta^{15}\text{N}$  foram analisados em subamostras não acidificadas. As assinaturas isotópicas ( $\delta^{13}\text{C}$  e  $\delta^{15}\text{N}$ ) e os conteúdos de TOC e TN foram analisados usando um Leco Flash Elemental Analyzer acoplado a um espectrômetro de massa de razão de isótopos Thermo Fisher Delta V (Thermo Flash EA 1112). A precisão analítica foi a seguinte: TOC = 0,1%, TN = 0,1%,  $\delta^{13}\text{C} = 0,1\text{‰}$  e  $\delta^{15}\text{N} = 0,15\text{‰}$ . Os padrões de trabalho foram usados (glicose,

10,7 ppt e ureia, 41,3 ppt) para calibrar para  $\delta^{13}\text{C}$ . Um par de padrões foi medido a cada 20 amostras. Esses padrões foram calibrados inicialmente com os padrões absolutos internacionais LSVEC e NIST8542. Os resultados de COT e NT expressos em % neste trabalho, foram convertidos em  $\mu\text{mol g}^{-1}$  peso seco de sedimento para calcular as relações molares individuais COT/NT. A composição elementar e isotópica do carbono orgânico total e nitrogênio total foram realizadas no laboratório do Centro Nacional de Ciências Marinhas da *Southern Cross University*, na Austrália.

#### 5.2.2.6 Fósforo total (PT)

A análise de fósforo total (PT) foi determinada em amostra de sedimento digerido de acordo com o procedimento de digestão ácida proposta por Aspila *et al.* (1976). Uma amostra de 0,3 g de sedimento (seca e macerada) foi pesada em cadinho de porcelana, levando-o à mufla a temperatura de 550°C por 4 horas. Após a perda ao fogo, transferiu-se as amostras para tubos de centrífuga e adiciona-se 10 mL da solução de HCl 1 N, colocando-os em agitação mecânica por 16 horas. Após a agitação, as amostras foram centrifugadas por 10 minutos (3000 rpm). Descartou-se o material precipitado e analisou-se o teor de P (como ortofosfato) no extrato sobrenadante. A determinação do ortofosfato foi efetuada de acordo com Gieskes *et al.* (1991). Essa análise foi realizada no Laboratório de Análises Química do Museu Paraense Emílio Goeldi (MPEG).

#### 5.2.2.7 Fe e Mn reativos

Fe e Mn reativos ( $\text{Fe}_R$  e  $\text{Mn}_R$ ) foram determinados usando reagente ascorbato (50 g  $\text{NaHCO}_3$ , 50 g citrato de sódio, 20 g ácido ascórbico para 1 L de solução, tamponado a pH 8 (Kostka e Luther 1994, Anschutz *et al.* 2005). As extrações foram realizadas em 500 mg de sedimento seco em 10 mL de reagente ascorbato, desgaseificado com  $\text{N}_2$ , por 24 h sob agitação contínua. O sobrenadante foi diluído 10 vezes com  $\text{HNO}_3$  (1,0 %). As concentrações de Fe e Mn foram medidas por espectrometria de absorção atômica com padrão externo preparado na mesma matriz, no laboratório de análises químicas do Museu Paraense Emílio Goeldi.

### 5.2.2.8 Enxofre total (ST)

Para as análises de enxofre total, aproximadamente 3 mg de amostra de sedimento seco e macerado foi pesado em capsula de estanho e determinadas em um analisador elementar CHNS (PerkinElmer), no laboratório do Museu Paraense Emílio Goeldi.

### 5.2.2.8 Destilação AVS-CRS

Amostras previamente fixadas com Zn(Ac)<sub>2</sub> foram centrifugadas por 10 min. a 3000 rpm para a retirada do Zn(Ac)<sub>2</sub>. AVS e CRS (*acid-volatile sulfur* e *chromium-reducible sulfur*) foram determinados em 1 g de sedimento por destilação em duas etapas. O AVS foi analisado por destilação fria ácida (16 mL, HCl 6 N) com fluxo contínuo de N<sub>2</sub>, enquanto o CRS através de destilação quente (80°C) em solução ácida de Cr<sup>2+</sup> (16 mL, 2 N). Em ambas as destilações o H<sub>2</sub>S lixiviado do sedimento foi fixado quantitativamente em armadilhas de 10 mL de Ac(Zn)<sub>2</sub> (20%), e sua concentração foi determinada por espectrofotometria (670 nm), de acordo com o método colorimétrico descrito por Cline (1969). Essas análises foram realizadas no Laboratório de Biogeoquímica da Universidade Federal Fluminense.

### 5.2.2.9 Morfologia da pirita

A análise da morfologia da pirita foi realizada em amostra total (seca e macerada) em microscópio eletrônico de varredura-MEV (TESCAN MIRA3) com sistema de energia dispersiva-EDS (Oxford instruments x-act), no Laboratório de MEV/EDS do MPEG. As amostras foram montadas nos suportes para MEV usando-se fita de carbono e cola de prata, e então metalizados com ouro. As análises químicas por MEV/EDS nessas amostras ocorreram em condições de 15 kV e as imagens de 5 kV.

## 5.3 FLUXOS DIFUSIVOS NA INTERFACE ÁGUA-SEDIMENTO

As estimativas de fluxos difusivos de nutrientes (NH<sub>4</sub><sup>+</sup> e PO<sub>4</sub><sup>3-</sup>) e metais (Fe<sup>2+</sup> e Mn<sup>2+</sup>) entre os sedimentos e a água sobrejacente foram calculadas a partir dos gradientes de concentração interfacial, de acordo com a primeira lei de difusão de Fick (Berner 1980) representada pela Eq. (2) abaixo:

$$F = -\Phi D_s(\Delta C / \Delta Z) \quad (2)$$

onde  $F$  ( $\text{mmol.m}^{-2}.\text{d}^{-1}$ ) é o fluxo difusivo,  $\Phi$  (adimensional) é a porosidade na superfície do sedimento (profundidade = 0-1 cm),  $D_s$  ( $\text{m}^2.\text{s}^{-1}$ ) é a difusão molecular coeficiente no sedimento, e  $\Delta C/\Delta Z$  é o gradiente de concentração através da interface água-sedimento. De acordo com esses cálculos, fluxos negativos indicam fluxos de entrada da água de fundo para o sedimento, enquanto fluxos positivos indicam fluxos de saída do sedimento para as águas de fundo. A  $\Phi$  foi determinada de acordo com o item 4.2.2.2.  $\Delta C/\Delta Z$  foi assumido como representado pela diferença entre a concentração na água de fundo e na concentração de água intercial. O coeficiente de difusão ( $D_s$ ) foi calculado a partir do coeficiente de difusão molecular em água livre  $D_0$  corrigido para a porosidade e temperatura do sedimento (Li & Gregory 1974). A porosidade na camada superior do sedimento variou de 0,51 a 0,76. As temperaturas da água sobrejacente estavam entre 27,7 e 29,3 °C.

#### 5.4 ANÁLISES ESTATÍSTICA

As análises estatísticas foram realizadas usando o pacote estatístico PAST versão 3.26 (Hammer *et al.* 2001). A análise de variância unilateral (ANOVA) foi usada para avaliar a diferença significativa de uma única variável (por exemplo, argila, silte, areia, TOC, TN, TP,  $\delta^{13}\text{C}$ ,  $\delta^{15}\text{N}$ , salinidade, pH, entre outros) entre os locais de amostragem (P1, P2 e P3) e estações (chuvelha e seca), com um teste post hoc Tukey HSD para distinguir relações de pares entre pontos de amostragem. A normalidade da distribuição dos dados foi testada usando Shapiro-Wilk antes da análise estatística. Quando as variáveis não foram normalmente distribuídas, elas foram transformadas em logaritmo para se ajustar a uma distribuição normal. Significância estatística em  $\alpha < 0,05$  foi usada para todos os testes. A Análise de Componentes Principais (PCA) foi aplicada para identificar as relações multivariadas entre as variáveis geoquímicas. Fatores significativos foram selecionados com base em autovalores  $> 1$ . A relação entre cada par de variáveis foi medida pelo coeficiente de correlação de Pearson. Coeficientes de correlação maiores que 0,5 foram considerados significativos.

## 6 RESULTADOS E DISCUSSÕES

Os resultados e discussões foram organizados em dois artigos. O primeiro artigo foi publicado na revista *Marine Geology*, online em 12 de agosto de 2020, e investigou o potencial dos sedimentos de canais de maré dos manguezais de Marapanim – PA, para sequestrar C, N e P em seus sedimentos, além de avaliar as fontes da MO sedimentar. Para isso determinou-se as concentrações, estocagens e acúmulo de C, N e P nos sedimentos de manguezais mediante o uso de indicadores geocronológicos, elementares e isotópicos. O segundo artigo foi submetido à revista *Biogeochemistry*, e investigou a influência da precipitação sazonal nas propriedades físico-químicas, nos processos diagenéticos e na troca de nutrientes e metais na interface água – sedimento dos canais de maré estudados, para isso uma série de análises químicas foram realizadas na água intersticial, além de enxofre total, pirita, e ferro e manganês reativos no sedimento.

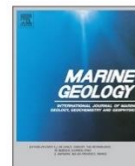
## 6.1 ARTIGO 1: CARBON AND NUTRIENT ACCUMULATION IN TROPICAL MAN-GROVE CREEKS, AMAZON REGION

Marine Geology 429 (2020) 106317



Contents lists available at ScienceDirect

**Marine Geology**  
journal homepage: [www.elsevier.com/locate/margeo](http://www.elsevier.com/locate/margeo)



### Carbon and nutrient accumulation in tropical mangrove creeks, Amazon region



Christiene R.L. Matos<sup>a,\*</sup>, José F. Berrêdo<sup>b,\*</sup>, Wilson Machado<sup>c</sup>, Christian J. Sanders<sup>d</sup>, Edouard Metzger<sup>e</sup>, Marcelo C.L. Cohen<sup>a</sup>

<sup>a</sup> Programa de Pós-Graduação em Geologia e Geoquímica, Universidade Federal do Pará, Belém, Pará, Brazil

<sup>b</sup> Museu Paraense Emílio Goeldi/MCTIC, Belém, Pará, Brazil

<sup>c</sup> Programa de Pós-Graduação em Geoquímica, Universidade Federal Fluminense, Niterói, Rio de Janeiro, Brazil

<sup>d</sup> National Marine Science Centre, Southern Cross University, Coffs Harbour, New South Wales, Australia

<sup>e</sup> Laboratoire des Bio-Indicateurs Actuels et Fossiles, UMR6112 CNRS LPG-BIAF, Université d'Angers, Angers, France

#### ARTICLE INFO

**Keywords:**  
Blue carbon  
Organic matter source  
Macrotidal estuary  
Creek mudflat  
Brazilian Amazon coast

#### ABSTRACT

The Marapanim River estuary (MRE) is part of the Amazon estuarine system located in northern Brazil, which is characterized as having extensive mangrove forests. Given that previous studies reported CO<sub>2</sub> and CH<sub>4</sub> fluxes from mangrove creeks in this region, here we investigate the potential organic carbon sequestration of the creek mudflats to get a better understanding of the carbon cycling through these systems. Sediment accumulation rates derived from <sup>210</sup>Pb dating indicated that sampled cores represent the previous 24 ( $\pm 4$ ) yr. The approximately 24-year total organic carbon (TOC), total nitrogen (TN) and total phosphorus (TP) burial rates were estimated to be 192.5 ( $\pm 43.5$ ), 15.3 ( $\pm 4.1$ ) and 3.2 ( $\pm 0.8$ ) g m<sup>-2</sup> yr<sup>-1</sup>, respectively. A binary source mixing model based on carbon stable isotopes ( $\delta^{13}\text{C}$ ) revealed that the sedimentary organic matter (OM) is mainly influenced by marine phytoplankton input (49% to 95%). Furthermore, the TOC accumulation rates found here were slightly higher than the global averages estimated for within mangrove forests, suggesting that these unaccounted carbon sinks along creek mudflat environments are relevant for carbon budgets in mangrove-colonized coastal zones. The highest contents, stocks and accumulation rates were found in the tidal creek sediments that are most influenced by nearby mangroves and are more protected than sediments from major river margins. Our results indicate that the creek mudflats play a major role in carbon and nutrients sequestration, directly related to grain size and OM sources.

#### 1. Introduction

Mangrove forests, along with other vegetated coastal ecosystems such as seagrasses and saltmarshes, are recognized as blue carbon ecosystems due to their capacity to sequester carbon at a far higher rate than terrestrial forests (Nellemann et al., 2009; Mcleod et al., 2011). Although mangrove forests occupy < 1% of the global coastal area, these ecosystems sequester and store high amounts of organic carbon in plant biomass and sediment, contributing 10–15% to coastal sediment carbon storage and exporting 10–11% of the particulate terrestrial carbon to the ocean (Jennerjahn and Ittekkot, 2002; Dittmar et al., 2006; Alongi, 2014). For instance, the carbon stocks in the Amazon mangroves are over twice those of upland evergreen forests and almost 10-fold those of tropical dry forests (Kauffman et al., 2018), which

underscores their potential value to mitigating greenhouse gas emissions.

Two important measurements used in determining the rate of organic carbon sequestration are the sediment total organic carbon (TOC) content and the sediment accumulation rate (SAR). The first term provides information about the TOC stock sequestered in sediments (Howard et al., 2014). The SAR is used to measure the TOC accumulation rates, which address the question of how much TOC is sequestered in a specified period and quantifies the ongoing sink capacity (Arias-Ortiz et al., 2018; Wang et al., 2019). From the <sup>238</sup>U decay series, the <sup>210</sup>Pb dating method has been an ideal tracer for dating aquatic sediments deposited during the previous 100 years, enabling the determination of TOC accumulation rates in vegetated coastal ecosystems (Smoak et al., 2013; Marchio et al., 2016; Sanders et al., 2016; Sasmito

\* Corresponding authors at: Museu Paraense Emílio Goeldi, Av. Perimetral, 1901 – CEP, 66077-830 Belém, Pará, Brazil.

E-mail addresses: christienematos@hotmail.com (C.R.L. Matos), berredo@museu-goeldi.br (J.F. Berrêdo), wmachado@geoq.uff.br (W. Machado), christian.sanders@scu.edu.au (C.J. Sanders), edouard.metzger@univ-angers.fr (E. Metzger), mcohen80@hotmail.com (M.C.L. Cohen).

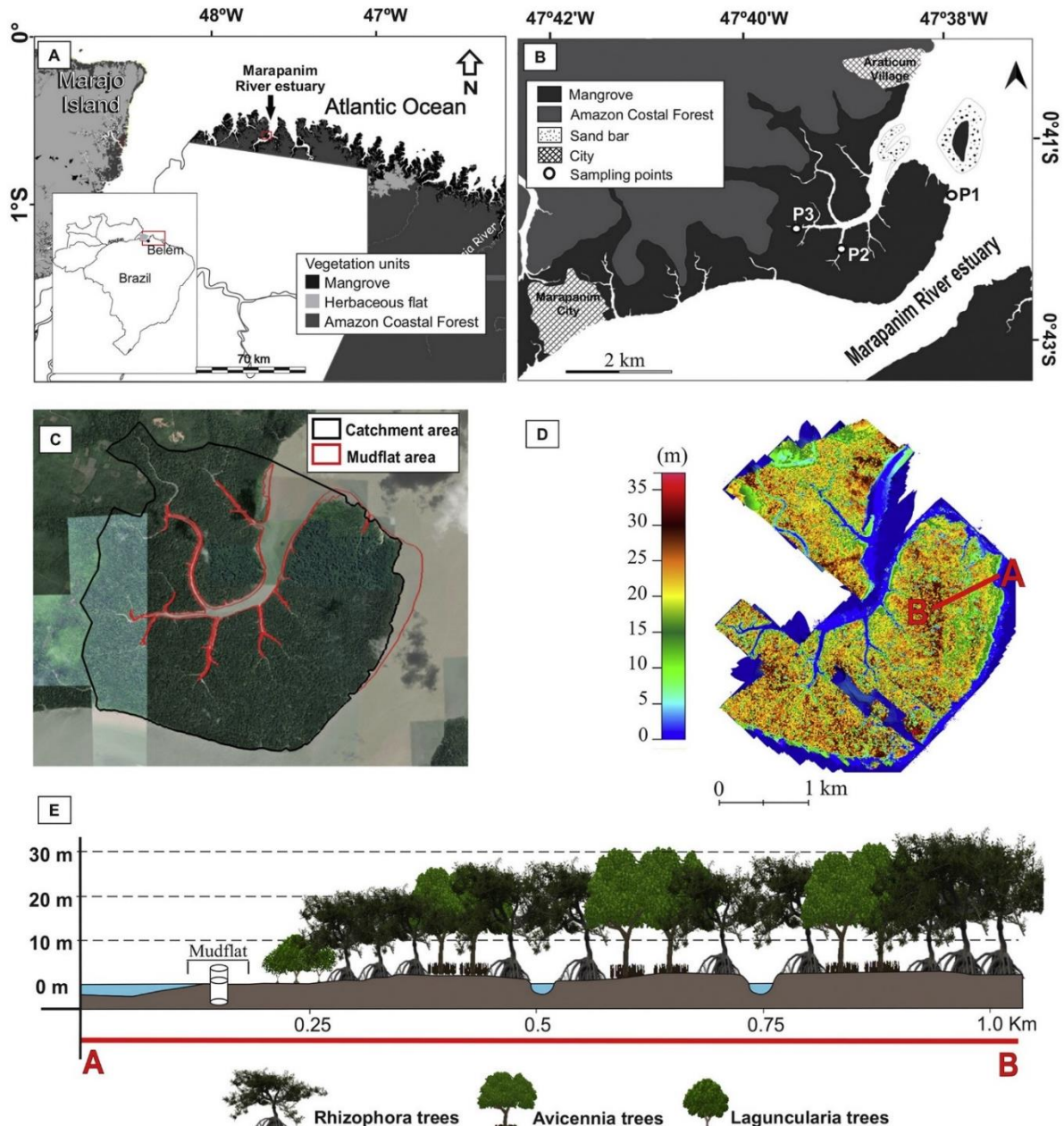


**Fig. 1.** (A) and (B) Map of the study area in Marapanim estuarine mangrove, Brazil. (B) Sampling location (P1, P2 and P3). (C) Catchment and mudflat areas related to the sampling sites. (D) Digital vegetation height model. (E) The diagrammatic mangrove forest distribution and positioning of the sampled cores in the mud tidal flat mangrove sediments. Black dashed lines represent the height of the mangrove.

et al., 2020).

Total organic carbon to total nitrogen ratios TOC/TN ratios, and carbon and nitrogen stable isotope signatures ( $\delta^{13}\text{C}$  and  $\delta^{15}\text{N}$ ) have been widely used as effective geochemical proxies to estimate the relative proportions of terrigenous and marine OM in estuarine and coastal sediments (Lamb et al., 2006; Ranjan et al., 2011; Liu et al., 2015; Vilhena et al., 2018; Kusumaningtyasa et al., 2019). Previous studies have shown that the terrestrial OM is preserved, stored and

accumulates more efficiently than marine-derived OM in sediments (Hedges et al., 1997; Ranjan et al., 2011; Watanabe and Kuwae, 2015; Kusumaningtyasa et al., 2019), due to the selective preservation of refractory OM at the expense of labile components, which is more susceptible to degradation by microorganisms (Hedges et al., 1997; Zonneveld et al., 2010). Therefore, identifying the source of OM is important in evaluating the effectiveness of the mangrove ecosystems as blue carbon sinks, since the variability of the origin of the OM stored

in sediments contributes differently to longer-term carbon burial.

Data on the contribution of intertidal creek environments are more limited than mangrove forests as carbon sinks. However, intertidal mudflats situated along mangrove creeks can play an important role in the carbon cycling of tropical land-sea interfaces, such as acting as a conduit for exchanges between mangrove forests and coastal waters. For instance, Call et al. (2019) demonstrated that a mangrove tidal creek in the Amazon region presented large CO<sub>2</sub> and CH<sub>4</sub> fluxes, suggesting that recent global estimates of these fluxes, based mostly on data from higher latitudes (exceeding 5°) without considering macro-tidal mangrove system, may be underestimated. Moreover, tidal creeks may be more sensitive to land-use changes than open water systems due to a broader connectivity with watersheds, implying that OC accumulation rate changes by up to one order of magnitude in response to urban effluents input (Darrow et al., 2017). Therefore, the balance between carbon export, and sediment burial may present an important conduit to the mangrove and coastal ocean carbon cycle.

The Brazilian coastal region holds, over 960,000 ha, the third-largest mangrove area worldwide (Giri et al., 2011) including the North coast of Brazil (known as the Brazilian Amazon coast) which is considered the largest continuous and best-preserved mangrove forest in the world (Nascimento et al., 2013; Kauffman et al., 2018). The mangroves of the Marapanim River estuary (MRE) are part of this extensive range of mangroves on the Brazilian north coast, which present minimal anthropogenic impact. Mangroves are enormously important in this region as they sustain traditional communities found on the Amazon coast (Fernandes et al., 2018). Information on the biogeochemical cycling of carbon and nutrients in a non-impacted environment is necessary to better understand how potential changes to the mangrove dynamics may impact the carbon and nutrient fluxes between mangrove forests and coastal waters.

The main goal of this study is to obtain a better understanding of the cycling of sedimentary OM in the Marapanim mangrove estuarine system, located in the Brazilian Amazon region. To this aim, the hypothesis that creek mudflats play an important role as carbon and nutrient sinks, rather than only act as a conduit for carbon and nutrients cycling in coastal regions, was tested. We analyzed TOC, TN and TP stocks (sediment) and accumulation rates, as well as estimated the sources of OM in unvegetated mudflats situated along mangrove creeks to: 1) characterize the different OM sources, and 2) investigate potential relationships between OM sources and TOC, TN, and TP burial based on accumulation rates. In addition, we characterized the mangrove forest, according to topographical gradients of the tidal flats and vegetation heights, since biogeochemical cycles and carbon budgets are also affected by the mangrove structure and environmental conditions (Chambers et al., 2013; Pérez et al., 2018; Steinmüller et al., 2020). As such, we suggest that mangrove characteristics should be considered when comparing the biogeochemical data obtained here with other studies.

## 2. Materials and methods

### 2.1. Study area

The Marapanim River estuary is part of the Amazon estuarine system in Para, Northern Brazil, between 00°30' to 01°00'S and 47°32' to 47°00'W (Fig. 1a). The main River channel has a funnel form, with a length of more than 70 km and a width of 8 km at the mouth (Atlantic Ocean) (Silva et al., 2009). The water in the estuary is extremely mixed as a result of tidal pumping and wave action, with the ocean water penetrating approximately 62 km up the estuary mouth during the dry season and 42 km during the wet season (Berrédo et al., 2008). This system is dominated by a macrotidal regime with semidiurnal tides; with an amplitude range from 3.5 m during neap tide to over 6 m during spring tides.

The coastal region of Para is characterized by a tropical climate,

with a wet season from January to June, and a dry season from July to December, high annual precipitation (2500–3000 mm) and average annual temperature of 27.7 °C (Martorano et al., 1993). The water temperature of the estuary varies from 27 to 30 °C. pH values indicate alkaline conditions during the dry season (7.9 to 8.0) and slightly acidic during wet season (5.7 to 6.7). The salinity at low and high fluvial discharge varies from 24 to 3, respectively, along the estuarine channel (Berrédo et al., 2008).

The estuary is part of the Master Lucindo Marine Extractivist Reserve, a protected Conservation Unit region. The estuary contains 130 km<sup>2</sup> of continuous and pristine mangrove forest (Vilhena et al., 2013). The dominant mangrove species are *Rhizophora* spp., *Avicennia germinans*, and *Laguncularia racemosa*. The trees are tall (up to approximately 35 m, Fig. 1d), generally distributed in mixed forests of *Rhizophora* spp. and *Avicennia germinans*. *Laguncularia racemosa* is found in the mangrove fringe. Saltmarsh vegetation is represented by *Spartina brasiliensis*, which occupies a pioneering position along mudflat accretion areas.

The Marapanim catchment extends over an area of 2500 km<sup>2</sup> (Silva et al., 2009), with no industrial development, where about 28,000 people live. Like other Brazilian Amazon coastal cities, the Marapanim city's economy is based mainly on the sustainable use of natural resources, particularly fishing (crabs, shrimps, mollusks and fish), as well as commerce and tourism (Kjerve and Lacerda, 1993; ICMBio, 2018; Fernandes et al., 2018).

### 2.2. Acquisition of drone images and processing

Very high resolution (3 cm) images of the study area were obtained using a Drone Phantom 4 DJI (FC 330 digital 4 K/12MP camera). The planimetric data were processed by the Agisoft Photoscan version 1.6.1 (AgisoftPhotoScan, 2018), and Global Mapper version 19 (GlobalMapper, 2017). Planimetric data of ten ground control points were acquired by a smartphone connected to an Antenna Trimble Catalyst with a differential Global Navigation Satellite System (GNSS). A sub-metric correction ( $\pm 30$  cm), provided by the Trimble website upon payment of a subscription (<https://geospatial.trimble.com/catalyst-subscriptions>), was applied to the GNSS data. The vegetation was manually classified by photointerpretation in the Global Mapper Software. *Rhizophora*, *Avicennia*, and *Laguncularia* trees were identified according to color, geometry, and texture of the canopy. This work followed procedures described by the software developer (AgisoftPhotoScan, 2018; "Global Mapper User's Manual," 2020) and adapted for mangrove areas (Cohen et al., 2018, 2019). A detailed description of the data processing can be obtained in the supplementary information section.

### 2.3. Field sampling

The sediment core collection was conducted during the wet (May 2017) and dry (Sept 2017) seasons. The sampling sites were situated near the mouth (Atlantic Ocean) of the MRE, along a lobular structure, where mangrove vegetation has developed. We compared tidal mangrove creeks (P2 and P3) with the Marapanim River margin (P1), which is located in an area under the influence of a nearby sand bar (Fig. 1b).

#### 2.3.1. Sediment

One sediment core was collected from the unvegetated mudflat (devoid of macrophytes) at each site by inserting an acrylic tube (50 cm length) vertically into the substrate during low tide. Immediately after extraction, the sediment core was sectioned at 1-cm depth intervals from the core top to 6 cm depth, then 2-cm intervals until the 20 cm depth, finally at 5-cm intervals until the 35 cm depth. The sub-samples were bagged, preserved on ice and then transported to the laboratory. In addition, pore waters were retrieved using Rhyzon® collectors (Seeberg-Elverfeldt et al., 2005) at the same intervals to the solid phase

for salinity analysis. Pore water salinity was measured in situ with a portable refractometer (Atago).

### 2.3.2. Vegetation and phytoplankton

The phytoplankton and vegetation collection was conducted just during the wet (May 2017) season. Approximately 15 fresh leaves of six different adult trees of each dominant mangrove species (*Rhizophora* spp., *Avicennia germinans* and *Laguncularia racemosa*) were collected. The leaves were washed in deionized water to remove the adhered sedimentary particles and salt, then the samples were frozen and lyophilized. The phytoplankton samples were collected along the mangrove tidal creek during the flood tides ( $n = 3$ ); horizontal hauls were performed on the water surface (maximal depth 50 cm), using a standard-type plankton mesh, with mesh opening 64  $\mu\text{m}$ . This mesh opening is the most used one in the Amazon estuaries due to the strong local hydrodynamics (Paiva et al., 2006). Each sample was observed in a binocular microscope after it was washed in deionized water and subjected to wet sieving (mesh opening 20  $\mu\text{m}$ ) to remove the contaminant particles (leaves and shells) or possible zooplankton predators. Finally, the samples were frozen and lyophilized.

## 2.4. Analyses and data treatment

### 2.4.1. DBD and grain size

Dry bulk density (DBD,  $\text{g cm}^{-3}$ ) was determined as the dry sediment weight (g) divided by the initial volume ( $\text{cm}^3$ ). From the original wet section, a portion was taken for grain size analysis. The sediment grain size was determined using a Fritsch particle size meter model Analysette 22, after calcium carbonate and OM removal, and dispersion in sodium hexametaphosphate 4% (Loring and Rantala, 1992). The GRADISTAT 9.1 software (Blott and Pye, 2001) was used for treating results, where the grain size scale was modified from Udden (1914) and Wentworth (1922), with the classification of clay (< 2  $\mu\text{m}$ ), silt (2–63  $\mu\text{m}$ ) and sand (> 63  $\mu\text{m}$ ) are established for these fractions.

### 2.4.2. Elemental and stable isotope analysis

Carbon and nitrogen stable isotope ratios of phytoplankton, leaves and sediments were measured to identify the sources of OM contributing to the sediments column at each site. A subsample of each core fraction was acidified to remove carbonate material; then it was washed in deionized water, dried (60 °C) and ground to powder before TOC and  $\delta^{13}\text{C}$  analyses. TN and  $\delta^{15}\text{N}$  were analyzed in non-acidified subsamples. Isotopic signatures ( $\delta^{13}\text{C}$  and  $\delta^{15}\text{N}$ ) and TOC and TN contents were analyzed using a Leco Flash Elemental Analyzer coupled to a Thermo Fisher Delta V isotope ratio mass spectrometer (Thermo Flash EA 1112) (Carvalho et al., 2020). Analytical precision was as follows: TOC = 0.1%, TN = 0.1%,  $\delta^{13}\text{C} = 0.1\text{\textperthousand}$ , and  $\delta^{15}\text{N} = 0.15\text{\textperthousand}$ . Working standards were used (glucose, 10.7 ppt and urea, 41.3 ppt) to calibrate for  $\delta^{13}\text{C}$ . A pair of standards were measured with every 20 samples. These standards were calibrated initially against international absolute standards LSVEC and NIST8542. TP contents in the sediments were determined by colorimetry, according to Grasshoff et al. (1999), following the extraction procedure from Aspila et al. (1976). The results of TOC, TN and TP, expressed in % in this work, were converted to  $\mu\text{mol g}^{-1}$  dry weight sediment to calculate individual TOC/TN/TP molar ratios.

### 2.4.3. Calculation of marine and terrestrial organic matter

The relative proportions of mangrove/terrestrial OM ( $\text{OM}_{\text{terr}}$ ) and marine OM ( $\text{OM}_{\text{mar}}$ ) in sediment cores were estimated using the two end-member mixing model described in Schultz and Calder (1976):

$$F_{\text{terr}} = (\delta^{13}\text{C}_{\text{mar}} - \delta^{13}\text{C}_{\text{sed}})/(\delta^{13}\text{C}_{\text{mar}} - \delta^{13}\text{C}_{\text{terr}}) \times 100 \quad \text{and} \quad F_{\text{mar}} = 100 - F_{\text{terr}} \quad (1)$$

where  $F_{\text{terr}}$  is the contribution from the mangrove/terrestrial fraction,  $F_{\text{mar}}$  is the contribution from the marine fraction,  $\delta^{13}\text{C}_{\text{sed}}$  value of the

sediment interval, and  $\delta^{13}\text{C}_{\text{terr}}$  and  $\delta^{13}\text{C}_{\text{mar}}$  are the terrestrial and marine end-members value, respectively. We estimated the terrestrial (an average of the plants that dominate in the Marapanim mangrove) and marine (phytoplankton-derived OM) end-member  $\delta^{13}\text{C}$  values to be  $-29.9 \pm 1.0\text{\textperthousand}$  ( $n = 18$ ) and  $-23.9 \pm 0.7\text{\textperthousand}$  ( $n = 3$ ), respectively, from our results.

### 2.4.4. $^{210}\text{Pb}$ dating and rates of organic carbon, nitrogen and phosphorus accumulation

To date sediments, we measured radionuclide activities from the  $^{238}\text{U}$  decay series in a high-purity germanium (HPGe) well gamma detector with 40% efficiency coupled to a multichannel analyzer. Sediments at each interval were sealed in gamma tubes for at least three weeks to establish secular equilibrium between  $^{226}\text{Ra}$  and its daughter products  $^{214}\text{Pb}$  and  $^{214}\text{Bi}$ . The  $^{210}\text{Pb}$  activities were determined by the direct measurement of 46.5 KeV gamma peaks, while  $^{226}\text{Ra}$  activity was calculated averaging its daughters' peaks  $^{214}\text{Pb}$  and  $^{214}\text{Bi}$  (295.2 KeV) (351.9 KeV) (609.3 KeV) (Sanders et al., 2016). The excess  $^{210}\text{Pb}$  ( $^{210}\text{Pb}_{\text{ex}}$ ) activity was estimated by subtracting the  $^{226}\text{Ra}$  from the total  $^{210}\text{Pb}$  activity. The sediment accumulation rate (SAR) was calculated according to the Constant Initial Concentration (CIC) method as a net downcore decrease in  $^{210}\text{Pb}_{\text{ex}}$  activities was noted in all three cores, implying a consistent rate of sedimentation (Appleby and Oldfield, 1992). Accumulation rates and stocks (for 0–35 cm) of TOC, TN and TP were estimated for each depth interval (cm), using values of SAR ( $\text{cm yr}^{-1}$ ), DBD ( $\text{g cm}^{-3}$ ), and TOC, TN as well as TP contents ( $\text{g g}^{-1}$ ), respectively:

$$\text{Accumulation rates (AR)} (\text{g m}^{-2} \text{yr}^{-1}) = [\text{SAR}] \times [\text{DBD}] \times [\text{TOC}, \text{TN or TP content}] \quad (2)$$

$$\text{Stocks} (\text{g m}^{-2}) = [\text{DBD}] \times [\text{depth}] \times [\text{TOC}, \text{TN or TP content}] \quad (3)$$

### 2.4.5. Statistical analysis

Statistical analyses were performed using statistical package PAST version 3.26 (Hammer et al., 2001). One-way analysis of variance (ANOVA) was used to assess the significant difference of a single variable (clay, silt, sand, TOC, TN, TP,  $\delta^{13}\text{C}$ ,  $\delta^{15}\text{N}$ ) between the sampling sites (P1, P2 and P3) and seasons (wet and dry), with a Tukey HSD post hoc test for distinguishing pairwise relationships among sites. The normality of data distribution was tested using Shapiro-Wilk prior to statistical analysis. When the variables were not normally distributed (clay, silt, sand, TOC, TN and TP), they were log-transformed to fit a normal distribution. Statistical significance at  $\alpha < 0.05$  was used for all tests. Principal Components Analysis (PCA) was applied to identify the multivariate relationships between the geochemical variables. Significant factors were selected based on eigenvalues  $> 1$ . The relation between each pair of variables was measured by Pearson's correlation coefficient. Correlation coefficients greater than 0.5 were considered significant.

## 3. Results

### 3.1. Mangrove structure

The A-B profile (Fig. 1d-e) revealed a young mangrove fringe (1–10 m) mainly represented by *Laguncularia racemosa* in the topographically lowest sector (~1 m above mean sea-level, amsl) of the tidal flat. In an intermediate topography (1–2 m amsl) a dense mangrove forest characterized by *Laguncularia racemosa* and *Rhizophora* spp. (10–20 m tall) was found. Following the topographical gradient (~2 m amsl) a mixed forest of *Avicennia germinans* and *Rhizophora* spp. is noted (20–30 m tall). These trees become taller (25–33 m) in the inner parts of this mangrove forest. The sampling sites P2 and P3 (Fig. 1b) were located in topographically highest areas, inundated only during spring tides, of which sediments are strongly oxidized during the dry season, coexisting with more mature mangroves (15–25 m).

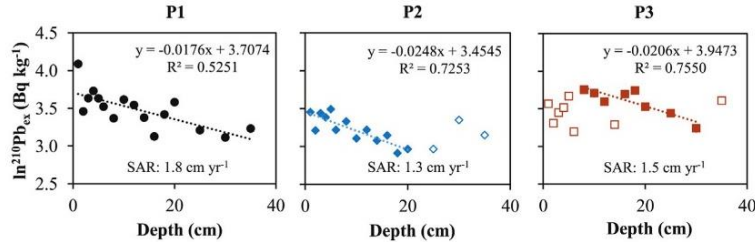


**Fig. 2.**  $\ln^{210}\text{Pb}_{\text{ex}}$  ( $\text{Bq kg}^{-1}$ ) activities versus depth in the sediment cores (P1, P2 and P3), sedimentation rates were calculated using selected points of  $^{210}\text{Pb}_{\text{ex}}$  profiles (filled symbols). Open symbols correspond to result interpreted as biologically and physically disturbed.

### 3.2. Sediment chronology

The  $\log^{210}\text{Pb}_{\text{ex}}$  of the sedimentary profiles from the three examined sampling sites were depicted by an almost linear decline with depth (Fig. 2), implying a consistent rate of sedimentation. Based on the  $^{210}\text{Pb}_{(\text{ex})}$  profiles, the top 6 cm of the P3 and bottom of the P2 sediment cores were determined to be mixed and therefore, were excluded when calculating SAR. The SAR were calculated as 1.8 (core P1), 1.5 (core P3) and 1.3 (core P2)  $\text{cm yr}^{-1}$ , respectively (Fig. 2), with a regional mean of  $1.5 \pm 0.3 \text{ cm yr}^{-1}$ . According to the extrapolated  $^{210}\text{Pb}_{\text{ex}}$ -derived age, sediment at the core basis corresponds to an age of about 1997 year in P1 (35 cm), 1989 year in P2 (35 cm) and 1994 in P3 (35 cm).

### 3.3. Grain size and dry bulk density

The textural composition of the sediments was mostly sand and silt (34–80% of silt, 12–64% of sand) with a low percentage of clay (< 10%) (Fig. 3). This textural distribution differs among the three sites ( $p < 0.05$ , Table 2), with the distribution of fine-grained higher at sites P2 and P3 compared with P1 (Fig. 3). The contents of the grain size fractions also showed significant seasonal variations (Table 2), except to silt at P3 and sand at P1 and P2. In general, values of DBD ( $\text{g cm}^{-3}$ ) in the sediment sites increased substantially with the depth (Fig. 3). The highest DBD was found in the P1, exceeding  $1.0 \text{ g cm}^{-3}$ , where the sedimentary profile graded to predominately sand.

### 3.4. Elemental and isotopic composition

The values and vertical profiles of elemental and isotopic composition for the sediments, plants and phytoplankton are shown in Table 1 and Fig. 3. Differences in TOC, TN, TP contents of sediments between sampling locations and seasons (except to TN at site P3) were statistically significant (Table 2). The range of TOC was highest at sites P2 (2.28 to 3.84%) and P3 (2.21 to 3.04%) compared to P1 (0.53 to 1.91%). The range of TN was similar to P2 (0.19 to 0.27%) and P3 (0.19 to 0.26%) compared to P1 (0.04 to 0.17%). Like TOC and TN, TP contents was much larger in the P2 (0.028 to 0.052%) and P3 (0.033 to 0.059%) than to P1 (0.009 to 0.044%). In all three sites, TOC, TN and TP contents decreased slightly with depth.

The  $\delta^{13}\text{C}$  values of sediments varied from  $-26.9$  to  $-24.2\text{\textperthousand}$ , with significant difference between sites ( $p < 0.05$ ). The downcore  $\delta^{13}\text{C}$  profile was relatively homogeneous at site P1, without significant difference between seasons ( $p > 0.05$ ), with an average of  $-25.2 \pm 0.4\text{\textperthousand}$ . However, P2 and P3 showed significant differences between seasons ( $p < 0.05$ ), due to results from upper 18 cm, with highest values during dry season, with average of  $-25.7 \pm 0.6\text{\textperthousand}$  and  $-25.2 \pm 0.5\text{\textperthousand}$ , compared to wet season, with average of  $-26.6 \pm 0.2\text{\textperthousand}$  and  $-26.3 \pm 0.2\text{\textperthousand}$ , respectively.

The  $\delta^{15}\text{N}$  values of sediments did not differ significantly between seasons ( $p > 0.05$ ), but differed significantly between sites ( $p < 0.05$ ). The  $\delta^{15}\text{N}$  values ranged from 5.1 to 8.4‰, with an average

of  $6.1 \pm 0.8\text{\textperthousand}$  to P1,  $5.9 \pm 0.6\text{\textperthousand}$  to P2 and  $6.5 \pm 0.3\text{\textperthousand}$  to P3. Downcore profiles of  $\delta^{15}\text{N}$  showed a small increase with depth, excepted for site P1 that showed oscillations and no tendency with depth, with a peak at 14 cm.

Differences in TOC/TN molar ratios between sampling locations and seasons were statistically significant (Table 2), varying from 12 to 18.5, with an average of  $15.3 \pm 1.3$  to P1,  $15.6 \pm 1.3$  to P2 and  $13.7 \pm 0.8$  to P3. Downcore profiles of TOC/TN showed a small increase with the depth at all sites. The TN/TP molar ratios in sediments were not significantly different in terms of spatial variability ( $p > 0.05$ ), but were significantly different seasonally, with highest ratios in the wet season, varying from 8.3 to 13.3, compared to dry season, that varied from 2.9 to 11.8.

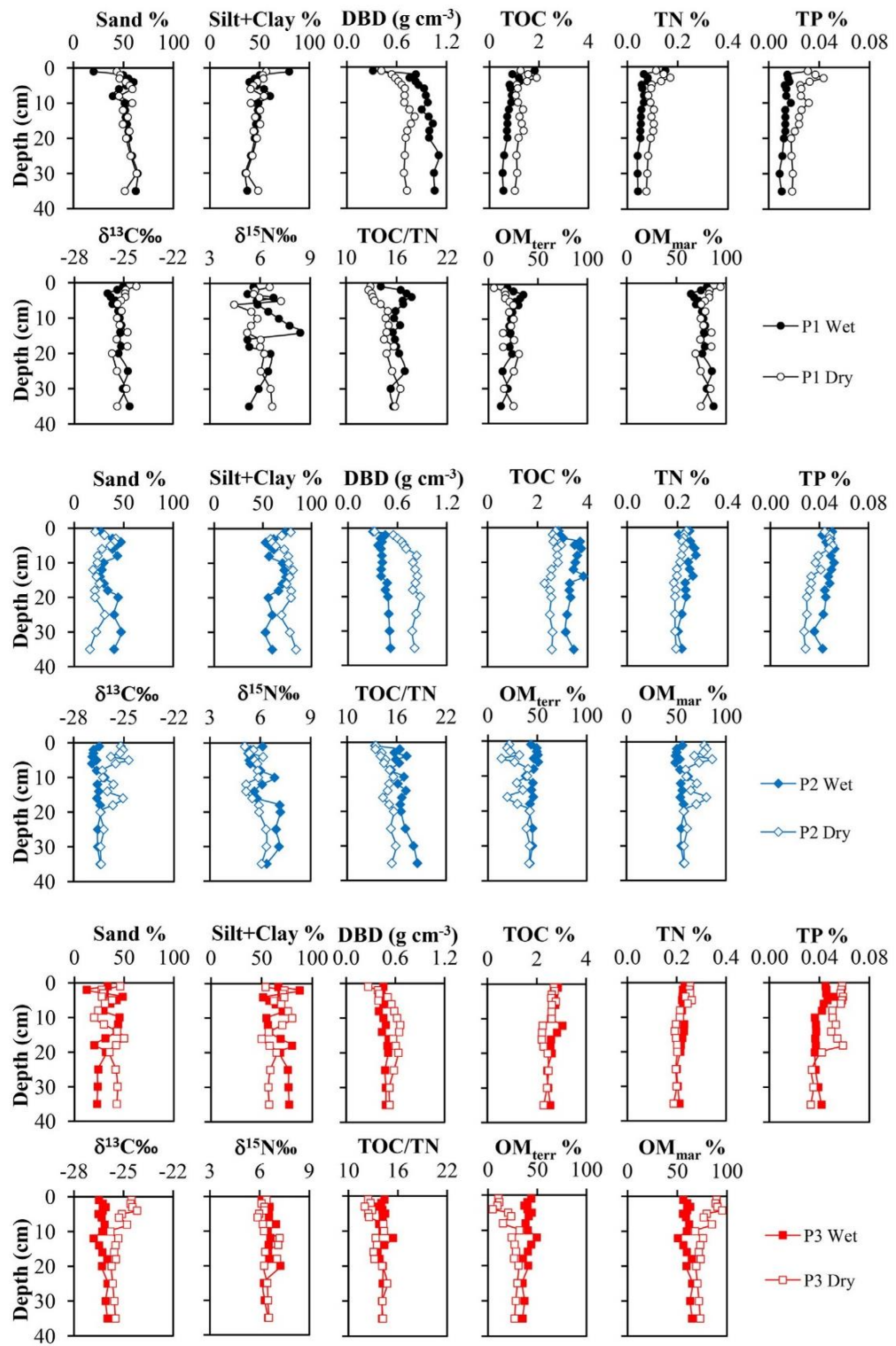
The  $\delta^{13}\text{C}$  values of *Rhizophora* spp., *Avicennia germinans* and *Laguncularia racemosa* leaves were similar and ranged from  $-31.8$  to  $-28.2\text{\textperthousand}$  ( $29.8 \pm 1.0\text{\textperthousand}$ ), which is within the range of C<sub>3</sub> terrestrial plants. The  $\delta^{15}\text{N}$  and TOC/TN values varied slightly from species to species from 1.7 to 6.4‰ ( $4.4 \pm 1.3\text{\textperthousand}$ ) and from 30.0 to 40.1 ( $34.0 \pm 3.2$ ), respectively. The phytoplankton presented  $\delta^{13}\text{C}$  values from  $-24.4$  to  $-23.4\text{\textperthousand}$  ( $23.9 \pm 0.7\text{\textperthousand}$ ),  $\delta^{15}\text{N}$  from 3.2 to 3.7‰ ( $3.4 \pm 0.4\text{\textperthousand}$ ), and TOC/TN from 6.9 to 7.2 ( $7.1 \pm 0.2$ ).

### 3.5. Principal Component Analysis (PCA)

The significant components (i.e., eigenvalue > 1) loading matrix of PCA are listed in Table 3. The PCA (Fig. 4) showed that the first two components together explained 74.5% of the data variation. The first component (PC1) accounted for the largest proportion with 61.7% of the total variance. It showed significant positive loading ( $> 0.5$ ) for TN, TOC, TP, silt and clay, and negative loading of sand and  $\delta^{13}\text{C}$ . The first component explained the variations between the sites, separating the site P1 from P2 and P3 due to its high sand content (Fig. 4a). This component also gives strong evidence of TOC, TN and TP increase with increase of silt and clay, with the highest TOC, TN and TP contents for P2 and P3 (Fig. 4b). The second component (PC2) explained 12.9% of the total variance and showed significant loading only for  $\delta^{15}\text{N}$ .

### 3.6. Proportions of organic matter sources

The proportions of terrestrial ( $\text{OM}_{\text{terr}}$ ) and marine ( $\text{OM}_{\text{mar}}$ ) OM sources were derived from the  $\delta^{13}\text{C}$  data and Eq. (1). Downcore profiles of  $\text{OM}_{\text{mar}}$  and  $\text{OM}_{\text{terr}}$  remained relatively constant throughout the sediment columns during the wet season, but during the dry season an increase in marine input in the upper layers ( $< 18$  cm) was observed at sites P2 and P3 (Fig. 3). Relatively high proportions of  $\text{OM}_{\text{mar}}$  were observed at all sites in both wet and dry seasons. Overall,  $\text{OM}_{\text{mar}}$  varied from 49.1 to 95.2% and  $\text{OM}_{\text{terr}}$  from 4.8 to 50.9% (Table 1). In the wet season,  $\text{OM}_{\text{mar}}$  contribution was highest in the site P1 (76.4%) compared to sites P2 (54.5%) and P3 (60%). During dry season,  $\text{OM}_{\text{mar}}$  increased to 79.6, 69 and 78% at sites P1, P2 and P3, respectively.



(caption on next page)

**Fig. 3.** Depth profiles of grain size, DBD, TOC, TN, TP,  $\delta^{15}\text{N}$ ,  $\delta^{13}\text{C}$  and TOC/TN (molar ratio) for the sediment cores (P1, P2 and P3). Including proportions of terrestrial ( $\text{OM}_{\text{terr}}$ ) and marine ( $\text{OM}_{\text{mar}}$ ) sedimentary OM, during wet (filled circles) and dry (open circles) seasons.

### 3.7. Stocks and accumulation rates

The TOC, TN and TP accumulation rates and stocks are shown in Fig. 5 and Table 4. The TOC, TN, and TP accumulation rates were estimated from SAR, DBD and TOC, TN and TP content results (Eq. (2)). The downcore sediment densities along with the TOC, TN and TP contents were used to determine stocks (Eq. (3)), the stocks were calculated to 30 cm sediment depth for the three sampling sites. The TOC, TN and TP accumulation rates showed significant site-difference ( $p < 0.05$ ), with a regional mean of  $192.5 \pm 50.6 \text{ g m}^{-2} \text{ yr}^{-1}$  for TOC,  $15.3 \pm 4.3 \text{ g m}^{-2} \text{ yr}^{-1}$  for TP and  $3.2 \pm 1.0 \text{ g m}^{-2} \text{ yr}^{-1}$  for TN. The highest TOC, TN, and TP accumulation rates were measured at sites P2 (C: 218.7, N: 16.4, and P:  $3.1 \text{ g m}^{-2} \text{ yr}^{-1}$ ) and P3 (C: 215.8, N: 18.4, and P:  $3.9 \text{ g m}^{-2} \text{ yr}^{-1}$ ) and the lowest were measured at site P1 (C: 143.2, N: 11.0, and P:  $2.7 \text{ g m}^{-2} \text{ yr}^{-1}$ ). The TOC, TN and TP stocks also differed significantly among the three sites ( $p < 0.05$ ), with a regional mean of  $3811 \pm 1389 \text{ g m}^{-2}$  for TOC,  $296 \pm 109 \text{ g m}^{-2}$  for TN and  $58 \pm 15 \text{ g m}^{-2}$  for TP. Similarly, the TOC, TN and TP stocks were higher at sites P2 (C: 5217.8, N: 386.3, P:  $64.9 \text{ g m}^{-2}$ ) and P3 (C: 3878.6, N: 325.8, P:  $55.4 \text{ g m}^{-2}$ ) than P1 (C: 2337.5, N: 177.1, P:  $17.1 \text{ g m}^{-2}$ ).

**Table 2**

One-way ANOVA for different geochemical parameters in the sediment cores (P1, P2 and P3), during wet and dry seasons. Superscript lowercase letters indicate statistically equal means by the Tukey post hoc test.

Parameters	Between sites		Between seasons ( <i>p</i> value)		
	( <i>p</i> value)	Tukey test	P1	P2	P3
TOC	< 0.05	P2 <sup>a</sup> P3 <sup>b</sup> P1 <sup>c</sup>	< 0.05	< 0.05	< 0.05
TN	< 0.05	P2 <sup>a</sup> P3 <sup>a</sup> P1 <sup>b</sup>	< 0.05	< 0.05	0.69
TP	< 0.05	P2 <sup>a</sup> P3 <sup>a</sup> P1 <sup>b</sup>	< 0.05	< 0.05	< 0.05
$\delta^{13}\text{C}$	< 0.05	P1 <sup>a</sup> P2 <sup>b</sup> P3 <sup>b</sup>	0.14	< 0.05	< 0.05
$\delta^{15}\text{N}$	< 0.05	P3 <sup>a</sup> P1 <sup>b</sup> P2 <sup>b</sup>	0.36	0.07	0.29
TOC/TN	< 0.05	P1 <sup>a</sup> P2 <sup>a</sup> P3 <sup>a</sup>	< 0.05	< 0.05	< 0.05
TN/TP	0.11	P1 <sup>a</sup> P2 <sup>a</sup> P3 <sup>a</sup>	< 0.05	< 0.05	< 0.05
Clay	< 0.05	P2 <sup>a</sup> P3 <sup>a</sup> P1 <sup>b</sup>	< 0.05	< 0.05	< 0.05
Silt	< 0.05	P2 <sup>a</sup> P3 <sup>a</sup> P1 <sup>b</sup>	< 0.05	< 0.05	0.51
Sand	< 0.05	P1 <sup>a</sup> P2 <sup>b</sup> P3 <sup>b</sup>	0.14	< 0.05	0.29
TOC AR	< 0.05	P3 <sup>a</sup> P2 <sup>b</sup> P1 <sup>c</sup>			
TN AR	< 0.05	P3 <sup>a</sup> P2 <sup>b</sup> P1 <sup>c</sup>			
TP AR	< 0.05	P3 <sup>a</sup> P2 <sup>b</sup> P1 <sup>c</sup>			
TOC Stocks	< 0.05	P2 <sup>a</sup> P3 <sup>a,b</sup> P1 <sup>b</sup>			
TN Stocks	< 0.05	P2 <sup>a</sup> P3 <sup>a</sup> P1 <sup>b</sup>			
TP Stocks	< 0.05	P2 <sup>a</sup> P3 <sup>a</sup> P1 <sup>b</sup>			

**Table 1**

Minimum, maximum, mean values and standard deviation ( $\pm \text{SD}$ ) of TOC, TN and TP contents, TOC/TN and TN/TP molar ratios, and  $\delta^{15}\text{N}$  and  $\delta^{13}\text{C}$  for the sediment cores (P1, P2 and P3), plants (Avicennia (Avi.), Laguncularia (Lag.), Rhizophora (Rhi.)) and phytoplankton (phy), including proportions of terrestrial ( $\text{OM}_{\text{terr}}$ ) and marine ( $\text{OM}_{\text{mar}}$ ) sedimentary OM.

	P1		P2		P3		Avi.	Lag.	Rhi.	Phy.	
	Wet	Dry	Wet	Dry	Wet	Dry					
TOC (%)	Min	0.5	1.0	2.8	2.3	2.4	2.2	42.1	37.9	41.3	10.3
	Max	1.8	1.9	3.8	2.9	3.0	2.8	44.2	45.1	44.9	11.0
	Mean	0.9	1.3	3.4	2.6	2.7	2.5	43.0	41.2	42.9	10.6
	SD	0.3	0.2	0.3	0.2	0.2	0.2	0.9	2.6	1.5	0.5
TN (%)	Min	0.04	0.08	0.20	0.19	0.20	0.19	1.2	1.3	1.3	1.7
	Max	0.15	0.17	0.27	0.24	0.23	0.26	1.6	1.9	1.5	1.8
	Mean	0.06	0.10	0.24	0.21	0.22	0.22	1.4	1.5	1.4	1.7
	SD	0.03	0.03	0.02	0.02	0.01	0.03	0.2	0.2	0.1	0.04
TP (%)	Min	0.009	0.018	0.036	0.028	0.036	0.033				
	Max	0.031	0.044	0.052	0.051	0.052	0.059				
	Mean	0.014	0.026	0.047	0.039	0.041	0.050				
	SD	0.005	0.007	0.004	0.008	0.005	0.009				
$\delta^{13}\text{C}$ (‰)	Min	-26.0	-25.7	-26.9	-26.4	-26.8	-25.8	-30.4	-30.4	-31.8	-24.4
	Max	-24.6	-24.2	-26.2	-24.7	-26.0	-24.2	-29.1	-28.2	-30.2	-23.4
	Mean	-25.3	-26.6	-25.7	-26.3	-26.3	-25.2	-29.4	-29.3	-30.8	-23.9
	SD	0.35	0.37	0.2	0.6	0.2	0.5	0.6	0.9	0.6	0.7
$\delta^{15}\text{N}$ (‰)	Min	5.2	4.4	5.3	5.1	6.1	5.9	5.0	2.6	1.7	3.2
	Max	8.4	7.2	7.2	6.4	7.3	7.2	6.4	5.3	4.6	3.7
	Mean	6.2	5.9	6.1	5.7	6.6	6.4	5.7	4.0	3.9	3.4
	SD	0.9	0.7	0.7	0.4	0.4	0.4	0.7	1.2	1.2	0.4
TOC/TN	Min	14.1	12.7	13.4	13.4	13.5	12.0	30.0	28.2	34.5	6.9
	Max	17.8	16.4	18.5	15.9	15.4	14.7	40.1	33.8	36.7	7.2
	Mean	16.2	14.5	16.5	14.8	14.1	13.3	35.0	31.4	35.6	7.1
	SD	0.9	1.1	1.2	0.7	0.4	0.8	4.3	2.3	0.8	0.2
TN/TP	Min	8.3	2.9	10.1	4.5	9.6	3.4				
	Max	11.7	8.1	12.5	11.8	13.7	9.7				
	Mean	9.7	4.3	11.4	5.9	12.0	4.8				
	SD	1.0	1.2	0.7	1.8	1.2	1.5				
OM <sub>terr</sub> (%)	Min	12.6	5.7	38.1	13.8	35.1	4.8				
	Max	35.3	30.8	50.9	42.4	49.4	32.1				
	Mean	23.6	20.4	45.5	31.0	40.1	21.8				
	SD	6.0	6.2	3.4	9.5	3.9	8.7				
OM <sub>mar</sub> (%)	Min	64.7	69.2	49.1	57.6	50.6	67.9				
	Max	87.4	94.3	61.9	86.2	64.9	95.2				
	Mean	76.4	79.6	54.5	69.0	59.9	78.2				
	SD	6.0	6.2	3.4	9.5	3.9	8.7				

**Table 3**

Component loadings of each variable obtained from PCA, variance explained and cumulative variance of the principal components (whole dataset).

Variables	PC1	PC2
Sand	-0.89	-0.02
Silt	<b>0.88</b>	0.01
Clay	0.84	0.14
TOC	0.92	-0.08
TN	0.93	-0.02
TP	0.80	0.05
$\delta^{13}\text{C}$	-0.57	0.19
$\delta^{15}\text{N}$	0.02	<b>0.98</b>
Eigen-values	4.89	1.02
% variance	61.67	12.87
% cumulative	61.67	74.54

Bold values represents the components which show significant positive loading.

#### 4. Discussion

##### 4.1. Sedimentary composition

The mudflat sediments were found to be mainly composed of a mixture containing silt and sand, reflecting a moderately high energetic environment, influenced by tide and fluvial process. The low hydrodynamic flow in the mangrove creeks (P2 and P3) likely caused an increase in the deposition of fine sediments. However, the MRE margin, where P1 was collected, appears to be more affected by tidal currents. In addition, the P1 site is located closer to the sand bar that likely contributed to the increase of fine sand in the sedimentary profile at this study site.

The spatial variations in the grain size distribution of the mudflat sediments play an important role in controlling the OM content. Silt and clay had positive strong to moderate correlation with TOC, TN and TP contents ( $r$  varied from 0.52 to 0.81). The first component of the PCA also indicated strong evidence that TOC, TN and TP increase as the silt and clay increase, with the highest TOC, TN and TP contents for P2 and P3 (Fig. 4a-b). Generally, fine-grained (silt + clay) sediments have higher %TOC than coarse sediments (Canfield, 1994), such relationships may be attributed to the fine-grained sediments which have large specific surface areas that provide higher capacity to adsorb OM (Loring and Rantala, 1992; Mayer, 1994).

The TOC and TN contents measured in the sediments during the

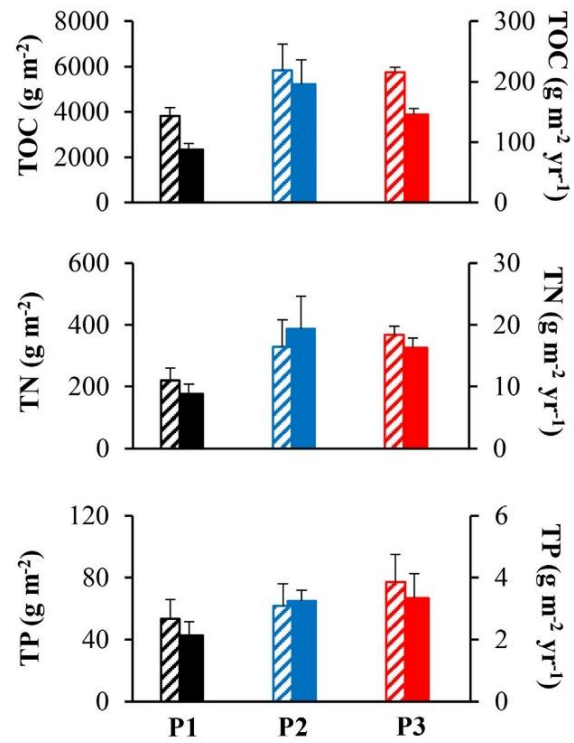


Fig. 5. TOC, TN and TP stocks (solid bars,  $\text{g m}^{-2}$ ) and accumulation rates (striped bars,  $\text{g m}^{-2} \text{yr}^{-1}$ ) in the sediment cores (P1, P2 and P3). The error bars are based on the standard deviation from the average between the wet and dry season dataset.

present study are comparable to those reported in the adjacent coastal areas (Kauffman et al., 2018; Vilhena et al., 2018) and the TP contents are within the global average for mangrove (0.01–0.16%; Alongi et al., 1992). The gradual decrease of TOC, TN and TP content with depth in all cores likely reflect the decomposition of OM by microorganisms as

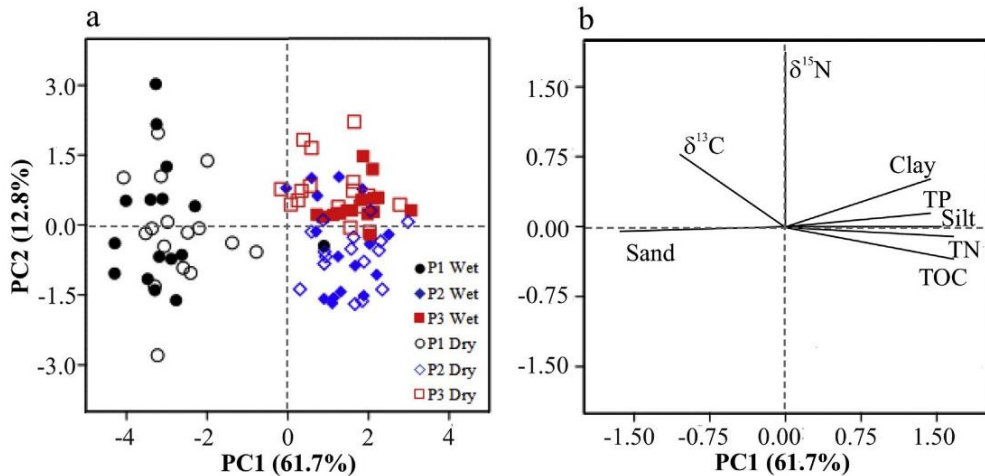
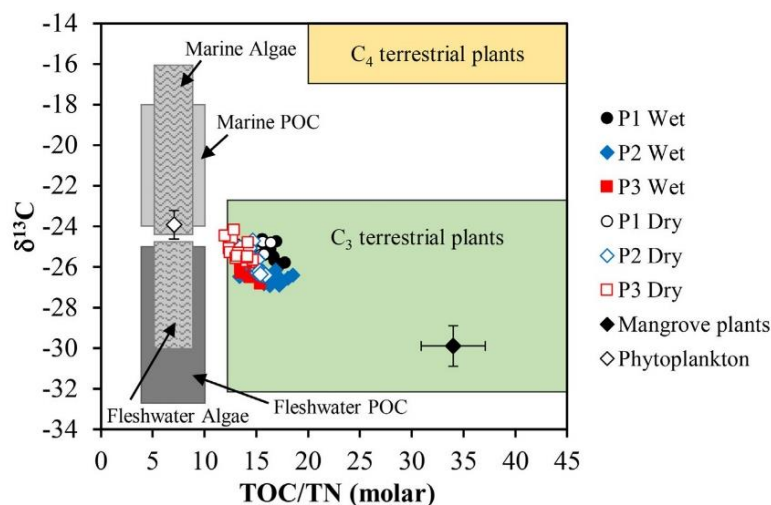


Fig. 4. (a) Principal Component Analysis (PCA) plot showing the multivariate variation among three sites in terms of environmental variables. (b) Vectors indicate the direction and strength of each environmental variable to the overall distribution. The first two principal axes explained 74.5% of the variance.

**Table 4**

The main variation and standard deviation (from each sediment core interval propagate to the average between the wet and dry season dataset) of total organic carbon, total nitrogen and total phosphorous stocks ( $\text{g m}^{-2}$ ) and accumulation rates (AR) ( $\text{g m}^{-2} \text{ yr}^{-1}$ ) for the sediment cores (P1, P2 and P3).

Sites	TOC stock	TOC AR	TN stock	TN AR	TP stock	TP AR
P1	2337 ± 279	143.2 ± 26.3	177 ± 31	11.0 ± 2.4	43 ± 9	2.7 ± 0.7
P2	5218 ± 1084	218.7 ± 48.9	386 ± 107	16.4 ± 4.0	65 ± 7	3.1 ± 0.7
P3	3878 ± 281	215.8 ± 31.2	325 ± 31	18.4 ± 2.4	67 ± 16	3.9 ± 1.0
Overall average	3811 ± 1389	192.5 ± 50.6	296 ± 109	15.3 ± 4.3	58 ± 15	3.2 ± 1.0



**Fig. 6.** Origin of sedimentary OM as indicated by  $\delta^{13}\text{C}$  against TOC/TN (molar ratio). Fields are defined from the compilation of coastal sediments by Lamb et al. (2006). The phytoplankton (white diamond symbol) and Mangrove plants (black diamond symbol) endmember data are taken from the original data in this study.

noted in other systems (Kristensen et al., 2008) or a general increase in the OM content with time. The significant positive correlation between TOC and TN ( $r = 0.96$ ) and TP ( $r = 0.83$ ) in the sediments indicate that the nitrogen and phosphorous in the samples are predominantly associated with the organic fraction.

The TOC/TN/TP molar ratios in sediments were not significantly different in terms of spatial variability, but were significantly different seasonally: 171:11:1 in the wet season and 71:5:1 in the dry season. In both cases the TOC/TN/TP was different from the phytoplankton sources (Redfield: 106:16:1), with TN/TP ratios below 16 that suggest nitrogen to be the limiting factor for phytoplankton growth in these systems. This seasonal variation may be related to the diagenesis of OM. Higher TOC/TN molar ratios in wet than dry season indicate a greater contribution from OM of terrestrial origin, which is more refractory, during the wet season.

#### 4.2. Sources of sedimentary organic matter

Different sources of OM often exhibit distinct elemental (carbon and nitrogen) and/or isotopic signatures ( $\delta^{13}\text{C}$  and  $\delta^{15}\text{N}$ ), representing useful indicators to quantify their relative contribution to the sedimentary OM. For example,  $\text{C}_3$  plants are assumed to have TOC/TN > 12 (Meyers, 1997),  $\delta^{13}\text{C}$  between  $-32\text{\textperthousand}$  and  $-21\text{\textperthousand}$  (Deines, 1980) and  $\delta^{15}\text{N}$  around  $0.4 \pm 0.9\text{\textperthousand}$  (Peterson and Howarth, 1987), while marine-derived OM is characterized by TOC/TN between 5 and 7 (Redfield et al., 1963),  $\delta^{13}\text{C}$  from  $-16\text{\textperthousand}$  to  $-23\text{\textperthousand}$  (Meyers, 1994) and  $\delta^{15}\text{N}$  around  $8.6 \pm 1.0\text{\textperthousand}$  (Peterson and Howarth, 1987).

The potential sources to the sedimentary OM pool in mangrove-estuarine ecosystems can be upland forest and mangrove tissues (fresh leaf, stem, root, and litter), soils from river flow, aquatic macrophytes, microphytobenthos, and phytoplankton (Bouillon et al., 2008; Sasmito

et al., 2020). Some studies have also identified the presence of microphytobenthos as a potential source of OM in mudflats (Gontharet et al., 2014; Gorman et al., 2020), when microphytobenthos layers are visually detectable and thick enough to be sampled and separated from the sediments. However, the presence of microphytobenthos was not visually detectable in our sampling sites, therefore prohibiting the separation and analyses of a potential benthic microalgae endmember. Saltmarsh vegetation (*Spartina* spp.), dominated by  $\text{C}_4$  plants, can be found at the mudflats along MRE. However, given that *Spartina* spp. and their sediments have enriched  $\delta^{13}\text{C}$  signature, ranging from  $-14$  to  $-12\text{\textperthousand}$  and  $-18$  to  $-14\text{\textperthousand}$ , respectively (Curran et al., 1995; Kemp et al., 2010, and references therein), the depleted  $\delta^{13}\text{C}$  values found in sediment samples suggests that *Spartina* spp. is not a major contributor of OM to the studied mudflat sediments. Therefore, we assumed mangrove plants and phytoplankton as the principal OM sources to the mudflats along MRE.

The  $\delta^{13}\text{C}$  values of mangrove leaves ( $-31.8$  to  $-28.2\text{\textperthousand}$ ) are consistent with previously published results from other mangrove-estuarine ecosystems (Bouillon et al., 2008; Prasad and Ramanathan, 2009; Ranjan et al., 2011; Vilhena et al., 2018). The  $\delta^{13}\text{C}$  and  $\delta^{15}\text{N}$  values and TOC/TN molar ratio of phytoplankton (average of  $-23.9 \pm 0.7\text{\textperthousand}$ ,  $3.4 \pm 0.4\text{\textperthousand}$  and  $7.1 \pm 0.2$ , respectively), which we extracted along the studied tidal creek, are close to the marine phytoplankton values. The  $\delta^{13}\text{C}$  values are also similar to the reported value for marine DOC (average  $-23.7\text{\textperthousand}$ ) extracted from Atlantic deep water in the adjacent study area (Dittmar et al., 2006).

The  $\delta^{13}\text{C}$  ( $-26.9$  to  $24.2\text{\textperthousand}$ ) versus TOC/TN (12.0 to 18.5) (Fig. 6) of the sedimentary OM suggests a mixture of sources contributing to the sedimentary OM pool, with a higher contribution of marine phytoplankton ( $\delta^{13}\text{C}$ :  $-23.9 \pm 0.7\text{\textperthousand}$ , TOC/TN:  $7.1 \pm 0.2$ ) than mangrove-derived OM ( $\delta^{13}\text{C}$ :  $-29.8 \pm 1.0\text{\textperthousand}$ , TOC/TN:  $34 \pm 3.1$ ). The  $\delta^{15}\text{N}$

values of sediments (5.2–8.4‰, average of 6.2‰) are within a typical range of aquatic OM produced from assimilation of the nitrate pool. The slight increase of  $\delta^{15}\text{N}$  values and TOC/TN molar ratios with depth, with exception to site P1 in the wet season, suggests anaerobic microbial degradation of OM in the deep reducing sediments (Meyers, 2003; Routh et al., 2009; Jennerjahn, 2012; Prasad et al., 2017). The peak of  $\delta^{15}\text{N}$  at 14 cm in the site P1 during wet season could reflect an event provoked by input from a phytoplankton bloom or accumulation of allochthonous material deposited during and after a high rainfall event.

The consistently similar values of  $\delta^{13}\text{C}$  throughout the sediment column suggest that the source of the depositional OM has been invariable during the past ~25 years at site P1. However, at sites P2 and P3, the enrichment of  $\delta^{13}\text{C}$ , during the dry season compared to wet season, indicated a shift in OM source, because the decomposition of OM usually does not cause a significant enrichment in  $\delta^{13}\text{C}$  (Saintilan et al., 2013), and isotopic fractionation during the decomposition is typically < 3‰. This shift in OM accumulation source may be due to an increase in marine input in the upper layer (< 18 cm), likely associated with a larger sediment mixing provoked by bioturbation in the surface sediments, as the  $\delta^{13}\text{C}$  values were relatively similar along the bottom layers.

The difference in OM source for terrestrial/mangrove C<sub>3</sub> plants ( $\delta^{13}\text{C}$ :  $-29.8 \pm 1.0\text{‰}$ ) vs. marine phytoplankton ( $\delta^{13}\text{C}$ :  $-23.9 \pm 0.7\text{‰}$ ) is distinct and hence, suitable for indicating the OM sources in the study area. However,  $\delta^{15}\text{N}$  values and TOC/TN molar ratios can be unreliable because these may be influenced by diagenetic alterations (Prahl et al., 1997). Additionally,  $\delta^{13}\text{C}$  did not show significant positive correlations with  $\delta^{15}\text{N}$  ( $r < 0.08$ ) and TOC/TN molar ratios ( $r < 0.05$ ) in either the wet or dry season. Therefore, only  $\delta^{13}\text{C}$  was used for the quantification analysis of OM. Based on the assumption of differing OM source input to the mudflat sediments, the end-member mixing model of terrestrial and marine OM showed that the contribution of OM sources varied between sites and seasons (Fig. 3, Table 1).

The OM<sub>mar</sub> predominated in the studied sites likely due to the positioning of the sampling sites, which are situated near the mouth of the MRE (Atlantic Ocean). During the wet season (pore water salinity: 4–20), the OM<sub>mar</sub> contribution was highest in the mudflat sediment from MRE margin (P1: 76.4%) compared to the mangrove tidal creeks (P2: 54.5, P3: 60%). During the dry season (pore water salinity: 18–25), due to less dilution from Marapanim River discharge, the influence of salt water is greater, thereby increasing the contribution of OM<sub>mar</sub> by up to 18% (P1: 79.6, P2: 69 and P3: 78%). Overall, the downcore profiles of OM<sub>mar</sub> and OM<sub>terr</sub> remained relatively constant throughout the sediment columns during the wet season, but during the dry season an increase in marine input in the upper layers (< 18 cm) is noted at sites P2 and P3 (Fig. 3).

#### 4.3. Carbon and nutrient accumulation rates and stocks

The TOC, TN and TP accumulation rates and stocks showed differences between the sites (Table 2, Fig. 5). The highest stocks and accumulation rates were found in the mudflat sediment from mangrove tidal creek (P2 and P3) compared to the MRE margin (P1). Two factors may cause these differences. Firstly, although site P1 presented the highest sedimentation rate (Fig. 2) and highest density (Fig. 3), it is composed of > 50% sand content with lower TOC, TN and TP contents compared to the sites P2 and P3. Previous studies indicated that OM preservation is often enhanced by the large surface area of fine-grained sediments, and the low energy associated with slack water deposits (Mayer, 1994; Keil et al., 1994). Sites P2 and P3 are protected from the direct impact of tidal energy and waves, as compared to site P1 that is located in the MRE margin and close to a sand bar.

The other factor is that the efficiency of OM storage in the mudflat sediments is also dependent on the origin of OM (Saintilan et al., 2013; Watanabe and Kuwae, 2015; Kusumaningtyasa et al., 2019). OM

proportions in our simple end-member mixing model indicated that 49–95% of OM contribution is from marine OM. The slight increase in fluxes of terrestrial OM along the mangrove tidal creek sites (P2 and P3, Table 1) contributed to higher TOC, TN and TP accumulation rates and stocks than those noted from the MRE margin (P1). These results were corroborated with previous studies, which indicated the terrestrial OM is preserved more efficiently than phytoplankton-derived OM in estuarine sediments (Hedges et al., 1997).

The average TOC accumulation rate (TOC AR) calculated in the studied mudflats was slightly higher ( $192.5 \pm 43.5 \text{ g C m}^{-2} \text{ yr}^{-1}$ ) than the global average in conserved mangrove ( $170 \text{ g C m}^{-2} \text{ yr}^{-1}$ , Pérez et al., 2018) and the current global average for mangrove ecosystems ( $179.6 \text{ g C m}^{-2} \text{ yr}^{-1}$ , Alongi, 2020). Higher rates of  $555 \text{ g C m}^{-2} \text{ yr}^{-1}$  were measured in other tropical mudflat in Piraquê-Açu estuary, Brazil, supported by high SAR ( $1.8 \text{ cm yr}^{-1}$ , Bernardino et al., 2020). In contrast, lower carbon accumulation rates were reported in subtropical microtidal creeks systems. For example, Marchio et al. (2016) evidenced TOC AR of  $162 \text{ g C m}^{-2} \text{ yr}^{-1}$  in Southwest Florida, and Santos et al. (2019) observed TOC AR of  $63 \text{ g C m}^{-2} \text{ yr}^{-1}$  in a tidal creek in Evans Head, Australia. However, according Pérez et al. (2018), the distribution of TOC AR within the forests and adjacent sites (margin and mudflat environments) of mangrove ecosystems exhibited non-significant differences among regions, as variations are influenced by a combination of many local factors (e.g. geomorphology, vegetation cover, flooding frequency, hydrological regime and anthropogenic influence).

The average TN and TP accumulation rates were also high (TN:  $15.3 \text{ g m}^{-2} \text{ yr}^{-1}$  and TP:  $3.2 \text{ g m}^{-2} \text{ yr}^{-1}$ ; Table 4) when compared to the global average of anthropogenically non-impacted mangroves (TN:  $8.9 \text{ g m}^{-2} \text{ yr}^{-1}$  and TP:  $0.5 \text{ g m}^{-2} \text{ yr}^{-1}$ , Breithaupt et al., 2014). Similar to our study, Bernardino et al. (2020) measured high TN accumulation rates of  $27.9 \text{ g m}^{-2} \text{ yr}^{-1}$  in a conserved mudflat in Piraquê-Açu estuary. OM enriched in nutrients may be expected to decompose faster and to a larger extent than nutrient-depleted OM (Kristensen and Hansen, 1995; McGlathery et al., 2007). Thereby, the capacity to sequester OC may decrease with an increase in TN and TP burial rates (Breithaupt et al., 2014). However, in our study area TOC AR were higher in the sites with higher TN and TP AR. Similarly, TOC stocks were higher in the sites with higher TN and TP stocks (Table 4).

Due to the relatively shallow sediment depth (30 cm) used in our study, it is difficult to directly compare our results with those from other studies which usually assess sediment stocks based on deeper sediment profiles (e.g.,  $\geq 100 \text{ cm}$ , Howard et al., 2014). However, we found some studies similar to ours with more superficial sampling. Our TOC stocks ranged from 2333 to 5218  $\text{g C m}^{-2}$  (average of  $3811 \text{ g C m}^{-2}$ ), which is similar those mudflat of West Papua, Indonesia (in the top 50 cm,  $6200 \text{ g C m}^{-2}$ , Sasmito et al., 2020), Araçá Bay, Brazil (in the top 20 cm, range from 1700 to  $2200 \text{ g C m}^{-2}$ , Gorman et al., 2020), and for unvegetated mudflats of China (in the top 50 cm,  $4808 \text{ g C m}^{-2}$ , Feng et al., 2019). Comparing our stocks results with the values found in other Amazon mangroves sediments (in the top 30 cm) (supplementary information in Kauffman et al., 2018), our values are within the range of  $3430$ – $6230 \text{ g C m}^{-2}$ , except at site P1 that was relatively lower ( $2337 \pm 279 \text{ g C m}^{-2}$ ), which can be attributed to coarse textured sediments. These results suggest that mudflat along tidal creeks also have a high potential for organic carbon storage compared to vegetated habitats such as mangrove forests.

Few studies have assessed nitrogen and phosphorus stocks in mangrove and mudflat sediments. Feng et al. (2017) measured TN and TP stocks in an unvegetated mudflat of China (in the top 40 cm). Their average of TN stock of  $\sim 290 \text{ g N m}^{-2}$  is comparable to  $296 \pm 109 \text{ g N m}^{-2}$  (Table 4) in our study, but TP stock of  $\sim 150 \text{ g P m}^{-2}$  is higher than what we found of  $58 \pm 15 \text{ g P m}^{-2}$  (Table 4). Saderne et al., (2020) measured TN and TP stocks in mangrove sediments (in the top 20 cm) in the central Red Sea ( $99 \text{ g N m}^{-2}$  and  $70 \text{ g P m}^{-2}$ ) and along the Gulf coast of Saudi Arabia ( $223 \text{ g N m}^{-2}$  and  $32.8 \text{ g P m}^{-2}$ ).

$\text{P m}^{-2}$ ), where TN and TP stocks in the Gulf were quite comparable to what is presented here, but TN stocks were at least twofold higher in the Gulf compared to the Red Sea, while TP stocks were a maximum of 1.2 times higher in Red Sea. Pérez et al. (2017) observed in a conserved mangrove forest in New Zealand estuary TN stock between 400 and 500  $\text{g N m}^{-2}$ , in the top 40 cm, which is slightly higher than our values. In contrast, Ray et al. (2014) and Ray et al. (2017) measured the TN and TP stocks, respectively, in the top 60 cm sediment in the Indian Sundarban mangrove and found an average of 4.2  $\text{g N m}^{-2}$  and 0.4  $\text{g P m}^{-2}$ , which are lower than what we found ( $58 \pm 15 \text{ g P m}^{-2}$ , Table 4), likely as a result of the TN and TP conserved in the living biomass.

The capacity to sequester and store OM in the studied creek mudflats likely reflects the SAR ( $1.5 \pm 0.3 \text{ cm yr}^{-1}$ ), which is higher than the global average in conserved mangrove ( $0.36 \pm \text{cm yr}^{-1}$ ; Pérez et al., 2018) and the current global average ( $0.77 \text{ cm yr}^{-1}$ ; Breithaupt et al., 2012). This high SAR is supported by strong interaction between the river stream and the tides that characterize this environment, being close to the highest global accumulation rates in the mangrove forest (Breithaupt et al., 2012; Kusumaningtyasa et al., 2019) and mudflat (Bernardino et al., 2020). In general, the sedimentation rate is considered as a driving factor controlling the OM burial efficiency (Canfield, 1994). Although the sedimentary OM with a high proportion of marine origin tends to be more susceptible to decomposition, sites with high sedimentation rates contribute significantly to preserve OM (Hedges and Keil, 1995; Canfield et al., 2005). In addition, it should be noted that the studied mangrove area is densely inhabited by *Rhizophora*, *Avicennia* and *Laguncularia* trees, with heights up to 33 m. Therefore, these rates probably reflect a high productivity that provided a large supply of mangrove litter and dead roots to the mangrove creeks through tidal exchange.

Recently, Call et al. (2019) demonstrated that a mangrove tidal creek in Amazon presented large  $\text{CO}_2$  and  $\text{CH}_4$  fluxes from a nearby mangrove tidal creek. However, our results indicate that the Amazon mangrove creeks are also sites that accumulate considerable amounts of organic carbon (Fig. 7). For example, the total mudflat area in the tidal creek catchment of this study was near  $0.5 \text{ km}^2$  (Fig. 1c), and

considering an average of the TOC accumulation rates between the three study sites, we estimate that a total of  $96 \text{ kg TOC yr}^{-1}$  is sequestered in these creeks catchment. This suggests a previously unaccounted carbon sink in creek environments that are relevant to the carbon budgets along mangrove-colonized coastal zones. Therefore, mangrove tidal creeks can play an important role in the carbon cycling in tropical land-sea interfaces more than just acting as a conduit for exchanges between mangrove forests and coastal waters.

Considering global average in conserved mangrove of  $170 \text{ g C m}^{-2} \text{ yr}^{-1}$  (Pérez et al., 2018) and the mangrove forest area within the catchment of this study was  $7,638,368 \text{ m}^2$ , we estimate that a total of  $1299 \text{ t TOC yr}^{-1}$  is sequestered in these mangrove soils. Thus, the creek mudflat area accumulates around 0.007% of what would be estimated for the mangrove forest soils. Carbon dioxide emissions at the water-air interface were  $2794 \pm 2072 \text{ g m}^{-2} \text{ yr}^{-1}$  ( $174 \pm 129 \text{ mmol m}^{-2} \text{ d}^{-1}$ ) from a nearby mangrove tidal creek (Call et al., 2019). Using our creek mudflat area ( $0.5 \text{ km}^2$ ),  $\text{CO}_2$  emissions would be  $1397 \text{ kg C CO}_2 \text{ yr}^{-1}$ , while total mudflat sediment carbon burial would be  $96.3 \text{ kg yr}^{-1}$ . Therefore, sediment carbon sequestration in this system may offset < 7.0% of the aquatic  $\text{CO}_2$  emissions.

## 5. Conclusion

This study investigated the recent ( $24 \pm 4$  years) carbon and nutrient accumulation rates and stocks in intertidal mudflats situated along mangrove creeks within the Brazilian Amazon coast. Even though marine OM was predominant along our study sites (49% to 95%), fine-grained sediments and higher terrestrial OM input, a product of a dense and tall mangroves trees, contributed to higher rates of TOC, TN, and TP accumulation and stocks in the mangrove tidal creeks (P2 and P3) compared to the Marapanim River estuary margin (P1). The capacity to sequester and store TOC also increased with increases in TN and TP burial rates and stocks. Due to the high sedimentation rates ( $1.5 \pm 0.3 \text{ cm yr}^{-1}$ ), the TOC ( $192.5 \pm 43.5$ ), TN ( $15.3 \pm 4.1$ ), and TP ( $3.2 \pm 0.8$ ) accumulation rates found here were slightly higher than the global averages estimated for mangrove forest sediments. The potential of intertidal mudflats to sequester OC suggests that the creek

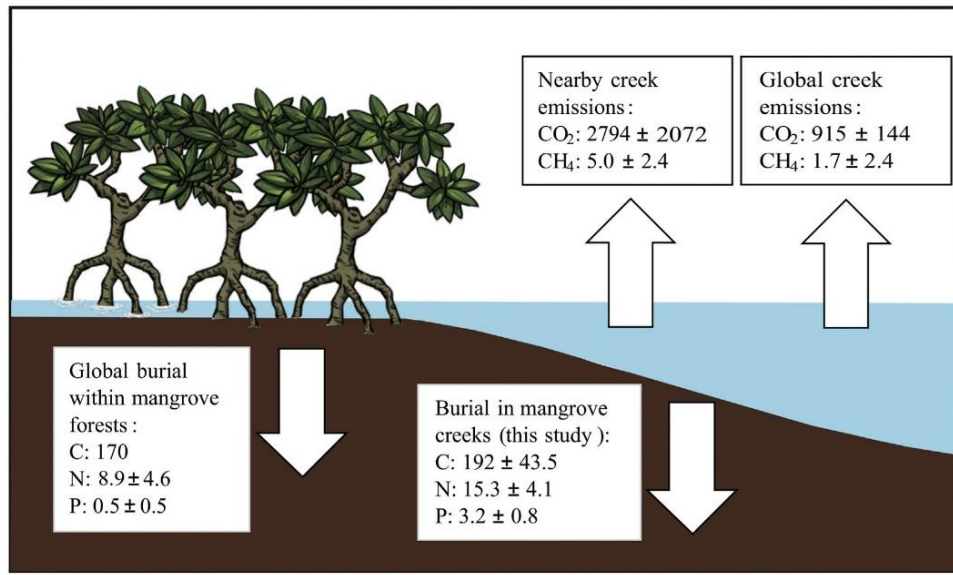


**Fig. 7.** Schematic comparing the global carbon (Pérez et al., 2018) and nitrogen and phosphorus burial rates (Breithaupt et al., 2014) for conserved mangrove forest with Marapanim mangrove creek (this study) and the global mangrove water-atmosphere  $\text{CO}_2$  and  $\text{CH}_4$  flux rates (Rosentreter et al., 2018) with “Furo do Meio” mangrove creek (Call et al., 2019). All rates are in  $\text{g m}^{-2} \text{ yr}^{-1}$ .

environments are unaccounted carbon sinks and are relevant in terms of carbon budgets in mangrove-colonized coastal zones.

#### Declaration of Competing Interest

The authors declare that they have no known competing financial interests or personal relationships that could have appeared to influence the work reported in this paper.

#### Acknowledgements

The authors thank the research grants from the Brazilian Ministry of Education (CAPES) and Brazilian Research Council (CNPq) to C.R.L. Matos and W. Machado. C.J. Sanders is supported by Australian Research Council (DE160100443) and E. Metzger by CNRS-EC2CO project Vublue.

#### Appendix A. Supplementary data

Supplementary data to this article can be found online at <https://doi.org/10.1016/j.margeo.2020.106317>.

#### References

- AgisoftPhotoScan, 2018. AgiSoft PhotoScan Professional. Version 1.4.5. Agisoft LLC, St. Petersburg, Russia Retrieved from. <http://www.agisoft.com/downloads/installer/>.
- Alongi, D.M., 2014. Carbon cycling and storage in mangrove forests. *Annu. Rev. Mar. Sci.* 6, 195–219. <https://doi.org/10.1146/annurev-marine-010213-135020>.
- Alongi, D.M., 2020. Global significance of mangrove blue carbon in climate change mitigation (Version 1). *Sci 2*, 57.
- Alongi, D.M., Boto, K.G., Robertson, A.I., 1992. Nitrogen and phosphorus cycles. In: Robertson, A.I., Alongi, D.M. (Eds.), Tropical Mangrove Ecosystems. Coastal and Estuarine Studies. American Geophysical Union, Washington, DC, pp. 251–292. <https://doi.org/10.1029/ce041p0251>.
- Appleby, P.G., Oldfield, F., 1992. Application of lead-210 to sedimentation studies. In: Ivanovich, M., Harmon, S. (Eds.), Uranium Series Disequilibrium: Application to Earth, Marine and Environmental Science, second ed. Oxford Science Publications, pp. 731–783.
- Arias-Ortiz, A., Masqué, P., García-Orellana, J., Serrano, O., Mazarrasa, I., Marbà, N., Lovelock, C.E., Lavery, P.S., Duarte, C.M., 2018. Reviews and syntheses:  $^{210}\text{Pb}$ -derived sediment and carbon accumulation rates in vegetated coastal ecosystems – setting the record straight. *Biogeosciences* 15, 6791–6818. <https://doi.org/10.5194/bg-15-6791-2018>.
- Aspila, K.L., Agemian, H., Chau, A.S.Y., 1976. A semi-automated method for the determination of inorganic, organic and total phosphate in sediments. *Analyst* 101, 187–197. <https://doi.org/10.1039/AN9760100187>.
- Bernardino, A.F., Sanders, C.J., Bissoli, L.B., de Gomes, L.E., Kauffman, J.B., Ferreira, T.O., 2020. Land use impacts on benthic bioturbation potential and carbon burial in Brazilian mangrove ecosystems. *Limnol. Oceanogr.* 9999, 1–11. <https://doi.org/10.1002/lnco.11458>.
- Berrédo, J.F., Costa, M.L., Progne, M.P.S., 2008. Efeitos das variações sazonais do clima tropical úmido sobre as águas e sedimentos de manguezais do estuário do rio Marapanim, costa nordeste do Estado do Pará. *Acta Amazon.* 38, 473–482. <https://doi.org/10.1590/S0044-59672008000300012>.
- Blott, S.J., Pye, K., 2001. GRADISTAT: a grain size distribution and statistics package for the analysis of unconsolidated sediments. *Earth Surf. Process. Landf.* 26, 1237–1248. <https://doi.org/10.1002/esp.261>.
- Bouillon, S., Connolly, R.M., Lee, S.Y., 2008. Organic matter exchange and cycling in mangrove ecosystems: recent insights from stable isotope studies. *J. Sea Res.* 59, 44–58. <https://doi.org/10.1016/j.seares.2007.05.001>.
- Breitbach, J.L., Smoak, J.M., Smith, T.J., Sanders, C.J., Hoare, A., 2012. Organic carbon burial rates in mangrove sediments: strengthening the global budget. *Glob. Biogeochem. Cycles* 26. <https://doi.org/10.1029/2012gb004375>.
- Breitbach, J.L., Smoak, J.M., Smith, T.J., Sanders, C.J., 2014. Temporal variability of carbon and nutrient burial, sediment accretion, and mass accumulation over the past century in a carbonate platform mangrove forest of the Florida Everglades. *J. Geophys. Res. Biogeosci.* 119, 2032–2048. <https://doi.org/10.1002/2014JG002715>.
- Call, M., Santos, I.R., Dittmar, T., Rezende, C.E., Asp, N.E., Maher, D.T., 2019. High pore-water derived  $\text{CO}_2$  and  $\text{CH}_4$  emissions from a macro-tidal mangrove creek in the Amazon region. *Geochim. Cosmochim. Acta* 247, 106–120. <https://doi.org/10.1016/j.gca.2018.12.029>.
- Canfield, D.E., 1994. Factors influencing organic carbon preservation in marine sediments. *Chem. Geol.* 114, 315–329. [https://doi.org/10.1016/0009-2541\(94\)90061-2](https://doi.org/10.1016/0009-2541(94)90061-2).
- Canfield, D.E., Kristensen, E., Thamdrup, B., 2005. Heterotrophic carbon metabolism. *Aquat. Geomicrobiol. Adv. Mar. Biol.* 48, 129–166. [https://doi.org/10.1016/S0065-2881\(05\)48005-0](https://doi.org/10.1016/S0065-2881(05)48005-0).
- Carvalho, M.C., Eickhoff, W., Drexel, M., 2020. Open-source autosampler for elemental and isotopic analyses of solids. *HardwareX* 8 (e00123), 1–22. <https://doi.org/10.1016/j.hrdwrx.2020.e00123>.
- Chambers, L.G., Davis, S.E., Troxler, T., Boyer, J.N., Downey-Wall, A., Scinto, L.J., 2013. Biogeochemical effects of simulated sea level rise on carbon loss in an Everglades mangrove peat soil. *Hydrobiologia* 726, 195–221. <https://doi.org/10.1007/s10750-013-1764-6>.
- Cohen, M.C.L., de Souza, A.V., Rossetti, D.F., Pessenda, L.C.R., França, M.C., 2018. Decadal-scale dynamics of an Amazonian mangrove caused by climate and sea level changes: inferences from spatial-temporal analysis and Digital Elevation Models. *Earth Surf. Process. Landf.* 43, 2876–2888. <https://doi.org/10.1002/esp.4440>.
- Cohen, M.C.L., Figueiredo, B.L., Oliveira, N.N., Fontes, N.A., França, M.C., Pessenda, L.C.R., Lima, P., 2019. Impacts of Holocene and modern sea-level changes on estuarine mangroves from Northeastern Brazil. *Earth Surf. Process. Landf.* <https://doi.org/10.1002/esp.4737>.
- Currin, C.A., Newell, S.Y., Paerl, H.W., 1995. The Role of Standing Dead Spartina alterniflora and Benthic Microalgae in Salt Marsh Food Webs: Considerations Based on Multiple Stable Isotope Analysis. *Mar. Ecol. Prog. Ser.* 121, 99–116.
- Darrow, E.S., Carmichael, R.H., Calci, K.R., Burkhardt, W., 2017. Land-use related changes to sedimentary organic matter in tidal creeks of the northern Gulf of Mexico. *Limnol. Oceanogr.* 62, 686–705. <https://doi.org/10.1002/lnco.10453>.
- Deines, P., 1980. The isotopic composition of reduced organic carbon. In: Fritz, P., Fontes, J.C. (Eds.), *Handbook of Environmental Isotope Geochemistry*. The Terrestrial Environment, vol. 1. Elsevier, Amsterdam, pp. 329–406. <https://doi.org/10.1016/B978-0-444-41780-0.50015-8>.
- Dittmar, T., Hertkorn, N., Kattner, G., Lara, R.J., 2006. Mangroves, a major source of dissolved matter sources to the oceans. *Glob. Biogeochem. Cycles* 20, GB1012. <https://doi.org/10.1029/2005GB002570>.
- Feng, J., Zhou, J., Wang, L., Cui, X., Ning, C., Wu, H., Zhu, X., Lin, G., 2017. Effects of short-term invasion of Spartina alterniflora and the subsequent restoration of native mangroves on the soil organic carbon, nitrogen and phosphorus stock. *Chemosphere* 184, 774–783. <https://doi.org/10.1016/j.chemosphere.2017.06.060>.
- Feng, J., Wang, S., Wang, S., Ying, R., Yin, F., Jiang, L., Li, Z., 2019. Effects of invasive spartina alterniflora islet, and subsequent ecological replacement by sonneratia apetala Buch.-Ham. on soil organic carbon fractions and stock. *Forests* 10, 171. <https://doi.org/10.3390/f10020171>.
- Fernandes, M.E.B., Oliveira, F.P., Eyzaguirre, I.A.L., 2018. Mangroves on the Brazilian Amazon coast: Uses and rehabilitation. In: Makowski, C., Finkl, C. (Eds.), *Threats to Mangrove Forests*. Coastal Research Library, vol 25 Springer, Cham. [https://doi.org/10.1007/978-3-319-73016-5\\_29](https://doi.org/10.1007/978-3-319-73016-5_29).
- Giri, C., Ochieng, E., Tieszen, L.L., Zhu, Z., Singh, A., Loveland, T., Masek, J., Duke, N., 2011. Status and distribution of mangrove forests of the world using earth observation satellite data. *Glob. Ecol. Biogeogr.* 20, 154–159. <https://doi.org/10.1111/j.1466-8238.2010.00584.x>.
- GlobalMapper, 2017. (Version 19). Blue Marble Geographics. Hallowell, Maine, United States.
- Gontharet, S., Mathieu, O., Lévéque, J., Milloux, M.-J., Lesourd, S., Philippe, S., Caillaud, J., Gardel, A., Sarrazin, M., Proisy, C., 2014. Distribution and sources of bulk organic matter (OM) on a tropical intertidal mud bank in French Guiana from elemental and isotopic proxies. *Chem. Geol.* 376, 1–10. <https://doi.org/10.1016/j.chemgeo.2014.03.009>.
- Gorman, D., Sumida, P.Y.G., Figueira, R.C.L., Turra, A., 2020. Improving soil carbon estimates of mudflats in Araçá Bay using spatial models that consider riverine input, wave exposure and biogeochemistry. *Estuar. Coast. Shelf Sci.* 238, 106734. <https://doi.org/10.1016/j.ecss.2020.106734>.
- Grasshoff, K., Kremling, K., Ehrrhardt, M., 1999. Methods of Seawater Analysis, third ed. Wiley, New York. <https://doi.org/10.1002/9783527613984>.
- Hammer, O., Harper, D.A.T., Ryan, P.D., 2001. PAST: paleontological statistics software package for education and data analysis. *Paleontol. Electron.* 4 (1) (9 pp). [https://palaeo-electronica.org/2001\\_1/past/issue1\\_01.htm](https://palaeo-electronica.org/2001_1/past/issue1_01.htm).
- Hedges, J.I., Keil, R.G., 1995. Sedimentary organic matter preservation: an assessment and speculative synthesis. *Mar. Chem.* 49, 81–115. [https://doi.org/10.1016/0304-4202\(95\)00008-F](https://doi.org/10.1016/0304-4202(95)00008-F).
- Hedges, J.I., Keil, R.G., Benner, R., 1997. What happens to terrestrial organic matter in the ocean? *Org. Geochem.* 27, 195–212. [https://doi.org/10.1016/S0146-6380\(97\)00066-1](https://doi.org/10.1016/S0146-6380(97)00066-1).
- Howard, J., Hoyt, S., Isensee, K., Pidgeon, E., Telzswski, M., 2014. Coastal Blue Carbon: Methods for Assessing Carbon Stocks and Emissions Factors in Mangroves, Tidal Salt Marshes, and Seagrass Meadows. *Conserv. Int. Intergov. Oceanogr. Comm.* UNESCO, Int. Union Conserv. Nature, Arlington, Virginia, USA. pp. 1–180.
- ICMBio, 2018. Atlas dos Manguezais do Brasil, 1st ed. Instituto Chico Mendes de Conservação da Biodiversidade, Brasília. [https://doi.org/10.1016/S0146-6380\(97\)00066-1](https://doi.org/10.1016/S0146-6380(97)00066-1). (176 p).
- Jennerjahn, T.C., 2012. Biogeochemical response of tropical coastal systems to present and past environmental change. *Earth Sci. Rev.* 114, 19–41. <https://doi.org/10.1016/j.earscirev.2012.04.005>.
- Jennerjahn, T.C., Ittekkot, V., 2002. Relevance of mangroves for the production and deposition of organic matter along tropical continental margins. *Naturwissenschaften* 89 (1), 23–30. <https://doi.org/10.1007/s00114-001-0283-x>.
- Kaufman, J.B., Bernardino, A.F., Ferreira, T.O., Giovannoni, L.R., de Gomes, L.E., Romero, D.J., Jimenez, L.C.Z., Ruiz, F., 2018. Carbon stocks of mangroves and salt marshes of the Amazon region, Brazil. *Biol. Lett.* 14, 20180208. <https://doi.org/10.1098/rsbl.2018.0208>.
- Keil, R.G., Montluçon, D.B., Prahl, F.G., Hedges, J.I., 1994. Sorptive preservation of labile organic matter in marine sediments. *Nature* 370, 549–552.
- Kemp, A.C., Vane, C.H., Horton, B.P., Culver, S.J., 2010. Stable carbon isotopes as potential sea-level indicators in salt marshes, North Carolina, USA. *The Holocene* 20 (4), 623–636. <https://doi.org/10.1177/0959636909354302>.

- Kjerfve, B., Lacerda, L.D., 1993. Mangroves of Brazil. In: Conservation and Sustainable Utilization of Mangrove Forests in Latin America and Africa Regions. Part 1: Latin America. ITTO/ISME Project PD114/90(F), pp. 245–272.
- Kristensen, E., Hansen, K., 1995. Decay of plant detritus in organic-poor marine sediment: production rates and stoichiometry of dissolved C and N compounds. *J. Mar. Res.* 53, 675–702. <https://doi.org/10.1357/002240953213115>.
- Kristensen, E., Bouillon, S., Dittmar, T., Marchand, C., 2008. Organic carbon dynamics in mangrove ecosystems: a review. *Aquat. Bot.* 89 (2), 201–219. <https://doi.org/10.1016/j.aquabot.2007.12.005>.
- Kusumaningtyasa, M.A., Huthahean, A.A., Fischer, H.W., Mayod, M.P., Ransbyd, D., Jennerjahn, T.C., 2019. Variability in the organic carbon stocks, sources, and accumulation rates of Indonesian mangrove ecosystems. *Estuar. Coast. Shelf Sci.* 218, 310–323. <https://doi.org/10.1016/j.ecss.2018.12.007>.
- Lamb, A.L., Wilson, G.P., Leng, M.J., 2006. A review of coastal palaeoclimate and relative sea-level reconstructions using  $\delta^{13}\text{C}$  and C/N ratios in organic material. *Earth-Sci. Rev.* 75, 29–57. <https://doi.org/10.1016/j.earscirev.2005.10.003>.
- Liu, D., Li, X., Emeis, K.C., Wang, Y., Richard, P., 2015. Distribution and sources of organic matter in surface sediments of Bohai Sea near the Yellow River Estuary, China. *Estuar. Coast. Shelf Sci.* 165, 128–136. <https://doi.org/10.1016/j.ecss.2015.09.007>.
- Loring, D.H., Rantala, R.T.T., 1992. Manual for the geochemical analyses of marine sediments and suspended particulate matter. *Earth-Sci. Rev.* 32, 235–283. [https://doi.org/10.1016/0012-8252\(92\)90001-A](https://doi.org/10.1016/0012-8252(92)90001-A).
- Marchio, D., Savarese, M., Bovard, B., Mitsch, W., 2016. Carbon sequestration and sedimentation in mangrove swamps influenced by hydrogeomorphic conditions and urbanization in Southwest Florida. *Forests* 7 (12), 116. <https://doi.org/10.3390/f7060116>.
- Martorano, L.G., Pereira, L.C., Cesar, E.G.M., Pereira, I.C.B., 1993. Estudos Climáticos do Estado do Pará, Classificação Climática (Köppen) e Deficiência Hídrica (Thornthwhite, Mather). Belém, SUDEM/EMBRAPA, SNILCS, pp. 53.
- Mayer, L.M., 1994. Surface area control of organic carbon accumulation in continental shelf sediments. *Geochim. Cosmochim. Acta* 58, 1271–1284. [https://doi.org/10.1016/0016-7037\(94\)90381-6](https://doi.org/10.1016/0016-7037(94)90381-6).
- McGlathery, K.J., Sundback, K., Anderson, I.C., 2007. Eutrophication in shallow coastal bays and lagoons: the role of plants in the coastal filter. *Mar. Ecol. Prog. Ser.* 348, 1–18. <https://doi.org/10.3354/meps07132>.
- McLeod, E., Chmura, G.L., Bouillon, S., Salm, R., Björk, M., Duarte, C.M., Lovelock, C.E., Schlesinger, W.H., Silliman, B.R., 2011. A blueprint for blue carbon: toward an improved understanding of the role of vegetated coastal habitats in sequestering CO<sub>2</sub>. *Front. Ecol. Environ.* 9, 552–560. <https://doi.org/10.1890/110004>.
- Meyers, P.A., 1994. Preservation of elemental and isotopic source identification of sedimentary organic matter. *Chem. Geol.* 114, 289–302. [https://doi.org/10.1016/0009-2541\(94\)90059-0](https://doi.org/10.1016/0009-2541(94)90059-0).
- Meyers, P.A., 1997. Organic geochemical proxies of paleoceanographic, paleolimnologic, and paleoclimatic processes. *Org. Geochem.* 27, 213–250. [https://doi.org/10.1016/S0146-6380\(97\)00049-1](https://doi.org/10.1016/S0146-6380(97)00049-1).
- Meyers, P.A., 2003. Applications of organic geochemistry to paleolimnological reconstructions: a summary of examples from the Laurentian Great Lakes. *Org. Geochem.* 34, 261–289. [https://doi.org/10.1016/S0146-6380\(02\)00168-7](https://doi.org/10.1016/S0146-6380(02)00168-7).
- Nascimento, W.R., Souza-Filho, P.W.M., Proisy, C., Lucas, R.M., Rosenqvist, A., 2013. Mapping changes in the largest continuous Amazonian mangrove belt using object-based classification of multisensor satellite imagery. *Estuar. Coast. Shelf Sci.* 117, 83–93. <https://doi.org/10.1016/j.ecss.2012.10.005>.
- Nellenmann, C., Corcoran, E., Duarte, C.M., Valdres, L., Young, C.D., Fonseca, L., Grimsditch, G., 2009. Blue Carbon - The Role of Healthy Oceans in Binding Carbon. UN Environment, GRID-Arendal (ISBN: 978-82-7701-060-1).
- Paiva, R.S., Eskinazi-Leça, E., Passavante, J.Z.O., Silva-Cunha, M.G.G., Melo, N.F.A.C., 2006. Ecological considerations on phytoplankton from the Guajará bay and from the Guamá river estuary in Para, Brazil. *Bol. Mus. Para. Emílio Goeldi Ciências Naturais* 1, 133–146.
- Pérez, A., Machado, W., Gutierrez, D., Stokes, D., Sanders, L., Smoak, J.M., Santos, I., Sanders, C.J., 2017. Changes in organic carbon accumulation driven by mangrove expansion and deforestation in a New Zealand estuary. *Estuar. Coast. Shelf Sci.* 192, 108–116. <https://doi.org/10.1016/j.ecss.2017.05.009>.
- Pérez, A., Libardoni, B.G., Sanders, C.J., 2018. Factors influencing organic carbon accumulation in mangrove ecosystems. *Biol. Lett.* 14 (10). <https://doi.org/10.1098/rsbl.2018.0237>.
- Peterson, B.J., Howarth, R.W., 1987. Sulfur, carbon, and nitrogen isotopes used to trace organic matter flow in the salt-marsh estuaries of Sapelo Island, Georgia. *Limnol. Oceanogr.* 32 (6), 1195–1213. <https://doi.org/10.4319/lo.1987.32.6.1195>.
- Prahl, F.G., De Lange, G.T., Scholten, S., Cowie, G.L., 1997. A case of post-depositional aerobic degradation of terrestrial organic matter in turbidite deposits from the Madeira Abyssal Plain. *Org. Geochem.* 27, 141–152. [https://doi.org/10.1016/S0146-6380\(97\)00078-8](https://doi.org/10.1016/S0146-6380(97)00078-8).
- Prasad, M.B.K., Ramanathan, A.L., 2009. Organic matter characterization in a tropical estuarine-mangrove ecosystem of India: preliminary assessment by using stable isotopes and lignin phenols. *Estuar. Coast. Shelf Sci.* 84 (4), 617–624. <https://doi.org/10.1016/j.ecss.2009.07.029>.
- Prasad, M.B.K., Kumar, A., Ramanathan, A.L., Datta, D.K., 2017. Sources and dynamics of sedimentary organic matter in Sundarban mangrove estuary from Indo-Gangetic delta. *Ecol. Process.* 6, 8. <https://doi.org/10.1186/s13717-017-0076-6>.
- Ranjan, R.K., Routh, J., Ramanathan, A.I., Klump, J.V., 2011. Elemental and stable isotope records of organic matter input and its fate in the Pichavaram mangrove-estuarine sediments (Tamil Nadu, India). *Mar. Chem.* 126, 163–172. <https://doi.org/10.1016/j.marchem.2011.05.005>.
- Ray, R., Majumder, N., Das, S., Chowdhury, C., Jana, T.K., 2014. Biogeochemical cycle of nitrogen in a tropical mangrove ecosystem, east coast of India. *Mar. Chem.* 167, 33–43. <https://doi.org/10.1016/j.marchem.2014.04.007>.
- Ray, R., Majumder, N., Chowdhury, C., Das, S., Jana, T.K., 2017. Phosphorus budget of the sundarbans mangrove ecosystem: box model approach. *Estuar. Coasts* 41, 1036–1049. <https://doi.org/10.1007/s12237-017-0332-0>.
- Redfield, A.C., Ketchum, B.H., Richards, F.A., 1963. The influence of organisms on the composition of sea-water. In: Hill, M.N. (Ed.), *The Composition of Seawater: Comparative and Descriptive Oceanography*. The Sea: Ideas and Observations on Progress in the Study of the Seas. 2. pp. 26–77.
- Rosenstretter, J.A., Maher, D.T., Erler, D.V., Murray, R., Eyre, B.D., 2018. Seasonal and temporal CO<sub>2</sub> dynamics in three tropical mangrove creeks – a revision of global mangrove CO<sub>2</sub> emissions. *Geochim. Cosmochim. Acta* 222, 729–745. <https://doi.org/10.1016/j.gca.2017.11.026>.
- Routh, J., Meyers, P.A., Choudhury, P., Kumar, B., 2009. A sediment record of recent nutrient loading and trophic state change in Lake Norrviken, Sweden. *J. Paleolimnol.* 42, 325–341. <https://doi.org/10.1007/s10933-008-9279-2>.
- Saderne, V., Cusack, O., Almahaeser, H., Krishnakumar, P.K., Rabaoui, L., Qurban, M.A., Duarte, C.M., 2020. Role of vegetated coastal ecosystems as nitrogen and phosphorous filters and sinks in the coasts of Saudi Arabia. *Environ. Res. Lett.* 15, 034058. <https://doi.org/10.1088/1748-9326/ab76da>.
- Saintilan, N., Rogers, K., Mazumder, D., Woodroffe, C., 2013. Allochthonous and autochthonous contributions to carbon accumulation and carbon store in southeastern Australian coastal wetlands. *Estuar. Coast. Shelf Sci.* 128, 84–92. <https://doi.org/10.1016/j.ecss.2013.05.010>.
- Sanders, C.J., Santos, I.R., Maher, D.T., Breithaupt, J.L., Smoak, J.M., Ketterer, M., Call, M., Sanders, L.M., Eyre, B.D., 2016. Examining  $^{239+240}\text{Pu}$ ,  $^{210}\text{Pb}$  and historical events to determine carbon, nitrogen and phosphorus accumulation in mangrove sediments of Moreton Bay, Australia. *J. Environ. Radioact.* 151, 623–629. <https://doi.org/10.1016/j.jenvrad.2015.04.018>.
- Santos, I.R., Maher, D.T., Larkin, R., Webb, J.R., Sanders, C.J., 2019. Carbon outwelling and outgassing vs. burial in an estuarine tidal creek surrounded by mangrove and saltmarsh wetlands. *Limnol. Oceanogr.* 64, 996–1013. <https://doi.org/10.1002/limo.11090>.
- Sasmilo, S.D., Kuzyakov, Y., Lubis, A.A., Murdiyarso, D., Hutley, L.B., Bachri, S., Friess, D.A., Martius, C., Borchard, N., 2020. Organic carbon burial and sources in soils of coastal mudflat and mangrove ecosystems. *Catena* 187, 104414. <https://doi.org/10.1016/j.catena.2019.104414>.
- Schultz, D.J., Calder, J.A., 1976. Organic carbon,  $^{13}\text{C}/^{12}\text{C}$  variations in estuarine sediments. *Geochim. Cosmochim. Acta* 40, 381–385. [https://doi.org/10.1016/0016-7037\(76\)90002-8](https://doi.org/10.1016/0016-7037(76)90002-8).
- Seeberg-Elverfeldt, J., Schlüter, M., Feseker, T., Kölling, M., 2005. Rhizone sampling of pore waters near the sediment-water interface of aquatic systems. *Limnol. Oceanogr. Methods* 3, 361–371. <https://doi.org/10.4319/lom.2005.3.361>.
- Silva, C.A., Souza-Filho, P.W.M., Rodrigues, S.P.W., 2009. Morphology and modern sedimentary deposits of the macrotidal Marapanaí Estuary (Amazon, Brazil). *Cont. Shelf Res.* 29, 619–631. <https://doi.org/10.1016/j.csr.2008.09.018>.
- Smoak, J.M., Breithaupt, J.L., Smith, T.J., Sanders, C.J., 2013. Sediment accretion and organic carbon burial relative to sea-level rise and storm events in two mangrove forests in Everglades National Park. *Catena* 104, 58–66.
- Steinmuller, H.E., Foster, T.E., Boudreau, P., Ross Hinkle, C., Chambers, L.G., 2020. Tipping points in the mangrove Marsh: characterization of biogeochemical cycling along the mangrove-salt marsh ecotone. *Ecosystems* 23, 417–434. <https://doi.org/10.1007/s10021-019-00411-8>.
- Udden, J.A., 1914. Mechanical composition of clastic sediments. *Bull. Geol. Soc. Am.* 25, 655–744.
- Vilhena, M.P.S.P., Costa, M.L., Berrédo, J.F., 2013. Accumulation and transfer of Hg, As, Se, and other metals in the sediment-vegetation-crab-human food chain in the coastal zone of the northern Brazilian state of Para (Amazonia). *Environ. Geochem. Health* 35, 477–494. <https://doi.org/10.1007/s10653-013-9509-z>.
- Vilhena, M.P.S.P., Costa, M.L., Berrédo, J.F., Paiva, R.S., Moreira, M.Z., 2018. The sources and accumulation of sedimentary organic matter in two estuaries in the Brazilian Northern coast. *Reg. Stud. Mar. Sci.* 18, 188–196. <https://doi.org/10.1016/j.rsma.2017.10.007>.
- Wang, F., Lu, X., Sanders, C.J., Tang, J., 2019. Tidal wetland resilience to sea level rise increases their carbon sequestration capacity in United States. *Nat. Commun.* 10 (5434), 1–11. <https://doi.org/10.1038/s41467-019-13294-z>.
- Watanabe, K., Kuwae, T., 2015. How organic carbon derived from multiple sources contributes to carbon sequestration processes in a shallow coastal system? *Glob. Chang. Biol.* 21, 2612–2623. <https://doi.org/10.1111/gcb.12924>.
- Wentworth, C.K., 1922. A scale of grade and class terms for clastic sediments. *J. Geol.* 30, 377–392.
- Zonneveld, K.A.F., Versteegh, G.J.M., Kasten, S., Eglington, T.I., Emeis, K.-C., Huguet, C., Koch, B.P., de Lange, G.J., de Leeuw, J.W., Middelburg, J.J., Mollenhauer, G., Prahl, F., Rethemeyer, J., Wakeham, S., 2010. Selective preservation of organic matter in marine environments: processes and impact on the fossil record. *Biogeosciences* 7, 483–511. <https://doi.org/10.5194/bg-7-483-2010>.

## 6.2 ARTIGO 2: CONTRASTING SEASONAL RECYCLING OF METALS AND NUTRIENTS IN PORE WATER OF MANGROVE CREEKS, AMAZON REGION

Christiene R. L. Matos<sup>a,\*</sup>, José F. Berredo<sup>b,\*</sup>, Wilson Machado<sup>c</sup>, Edouard Metzger<sup>d</sup>, Christian J. Sanders<sup>e</sup>, Kelson C. F. Faial<sup>f</sup>, Marcelo C. L. Cohen<sup>a</sup>

<sup>a</sup>Programa de Pós-Graduação em Geologia e Geoquímica, Universidade Federal do Pará, Belém, Pará, Brazil.

<sup>b</sup>Museu Paraense Emílio Goeldi/MCTIC. Belém, Pará, Brazil.

<sup>c</sup>Programa de Pós-Graduação em Geoquímica, Universidade Federal Fluminense, Niterói, Rio de Janeiro, Brazil.

<sup>d</sup>Laboratoire des Bio-Indicateurs Actuels et Fossiles, UMR6112 CNRS LPG-BIAF, Université d'Angers, Angers, France.

<sup>e</sup>National Marine Science Centre, Southern Cross University, Coffs Harbour, New South Wales, Australia.

<sup>f</sup>Laboratório de Toxicologia, Seção de Meio Ambiente, Instituto Evandro Chagas, Belém, Pará, Brazil.

\*Corresponding authors at: Museu Paraense Emílio Goeldi, Av. Perimetral, 1901 – CEP. 66077-830, Belém – Pará, Brazil.

E-mail addresses: christienematos@hotmail.com (C.R.L. Matos), berredo@museu-goeldi.br (J.F. Berredo), wmachado@geoq.uff.br (W. Machado), edouard.metzger@univ-angers.fr (E. Metzger), christian.sanders@scu.edu.au (C.J. Sanders), kelsonfaial@iec.gov.br (K.C.F. Faial), mcohen80@hotmail.com (M.C.L. Cohen).

### ABSTRACT

This study examines the influence of the Amazonian seasonal rainfall patterns on the physico-chemical conditions, diagenetic processes and exchange of nutrients and metals along the sediment-water interface (SWI) in intertidal mudflats fringed by pristine mangroves. During the wet season, the salinity values decreased due to increased rainfall, with a dilution-mixing zone in the top sediment intervals (<15 cm). In the dilution-mixing zone, Fe (III) and Mn (IV) reduction are dominant anaerobic respiratory processes. The redox zonation of sediments oscillated in response to the rainfall patterns, with the highest concentrations of Fe<sup>2+</sup> and Mn<sup>2+</sup> in deeper sediment layers during the dry season. Under suboxic conditions, the mudflat sediments act as

a source of  $\text{Fe}^{2+}$ ,  $\text{Mn}^{2+}$ ,  $\text{NH}_4^+$ , and  $\text{PO}_4^{3-}$  to the water column, and these fluxes were driven by rainfall. The results indicated that mangrove-fringed mudflats are quite effective in retaining nutrients and iron in sediment solid phases than exporting to the coastal waters, while can potentially be a significant contributor to the oceanic Mn cycle. In addition, temporal variability in pyrite formation revealed that the solid phase retention mechanisms are also susceptible to seasonal effects, with lower concentrations of chromium-reducible sulfur (CRS, mainly pyrite fraction) during the dry season. Therefore, we show that these seasonal variabilities implied substantial changes of physicochemical properties and the diagenetic processes, affecting the release of metals and nutrients from the SWI, evidencing the role of mangrove-fringed creeks as biogeochemical reactors, rather than simple conduits of dissolved metals and nutrients between mangrove wetlands and the coastal ocean.

**Keywords:** Early diagenesis. Seasonal rainfall. Iron reduction. Sulfate reduction. Macrotidal estuary. Tidal creek.

## 1 Introduction

Mangroves are coastal vegetated ecosystems that are situated along the land-ocean interface, under the influence of fresh and seawater. Mangroves, whether pristine or disturbed, can act as a carbon sink storing significant amount of carbon (Alongi 2020), nutrient (Breithaupt et al. 2014; Sanders et al. 2014) and metals (Marchand et al. 2011; Thanh-Nho et al. 2019) in their sediments. High organic matter (OM) accumulation in mangrove sediments enhances intense microbial activity, often leading to oxygen depletion within the upper few millimeters of sediment (Kristensen et al. 1994; Glud 2008; Meiggs and Taillefert 2011). This process favors the prevalence of anaerobic pathways of OM mineralization (Alongi 1995; Kristensen et al. 2011). Under anaerobic conditions, the microbial sulfate reduction (SR) and iron reduction (IR) are considered as major pathways of organic carbon mineralization during the early diagenesis (Ku et al. 2008; Kristensen et al. 2011; Pan et al. 2019).

The anaerobic degradation of sedimented OM and remineralization in the sediment releases inorganic nutrients ( $\text{NH}_4^+$  and  $\text{PO}_4^{3-}$ ) and metals ( $\text{Fe}^{2+}$  and  $\text{Mn}^{2+}$ ) into the pore water, and the transport mechanisms (e.g., diffusion, advection and bioturbation) can induce its transfer to the overlying water and return to the euphotic zone, which it is very important for the production of phytoplankton in many estuaries (Paul et al. 2008; Holloway et al. 2016). Therefore, mangrove sediments can also act as biogeochemical reactor that recycle nutrients and metals. Pre-

vious studies have reported that pore water exchange with tidal creeks draining mangrove wetlands can be a major driver of trace metal (Sanders et al. 2015; Holloway et al. 2016), carbon (Taillardat et al. 2018; Webb et al. 2019) and nutrient (Tait et al. 2017; Taillardat et al. 2019a), in mangrove to coastal waters. This exchange of dissolved elements can occur essentially through diffusive fluxes across the sediment-water interface (SWI) during inundation, or pore water seepage into the tidal creeks water columns during low and ebbing tides (Ovalle et al. 1990; Bouillon et al. 2007).

Mangroves developed under the Amazon climate regime are subject to high annual precipitation, high temperatures, and semidiurnal macrotides. High rainfall leads to high seasonal freshwater inputs and high fluvial water discharge, causing extreme fluctuations in salinities within estuaries and tidal creeks. Therefore, these waters biogeochemistry changes in temporal (seasonal, tidal, diel) and spatial scales due to the seasonal differences of fluvial discharges and OM inputs from different sources (mainly mangrove and phytoplankton). Previous studies have reported that the documented seasonal rainfall patterns can lead to a seasonal changes in the sedimentary physical and chemical properties (Alongi et al. 2004; Marchand et al. 2004; Berrêdo et al. 2016), pore water chemistry (Lee et al. 2008; Wu et al. 2015; Taillardat et al. 2019) and nutrient and metals release (Alongi et al. 2001; Adame et al. 2010; Yasui et al. 2016; Rao et al. 2018).

The Marapanim River estuary (MRE) represents part of the Amazon estuarine system, northern Brazil, situated approximately 200 km westward from Amazon River. Recently, Matos et al. (2020) results evidenced the role carbon and nutrient sequestration in the intertidal mudflat sediments fringed by pristine mangrove in this region. Thus, this study aims to understand the major sedimentary OM decomposition pathways and the mudflats potential to export metals and nutrients at the SWI. In addition, we investigate the effects of rainfall on the physicochemical properties, pore water biogeochemistry and pyrite formation, to discuss how seasonal diagenetic processes affect metals and nutrient fluxes at the SWI under the Amazon climatic regime.

## 2 Materials and methods

### 2.1 Study area

The MRE, northern Brazil ( $00^{\circ}30'$  to  $01^{\circ}00'S$  and  $47^{\circ}32'$  to  $47^{\circ}00'W$ , Fig. 1), can be subdivided into three morphologic realms: the coastal plain, estuarine plain, and alluvial plain (Silva et al. 2009). The sedimentary deposits of the Coastal Plateau are represented by cliffs and lateritic soils (Pleistocene), derived from the Barreiras Formation (Tertiary), the main source of sand, silt and clay fractions, consisting of quartz, clay minerals (kaolinite and illite), iron oxides, and recent sediments (Holocene) that constitute the mangrove substrates (Berrêdo et al. 2008b). The estuarine plain presents sandy and muddy deposits where mangroves are established (Silva et al. 2009).

The tidal flats of the MRE are occupied by well-developed mangroves, which are part of the largest continuous and best-preserved mangrove forest in the world (Nascimento et al. 2013; Kauffman et al. 2018). The main river channel presents a length and width of ~70 and ~8 km at the mouth, respectively, with incursion of oceanic waves from Atlantic and semidiurnal macrotides that have a tidal range of 3.5 m during neap tide and over 6 m during spring tides (Silva et al. 2009). Saline waters penetrate approximately 62 km up the estuary during the dry season and 42 km during the wet season (Berrêdo et al. 2008b).

The coastal region of Para is characterized by a tropical climate with two distinct seasons. The wet and dry season occurs between January and June, and July and December, respectively. The annual mean precipitation is ~ 2,500 mm, with the majority of precipitation occurring during the wet season. The annual mean temperature is  $27.7^{\circ}C$ . The estuary water temperature oscillates between  $27$  and  $30^{\circ}C$ . Along the estuarine channel the pH values are between alkaline (7.9 to 8.0) and slightly acidic (5.7 to 6.7) conditions during the dry and wet seasons, respectively (Berrêdo et al. 2008b).

Sampling was carried out along three intertidal mudflats. The locations are numbered according to their distance from the Marapanim main River, with number 1 at the Marapanim River margin, and number 2 and 3 in two tidal mangrove creeks along the Marapanim mangrove forest. The distance between sites P1 and P2 is 2.3 km, while site P3 is located ~1 km from site P2. The tidal creeks do not receive any direct freshwater inputs except for rainwater. Sedimentary composition and OM sources at each sampling site were previously characterized by Matos et al. (2020). The estuarine mudflat (P1) has very different sedimentary characteristics in relation to the creek mudflats (P2 and P3). Located in the lowest topographically, P1 presents a

slightly higher sedimentation rate ( $1.8 \text{ cm yr}^{-1}$ ). However, its grain size is represented by a higher sand content (~ 52%), and large contributions from marine OM (wet: 76.4% and dry: 79.6%), which consequently equates to a lower TOC (0.5 - 1.9%), TN (0.04 - 0.17%) and TP (0.009 - 0.044%) contents. Both the P2 and P3 sites are located in topographically highest tidal flats (~ 2 m amsl), where the sediments are strongly oxidized during the dry season. The site P2 is located in more confined area, presented a lower sedimentation rate of  $1.3 \text{ cm yr}^{-1}$ , finer grain size of ~ 68% (silte+clay), marine OM contribution of 54.5% in the wet season and of 69% in the dry season and high TOC (2.3 to 3.8%), TN (0.20 to 0.27%) and TP (0.028 to 0.052%) contents. The site P3, located closer to the mainland, presented sedimentation rate of  $1.5 \text{ cm yr}^{-1}$ , finer particle size of ~ 66%, marine OM contribution of 60% in the wet season and 78% in the dry season, and relatively high TOC (2.2 to 3.0%), TN (0.20 to 0.27%) and TP (0.033 to 0.059 %) contents.

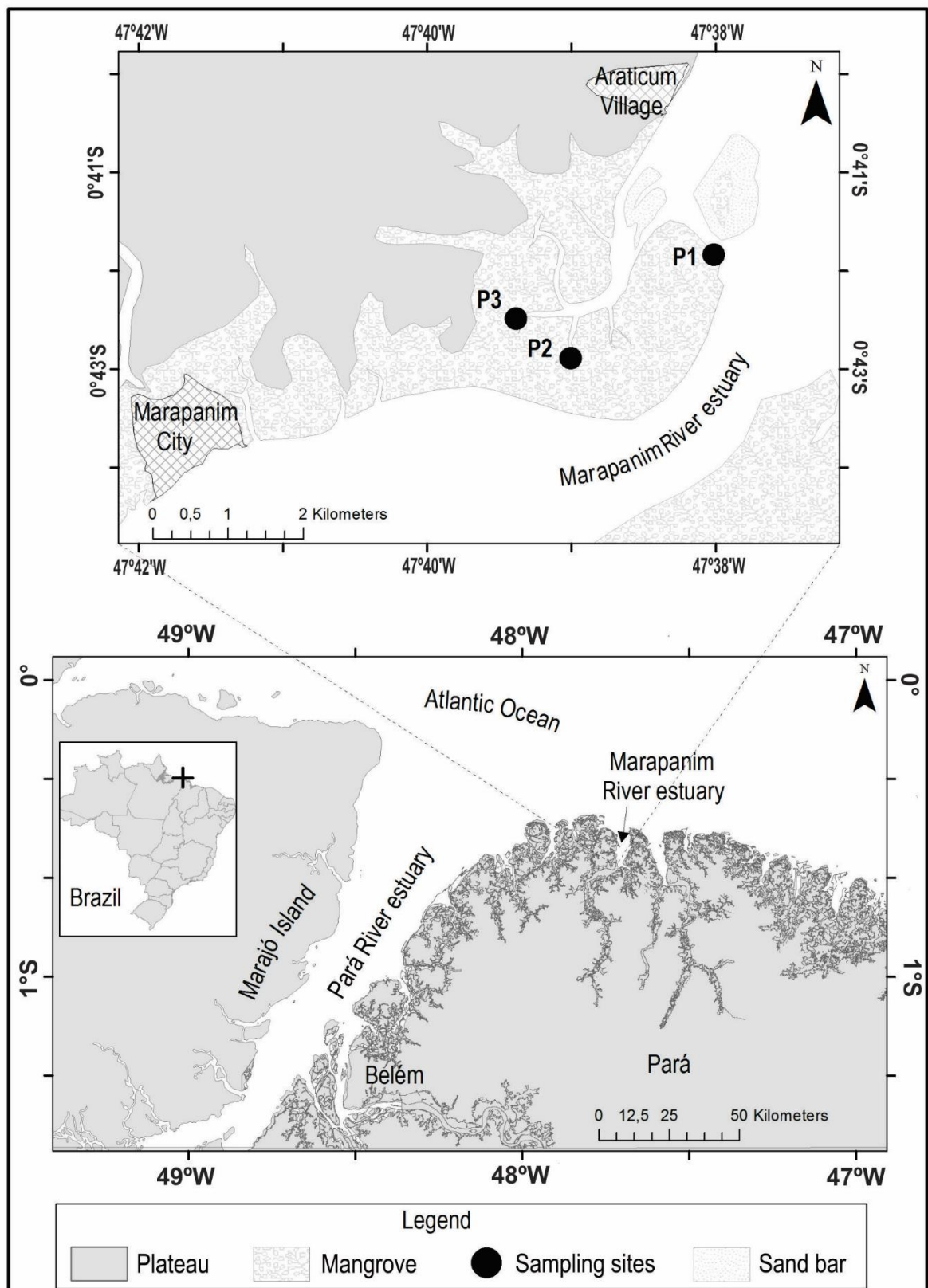


**Fig. 13** Map of the study area in Marapanim estuary showing the P1, P2 and P3 sampling sites

## 2.2 Solid-phase sediment sampling and analyses

To assess the effects of contrasting seasons, two replicate cores were collected from the intertidal mudflat at each site, during the wet (May 2017) and dry (Sept 2017) seasons. A sediment core with approximately 35 cm depth of sediment was recovered, at a water column depth of ~0.8 m. One core, dedicated to solid-phase analyses, was sliced at 1-cm (0 – 6 cm), 2-cm (6 – 20 cm), and 5-cm intervals (20 – 35 cm depth). The sub-samples were stored in polyethylene bags at 4 °C until processing. An aliquot of humid sediment was fixed with Zn-acetate, within a N<sub>2</sub>-filled glove bag, for the determinations of acid volatile sulfides (AVS, mainly Fe monosulfide) and chromium reducible sulfur (CRS, mainly pyrite). The most reactive fraction of the Fe (Fe<sub>R</sub>) and Mn (Mn<sub>R</sub>), and total sulfur (TS) were performed in dried sediment. Depth profiles of total organic carbon (TOC) were obtained from Matos et al. (2020).

Fe<sub>R</sub> and Mn<sub>R</sub> were determined using ascorbate reagent (50 g NaHCO<sub>3</sub>, 50 g Na-citrate, 20 g ascorbic acid for 1 L solution, buffered at pH 8) (Kostka and Luther 1994; Anschutz et al. 2005) . Extractions were carried out on 500 mg of dried sediment in 10 mL of N<sub>2</sub>-degassed ascorbate reagent for 24 h under continuous shaking. The supernatant was diluted 10-fold with HNO<sub>3</sub> (1.0 %). The Fe and Mn concentrations were measured by atomic absorption spectrometry with external standard prepared in the same matrix. TS was determined on a CHNS elemental analyser (PerkinElmer). AVS and CRS were determined in 1 g of sediment by a two-step distillation with cold 6 N HCl followed by boiling 2 N acidic CrCl<sub>2</sub> solution (Fossing and Jørgensen 1989). The liberated H<sub>2</sub>S was collected in Zn-acetate (20%) traps, and its concentration was determined according to the method of Cline (1969). Scanning electron microscopy (SEM) coupled with an energy dispersive X-ray spectrometer was used on particles collected from sediments.

## 2.3 Pore water sampling and analyses

In the second replicate core, the pH and redox potential were measured with a pH meter electrode (Metrohm 826 pH mobile) directly from the sediment through holes in one specific predrilled tube, in the same intervals as the solid-phase; these holes were covered with tape during sampling. After measuring redox-pH, following the same intervals, the overlying and pore waters were removed using Rhyzon® collectors (7 cm and 0.1 µm of length and pore diameter, respectively), inserted directly into the sediment through pre-drilled holes along the

acrylic tubes (Seeberg-Elverfeldt et al. 2005). The overlying water sampling was ~5 cm above the sediment - water interface.

The pore water samples were treated in a N<sub>2</sub>-filled glove bag to prevent oxidation. The overlying and pore water samples were analysed for Cl<sup>-</sup>, SO<sub>4</sub><sup>2-</sup>, Fe<sup>2+</sup>, Mn<sup>2+</sup>, total alkalinity (TA), NH<sub>4</sub><sup>+</sup> and PO<sub>4</sub><sup>3-</sup> and total dissolved sulfide ( $\Sigma\text{H}_2\text{S} = \text{H}_2\text{S} + \text{HS}^- + \text{S}_0 + \text{S}_x^{2-}$ ). A total of 2 mL of water samples were deposited in amber vials for alkalinity analyses. Subsamples of 1 mL were preserved in Eppendorf tubes with 100 µL of a 5% Zn-acetate solution and with 10 µL HCl for  $\Sigma\text{H}_2\text{S}$  and PO<sub>4</sub><sup>3-</sup> analysis, respectively. Samples with 1 mL were preserved in Eppendorf tubes to SO<sub>4</sub><sup>2-</sup> and Cl<sup>-</sup> analyses. All samples were kept at 4 °C. Sub-samples with 1 mL were kept frozen in amber vials to NH<sub>4</sub><sup>+</sup> analyses.

Fe and Mn dissolved concentrations were measured in an ICP-OES (VISTA-MPX CCD Simultaneous) using 10-fold dilutions. The accuracies were checked using a natural water reference NIST (1640a, 1643e). The accuracies of the measurements were within 5% for Fe and Mn. TA was measured by potentiometric Gran titration with 0.01 mol L<sup>-1</sup> HCl immediately after removal of vials from the glove-bag. Standard colorimetric methods were used to measure the NH<sub>4</sub><sup>+</sup> and PO<sub>4</sub><sup>3-</sup> concentrations (Gieskes et al. 1991).  $\Sigma\text{H}_2\text{S}$  contents were quantified by using the colorimetric method from Cline (1969). Concentrations of SO<sub>4</sub><sup>2-</sup> and Cl<sup>-</sup> were measured by ion chromatography (Dionex DX 120) in a 500-fold dilution. Salinity was measured with a portable refractometer (Atago).

#### 2.4 Calculation of sulfate depletion

Chloride is a conservative element, since it is not affected by biological or chemical processes, then, it was used to evaluate the sulfate depletion under the effects of freshwater dilution and microbial removal. Sulfate concentrations were normalized for changes in chloride concentrations according to:

$$(\text{SO}_4^{2-})_{\text{Dep}} = [(\text{Cl}^-)_{\text{pw}} \cdot (R_{\text{sw}})^{-1}] - (\text{SO}_4^{2-})_{\text{pw}} \quad (1)$$

where  $(\text{SO}_4^{2-})_{\text{Dep}}$  is the SO<sub>4</sub><sup>2-</sup> depletion,  $(\text{Cl}^-)_{\text{PW}}$  and  $(\text{SO}_4^{2-})_{\text{PW}}$  are the pore water concentrations of Cl<sup>-</sup> and SO<sub>4</sub><sup>2-</sup>, and R<sub>sw</sub> is the molar ratio of Cl<sup>-</sup> to SO<sub>4</sub><sup>2-</sup> in surface seawater (R<sub>sw</sub> = 19.33; Weston et al. 2006). Sulfate depletion reveals the net microbially mediated consumption of SO<sub>4</sub><sup>2-</sup> (Weston et al. 2006).

## 2.5 Estimates of nutrient fluxes

The diffusive flux estimates of nutrients between sediments and the overlying water were calculated from the interfacial concentration gradients, according to Fick's first law of diffusion (Berner 1980) below:

$$F = -\emptyset D_s (\Delta C / \Delta Z) \quad (2)$$

where  $F$  ( $\text{mmol.m}^{-2}.\text{d}^{-1}$ ) is the diffusive flux,  $\emptyset$  (dimensionless) is the porosity at the sediment surface (depth = 0-1 cm),  $D_s$  ( $\text{m}^2.\text{s}^{-1}$ ) is the molecular diffusion coefficient in sediment, and  $\Delta C / \Delta Z$  is the concentration gradient across the SWI. According to these calculations, negative fluxes reflect sediment uptake processes (i.e. downward flux), whereas positive fluxes indicate benthic recycling (i.e. outward fluxes to the overlying waters). The porosity was expressed and calculated as the volume fraction of the water in the wet sediment. The water volume was identified by the weights difference of wet sediment samples before and after drying at 60 °C.  $\Delta C / \Delta Z$  is the concentration gradient in the overlying water and pore water. The diffusion coefficient ( $D_s$ ) was calculated from the coefficient of molecular diffusion in free water  $D_0$  corrected for sediment porosity and temperature (Li and Gregory 1974). The upper sediment layers presented porosity between 0.51 and 0.76, while the overlying waters revealed temperatures between 28.0 and 29.3 °C.

## 2.6 Statistical analysis

Statistical analyses were executed using statistical package PAST version 3.26 (Hammer et al. 2001). The significant difference in concentrations of dissolved and solid-phase between the sampling sites (P1, P2, and P3) and seasons (wet and dry) were assessed by variance analysis (ANOVA). The normality of data distribution was verified via Shapiro-Wilk before statistical analysis. In the case of variables not normally distributed, they were log-transformed to fit a normal distribution. In all tests, a statistical significance at  $\alpha < 0.05$  was used. Pearson's correlation coefficient was used to measure the relation between each pair of variables, where correlation coefficients higher than 0.5 were interpreted as significant.

### 3 Results

#### 3.1 Sediment geochemistry

Sediment-depth profiles of TOC, TS, CRS, Fe<sub>R</sub> and Mn<sub>R</sub> in different seasons are shown in Fig. 2. The sediment concentrations changed between sites, seasons, and depth. Overall, the range of TOC, TS, CRS, Fe<sub>R</sub> and Mn<sub>R</sub> was lower at sites P1 compared to the sites P2 and P3. In all three sites, TOC concentration decreased slightly with depth, varying from 0.53 to 3.84%. The TS content showed large fluctuations between the sites and seasons varying from 0.04 to 1.62%, with the highest concentrations during the wet season. CRS concentrations ranged from 0.06 to 1.52%, and displayed almost the same distribution patterns with the depth as the TS. Concentrations of AVS were below the detection limit in all sediment profiles. The Fe<sub>R</sub> concentrations decreased slightly with depth, except to P2 in the dry season, varying from 0.11 to 1.07 %. Mn<sub>R</sub> concentrations ranged from 0.004 to 0.061 %, and displayed almost the same distribution patterns with the depth as the Fe<sub>R</sub>. Micro-analysis with SEM-EDS revealed that authigenic pyrite, sometimes surrounded by a clay film, was present with a uniform distribution at all depths and in all the sediment cores. Sulfate minerals (e.g., gypsum) were not present. The sedimentary pyrite occurs as single framboids and as euhedral crystal (Fig. 3). The typical framboids sizes ranged from ~5 µm to ~20 µm.

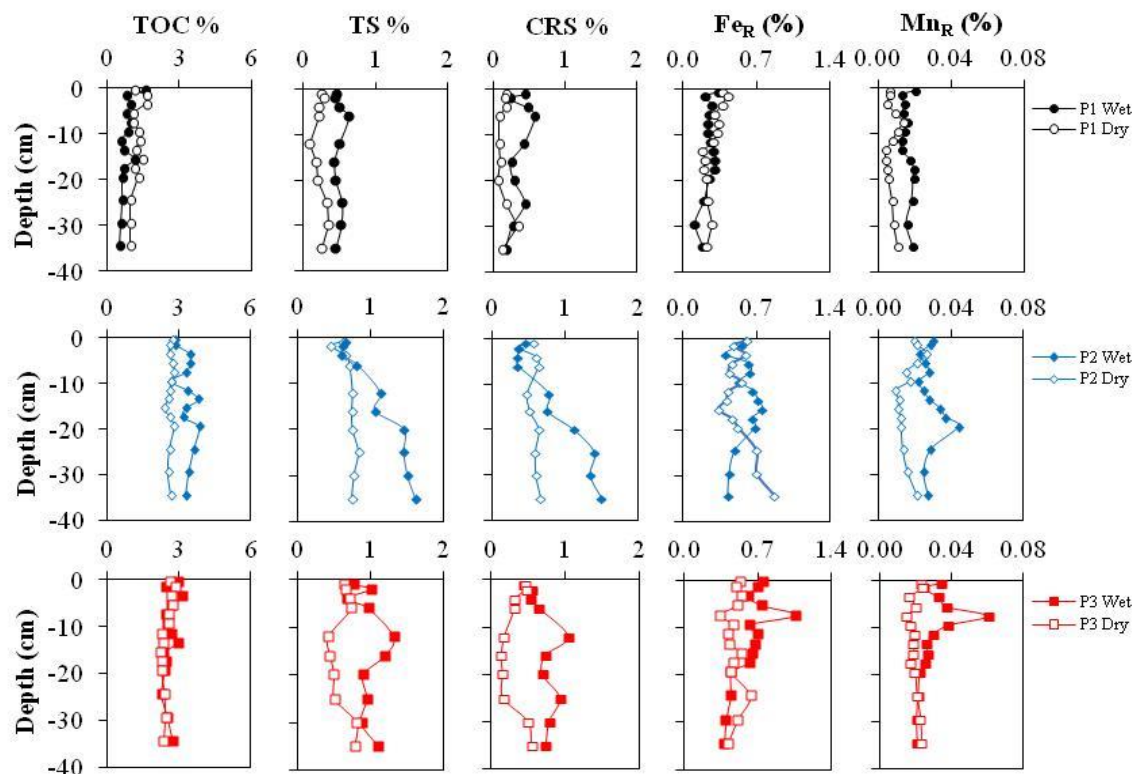


**Fig. 2** Sediment profiles of TOC, TS, CRS, Fe<sub>R</sub> and Mn<sub>R</sub> from sites P1 (black), P2 (blue) and P3 (red), during wet (solid markers) and dry (open markers) seasons

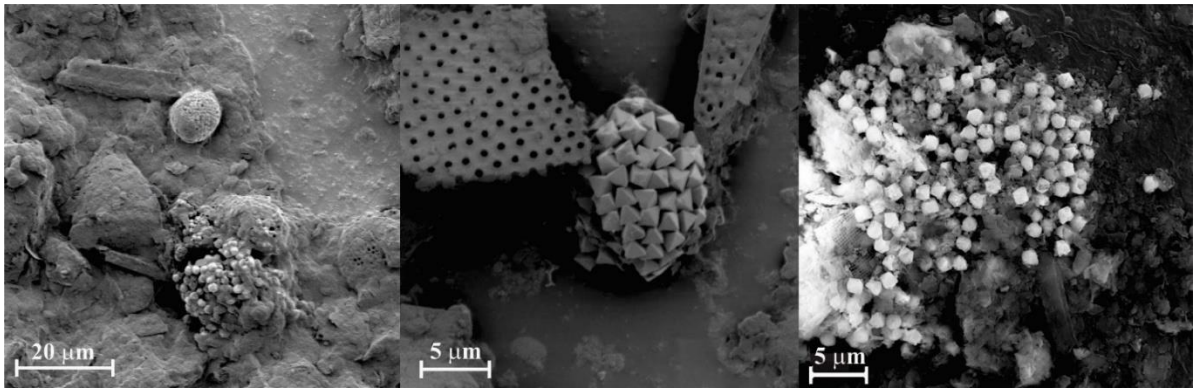


**Fig. 3** Example of pyrite crystals exhibiting a framboidal formed covered with a thin organic layer (a), around diatoms (b), and euhedral crystals (c)

### 3.2 Physicochemical characteristics

Depth profiles of salinity, pH, and Eh in overlying and pore water in different seasons are shown in Fig. 4, 5, and 6. There was a clear seasonal signal through the upper ~15 cm, with the highest values observed in the dry season compared to the wet season. During the wet season, the overlying water salinity was on average 4 and the pore water salinity increased with depth (5-20 at P1, 4-13 at P2, and 4-15 at P3). In the dry season, the overlying water salinity was on average 23 and pore water salinity showed a distinct vertical pattern, decreasing with the depth (24-19 at P1, 22-18 at P2 and 25-20 at P3). In addition, occurred a significant difference between sampling sites during the dry and wet seasons ( $p<0.05$ ). At P1 the salinity tended to remain constant below 18 cm in both seasons, while the sites P2 and P3 the salinity stabilizes below 35 cm depth. pH values were slightly acidic to neutral (6.7 to 7.4), and no seasonal variation in pH was recorded in the overlying water. The pore water pH values decreased with depth below the SWI during the wet season. By contrast, during the dry season, the pH values slightly increased with depth. The pH values were slightly more acidic during the wet season (5.9-6.5 at P1, 5.3-6.0 at P2 and 4.7-6.0 at P3) than in the dry season (6.6-7.3 at P1, 6.7-7.2 at P2 and 6.6-7.0 at P3). Eh values of overlying water were suboxic in both seasons at all sites, and ranged from 40 to 190 mV. The Eh dropped very strongly from the SWI and tended to decrease with depth, varying from -357 to -80 at P1, -220 to -125 at P2, and -180 to -95 at P3 in the wet season and from -146 to 0 at P1, -222 to -85 at P2 and, -265 to -55 at P3 in the dry season. A large

seasonal difference occurred only the site P1 ( $p<0.05$ ), which exhibited more reducing conditions during the wet season, however in the other sites there were no significant seasonal difference ( $p>0.05$ ).

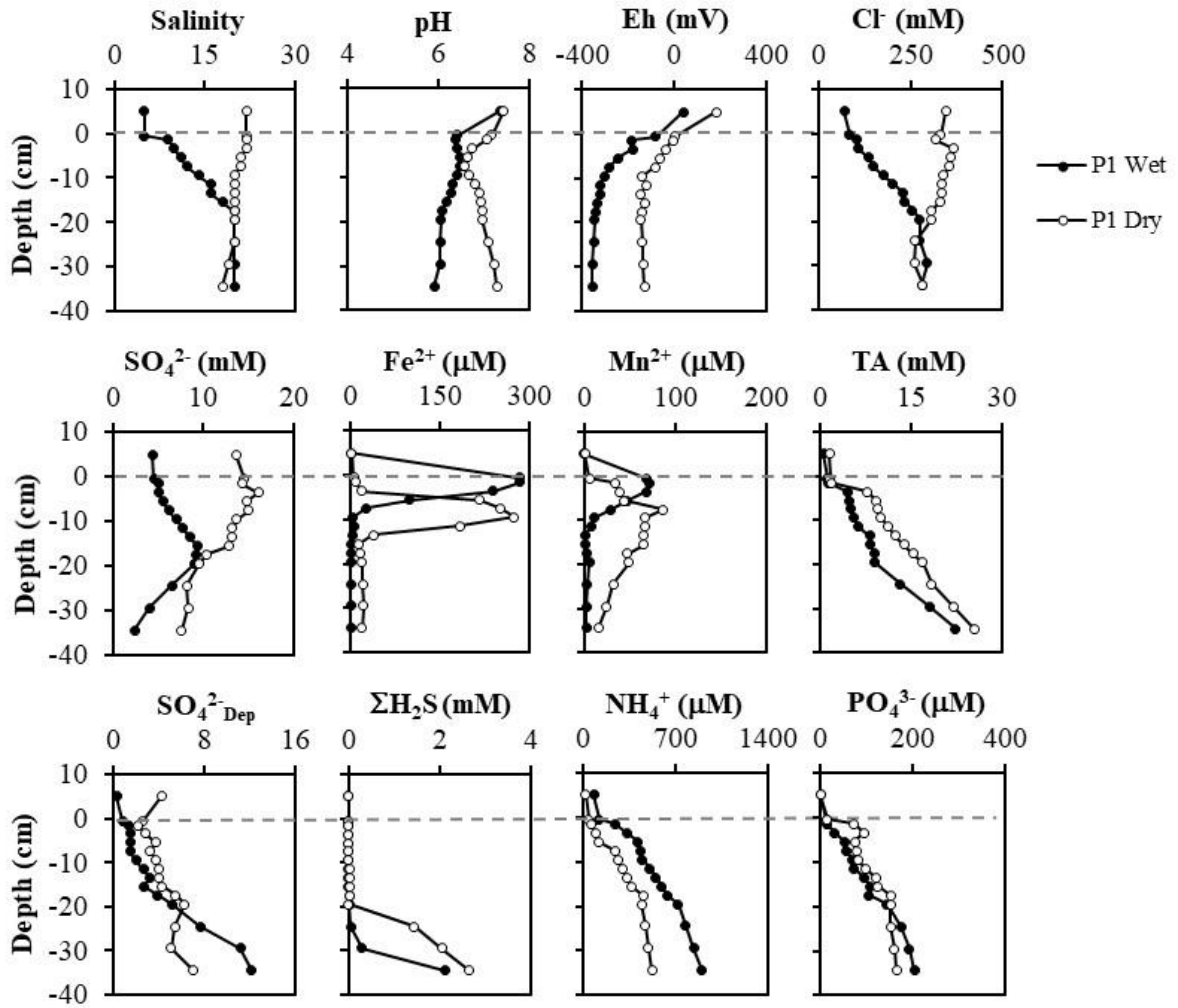


**Fig. 4** Overlying and pore water profiles of the physicochemical parameters (salinity, pH and Eh), Cl<sup>-</sup>, SO<sub>4</sub><sup>2-</sup>, redox-sensitive trace metals (Fe<sup>2+</sup> and Mn<sup>2+</sup>), total alkalinity (TA), sulfate depletion (SO<sub>4</sub><sup>2-</sup>Dep) and nutrients (NH<sub>4</sub><sup>+</sup> and PO<sub>4</sub><sup>3-</sup>) from site P1, during wet (filled circles) and dry (open circles) seasons. Dashed lines horizontally represent the SWI

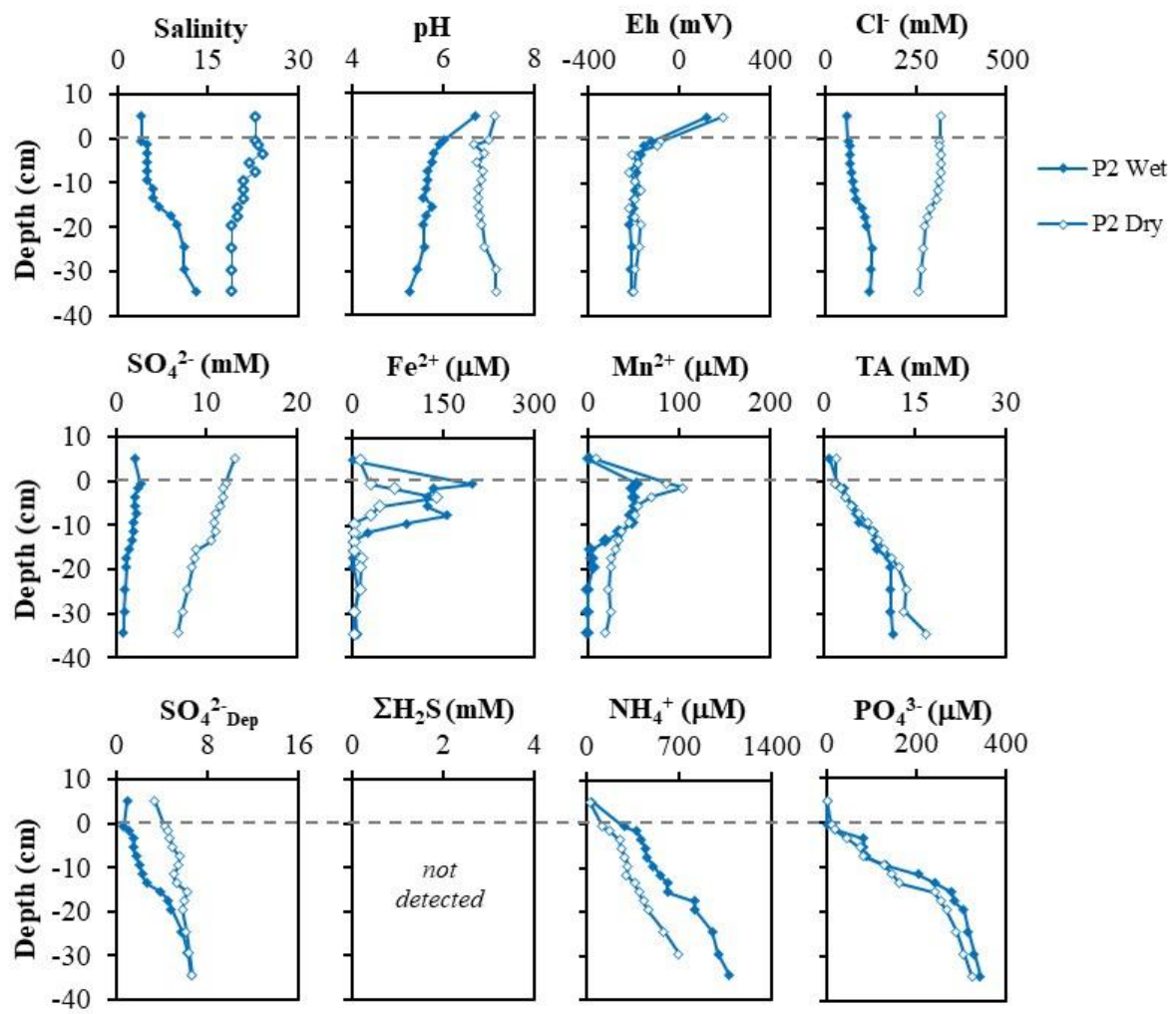


**Fig. 5** Overlying and pore water profiles of the physicochemical parameters (salinity, pH and Eh, Cl,  $\text{SO}_4^{2-}$ , redox-sensitive trace metals ( $\text{Fe}^{2+}$  and  $\text{Mn}^{2+}$ ), total alkalinity (TA), sulfate depletion ( $\text{SO}_4^{2-}\text{Dep}$ ) and nutrients ( $\text{NH}_4^+$  and  $\text{PO}_4^{3-}$ ) from site P2, during wet (filled circles) and dry (open circles) seasons. Dashed lines horizontally represent the SWI

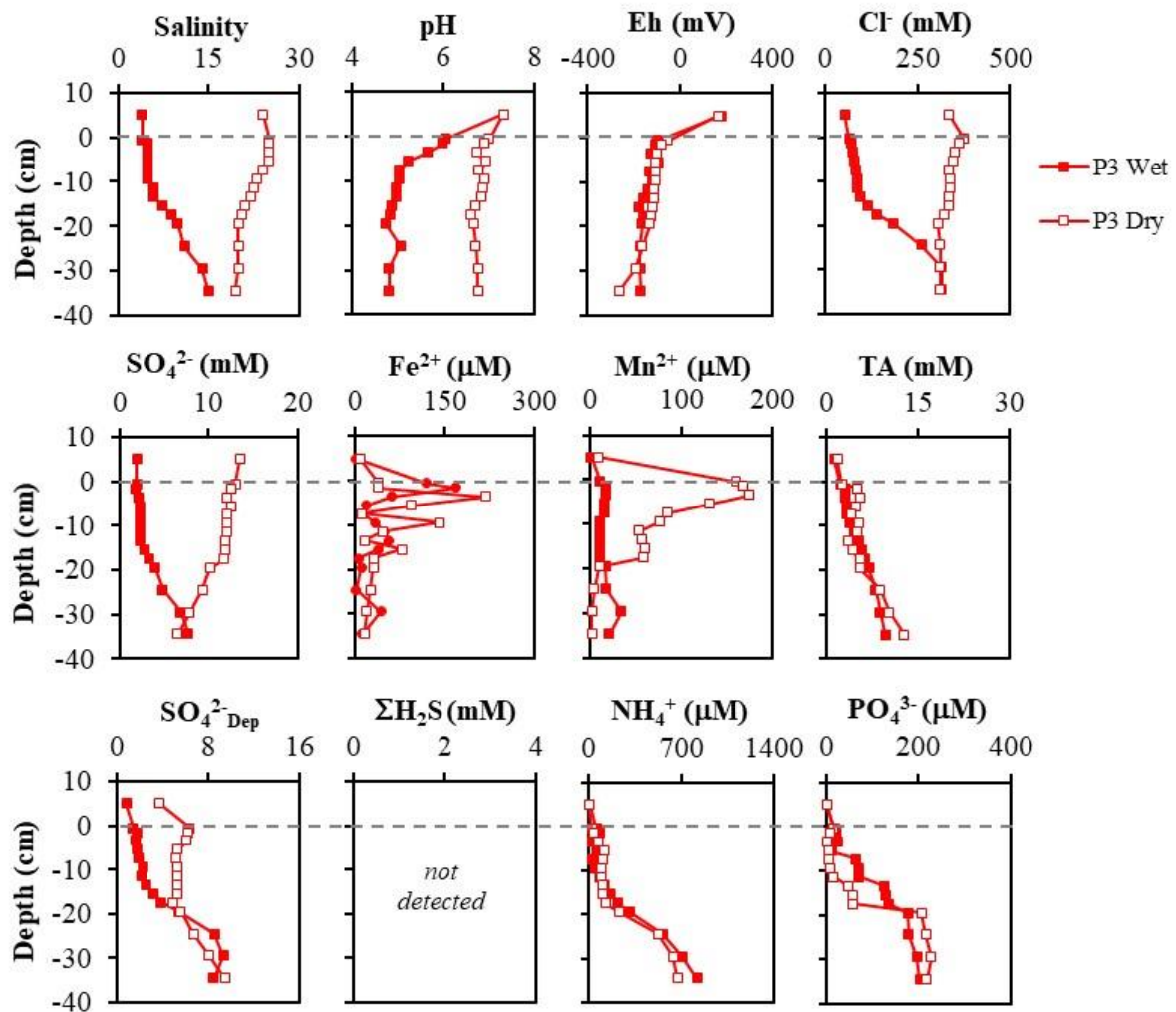


**Fig. 6** Overlying and pore water profiles of the physicochemical parameters (salinity, pH and Eh),  $\text{Cl}^-$ ,  $\text{SO}_4^{2-}$ , redox-sensitive trace metals ( $\text{Fe}^{2+}$  and  $\text{Mn}^{2+}$ ), total alkalinity (TA), sulfate depletion ( $\text{kkSO}_4^{2-}\text{Dep}$ ) and nutrients ( $\text{NH}_4^+$  and  $\text{PO}_4^{3-}$ ) from site P3, during wet (filled circles) and dry (open circles) seasons. Dashed lines horizontally represent the SWI

### 3.3 Pore water profiles of the dissolved species

Overlying and pore water profiles of  $\text{Cl}^-$ ,  $\text{SO}_4^{2-}$ , redox-sensitive trace metals ( $\text{Fe}^{2+}$  and  $\text{Mn}^{2+}$ ), total alkalinity (TA), sulfate depletion ( $\text{SO}_4^{2-}\text{Dep}$ ), and nutrients ( $\text{NH}_4^+$  and  $\text{PO}_4^{3-}$ ) at three sites during the wet and dry seasons are shown in Fig. 4, 5 and 6. The concentrations of  $\text{Cl}^-$  correlated positively with the salinity values at all sites and in both seasons ( $0.81 < r < 0.91$ , Table 1 and 2). At all sites,  $\text{Cl}^-$  concentrations increased from the overlying water to the pore water depth during the wet season (90-294 mM at P1, 59-143 mM at P2 and 54-314 mM at P3) and decreased with depth during the dry season (332-260 mM at P1, 317-260 mM at P2 and

376-310 mM at P3), corresponding to the salinity range observed seasonally and spatially, although there are subtle differences along these profiles.

The  $\text{SO}_4^{2-}$  concentrations showed a similar trend as salinity only during the dry season, with concentrations decreasing from the overlying water to the pore water at depth (16.0-7.5 mM at P1, 13.1-6.8 mM at P2 and 13.6-6.6 mM at P3). However, during the wet season, downcore pore water  $\text{SO}_4^{2-}$  displayed different characteristics at each site. At site P1, pore water  $\text{SO}_4^{2-}$  increased from overlying water with depth from 4.5 to 9.2 mM until 16 cm and then decreased with the depth to 2.4 mM. At site P2, the  $\text{SO}_4^{2-}$  concentrations decreased from overlying water with depth, varying from 2.7 to 0.8. At site P3, pore water  $\text{SO}_4^{2-}$  increased from overlying water from 1.9 to 7.7 mM.

During the wet season, sites P1, P2, and P3 featured the highest pore water  $\text{Fe}^{2+}$  concentrations closer to the SWI, reaching 285.1, 198.8, and 170.1  $\mu\text{M}$ , respectively. During the dry season, pore water  $\text{Fe}^{2+}$  concentrations were minimal in the upper centimeters, reaching 275  $\mu\text{M}$  in 10 cm at site P1, 140.2  $\mu\text{M}$  in 4 cm at site P2, and 219.3  $\mu\text{M}$  in 4 cm at site P3. During wet season, pore water  $\text{Mn}^{2+}$  concentrations were also higher closer to the SWI except for P3, reaching 72.2 at site P1 and 17.4  $\mu\text{M}$  at P2, respectively. During dry season, the  $\text{Mn}^{2+}$  peaks were located above the  $\text{Fe}^{2+}$  peaks, reaching 86.7  $\mu\text{M}$  in 8 cm at site P1, 104.7  $\mu\text{M}$  in 4 cm at site P2 and 175.7  $\mu\text{M}$  in 4 cm at site P3. For the three sites, the  $\text{Fe}^{2+}$  and  $\text{Mn}^{2+}$  concentrations drastically decreased below the peaks with increasing depths.

TA concentrations varied from 0.4 to 2.0 mM in the overlying water, and increased sharply with depth below the sediment-water interface, with concentrations ranging from 1.1 to 25.4 mM. TA pore water concentrations did not differ significantly between seasons ( $p>0.05$ ). The  $\text{SO}_4^{2-}\text{Dep}$  values increased with sediment depth at all sites, ranging from 0.6 to 12.1.  $\text{SO}_4^{2-}\text{Dep}$  did not differ significantly between sites ( $p>0.05$ ), however differed significantly between seasons just at sites P2 and P3 ( $p<0.05$ ), with slightly higher values during the dry season. Pore water  $\Sigma\text{H}_2\text{S}$  concentrations at sites P2 and P3 were negligible ( $<1 \mu\text{M}$ ), but at site P1, a high peak of 2 mM was recorded at the 35 cm depth.

$\text{NH}_4^+$  concentrations varied from 3.1 to 79.2 mM in the overlying water. The range of  $\text{NH}_4^+$  was highest at sites P1 (119.2-900.8  $\mu\text{M}$ ), and P2 (286.2-1083.8  $\mu\text{M}$ ) compared to site P3 (72.5-349.2  $\mu\text{M}$ ). Seasonal patterns were significant ( $P<0.05$ ) only at P1 and P2, where pore water concentrations were greater in the wet season. The  $\text{NH}_4^+$  pore water concentrations increased with sediment depth at all sites.  $\text{PO}_4^{3-}$  concentrations varied from 0.2 to 1.0 mM in the overlying water.  $\text{PO}_4^{3-}$  pore water concentrations did not present significant differences between

seasons ( $p>0.05$ ), but differed significantly between sites ( $p<0.05$ ), with the highest concentrations at site P2 (1.2-342.9  $\mu\text{M}$ ) compared to P1 (12.5-205.0  $\mu\text{M}$ ) and P3 (1.2-227.5  $\mu\text{M}$ ).

**Table 1** Pearson correlation matrix of geochemical variables in the wet season for the sampling sites (P1, P2, and P3)

	Salinity	pH	Eh	Cl <sup>-</sup>	SO <sub>4</sub> <sup>2-</sup>	Fe <sup>2+</sup>	Mn <sup>2+</sup>	TA	SO <sub>4</sub> <sup>2-</sup> <sub>Dep</sub>	NH <sub>4</sub> <sup>+</sup>	PO <sub>4</sub> <sup>3-</sup>
Salinity	1										
pH	0.25	1									
Eh	-0.89	-0.44	1								
Cl <sup>-</sup>	0.91	0.01	-0.69	1							
SO <sub>4</sub> <sup>2-</sup>	0.70	0.35	-0.59	0.72	1						
Fe <sup>2+</sup>	-0.48	0.38	0.48	-0.44	-0.12	1					
Mn <sup>2+</sup>	-0.47	0.29	0.42	-0.37	-0.05	0.86	1				
TA	0.89	0.23	-0.87	0.77	0.36	-0.52	-0.47	1			
SO <sub>4</sub> <sup>2-</sup> <sub>Dep</sub>	0.67	-0.30	-0.45	0.78	0.12	-0.52	-0.48	0.77	1		
NH <sub>4</sub> <sup>+</sup>	0.61	0.04	-0.58	0.53	0.06	-0.44	-0.35	0.83	0.70	1	
PO <sub>4</sub> <sup>3-</sup>	0.31	-0.35	-0.25	0.29	-0.26	-0.56	-0.51	0.58	0.64	0.81	1

**Table 2** Pearson correlation matrix of geochemical variables in the dry season for the sampling sites (P1, P2, and P3)

	Salinity	pH	Eh	Cl <sup>-</sup>	SO <sub>4</sub> <sup>2-</sup>	Fe <sup>2+</sup>	Mn <sup>2+</sup>	TA	SO <sub>4</sub> <sup>2-</sup> <sub>Dep</sub>	NH <sub>4</sub> <sup>+</sup>	PO <sub>4</sub> <sup>3-</sup>
Salinity	1										
pH	-0.24	1									
Eh	0.63	0.06	1								
Cl <sup>-</sup>	0.81	-0.48	0.56	1							
SO <sub>4</sub> <sup>2-</sup>	0.74	-0.35	0.74	0.85	1						
Fe <sup>2+</sup>	0.40	-0.44	0.23	0.48	0.48	1					
Mn <sup>2+</sup>	0.68	-0.15	0.39	0.65	0.48	0.43	1				
TA	-0.60	0.23	-0.69	-0.68	-0.91	-0.35	-0.46	1			
SO <sub>4</sub> <sup>2-</sup> <sub>Dep</sub>	-0.42	0.08	-0.67	-0.37	-0.81	-0.32	-0.13	0.84	1		
NH <sub>4</sub> <sup>+</sup>	-0.77	0.27	-0.71	-0.75	-0.82	-0.31	-0.63	0.85	0.61	1	
PO <sub>4</sub> <sup>3-</sup>	-0.74	0.19	-0.64	-0.78	-0.77	-0.40	-0.69	0.76	0.48	0.87	1

### 3.4 Fluxes of nutrients and metals at the sediment-water interface (SWI)

The estimates of diffusive fluxes of nutrient fluxes and metals at the SWI at three sites during the wet and dry seasons are shown in Table 3. At all site,  $\text{Fe}^{2+}$ ,  $\text{Mn}^{2+}$ ,  $\text{NH}_4^+$ , and  $\text{PO}_4^{3-}$ , fluxes in both season were positive, indicating export from sediments to the overlying water. In overall,  $\text{Fe}^{2+}$ ,  $\text{Mn}^{2+}$ ,  $\text{NH}_4^+$ , and  $\text{PO}_4^{3-}$  showed the highest fluxes in the wet season, except to  $\text{Mn}^{2+}$  at site P3.  $\text{Fe}^{2+}$ ,  $\text{Mn}^{2+}$ ,  $\text{NH}_4^+$ , and  $\text{PO}_4^{3-}$  fluxes varied from 6 to 723, from 16 to 189, from 90 to 1,433, and from 2 to 35  $\mu\text{mol m}^{-2} \text{ d}^{-1}$ , respectively.

**Table 3** Fluxes of  $\text{Fe}^{2+}$ ,  $\text{Mn}^{2+}$ ,  $\text{NH}_4^+$ , and  $\text{PO}_4^{3-}$  ( $\mu\text{mol m}^{-2} \text{ d}^{-1}$ ) across the SWI in the sites P1, P2 and P3, during wet and dry seasons

	P1		P2		P3	
	wet	dry	wet	dry	wet	dry
$\text{Fe}^{2+}$	723	6	595	24	238	75
$\text{Mn}^{2+}$	92	32	73	64	16	189
$\text{NH}_4^+$	415	90	1,433	155	201	121
$\text{PO}_4^{3-}$	24	18	35	14	19	2

Positive numbers indicated fluxes out of the sediment and negative numbers indicated fluxes into the sediment.

## 4 Discussion

### 4.1 Seasonal variability of physicochemical properties and $\text{Cl}^-$

Salinity oscillations were related to the seasonal variation in rainfall. In the wet season, due to increasing rainfall and runoff from the Marapanim River, the surface salinity was five times lower as relative to the dry season, indicating a greater dilution of the saline water by freshwater, as observed in Sinnamary mangrove by Marchand et al. (2004) and in Marapanim mangrove by Berrêdo et al. (2016). The seasonal effects controlled the conservative salinity and  $\text{Cl}^-$  values, especially in the upper sediment intervals (< 15 cm). Spatial variations were observed just during the wet season, with lower values of salinity and  $\text{Cl}^-$  values for the creek mudflats (P2 and P3) compared to the estuarine mudflat (P1). In the mangrove tidal creeks,

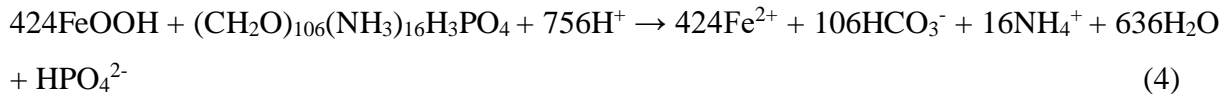
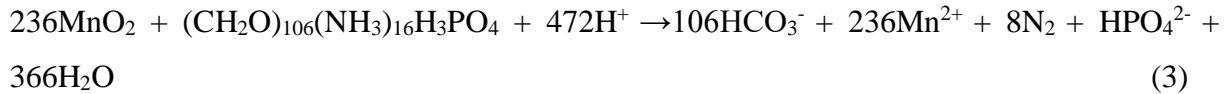
freshwater is sourced only from rainfall; no direct freshwater input from upstream riversstreams occurs. Spatial variability in salinity and  $\text{Cl}^-$  can be explained by spatial variability in grain size. The fine-grained sediments identified in the sites P2 and P3 promoted a high freshwater retention capacity. While site P1, characterized by sandy sediments (>50%), favored the saline water recharge during rising tides. At site P1, the pore water salinity tended to remain constant below 18 cm in both seasons, while sites P2 and P3 are likely to find consistent concentrations below the 35 cm depth.

The increased rainfall trend during the wet season caused a decrease in the pH values. The acidity was higher at sites P2 and P3, reaching values lower than 5 (Fig. 5-6), of which these sites have a greater freshwater retention capacity. In addition, these sites are located in topographically highest areas causing the sediments in these locations to be strongly oxidized. During dry season, saline water recharge influenced pore water quality, buffering the pH close to neutrality (6.6 - 7.3), with no significant difference between sites. Sediments more acidic in the wet season have been observed in other tropical intertidal environments (Alongi et al. 1999, 2004). Redox potential indicated suboxic to anoxic conditions at all sites. Eh values were very sensitive to seasonal change only in the site P1, where Eh values were significantly lower in the wet season than dry season (Fig. 4). However, seasonal Eh patterns were not noted at sites P2 and P3 (Fig. 5-6).

#### *4.2 Early diagenetic process and seasonal variations*

The gradual decrease of TOC content and redox potential with depth in all cores likely reflect the decomposition of OM by microorganisms. The pore water profiles allowed to assess the redox sequence of OM degradation in the mangrove mudflat sediments. Based on downcore variations in  $\text{Fe}^{2+}$  and  $\text{Mn}^{2+}$  concentrations, the sediment cores were subdivided into two distinct zones. Zone 1 (varying from 0 to 15 cm) presents peaks with high concentrations of dissolved  $\text{Fe}^{2+}$  and  $\text{Mn}^{2+}$ , revealing a suboxic zone of these sediments. This mobilization occurred because Fe and Mn oxyhydroxides are being used as terminal electron acceptors in bacterial oxidation of OM (Eq. 3 and 4) (Froelich et al. 1979), thus concentrations of Mn and Fe decreased in the solid-phase in this zone (Fig. 2). Depth sequences of high  $\text{Mn}^{2+}$  and  $\text{Fe}^{2+}$  concentrations were recorded during the dry season, as  $\text{Mn}^{2+}$  appeared in solution vertically before  $\text{Fe}^{2+}$ . However, during wet season  $\text{Mn}^{2+}$  and  $\text{Fe}^{2+}$  appeared simultaneous and closer to SWI, probably due to the strong resuspension and the impact the tidal pumping provoked by intense rainfall precipitation.

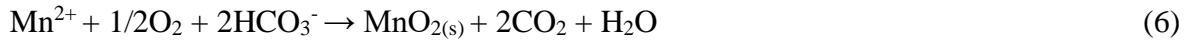
Marchand et al. (2006) also observed variations of  $\text{Fe}^{2+}$  and  $\text{Mn}^{2+}$  with depth related to seasonal fluctuation.



The mobilization intensity of  $\text{Fe}^{2+}$  and  $\text{Mn}^{2+}$  varied between sites and seasons, and can be induced by physical mixing shift, tidal fluctuation, geochemical reaction shift, as noted in previous studies (Thamdrup et al. 1994; Meiggs and Taillefert 2011; Liu et al. 2019). Pore water  $\text{Fe}^{2+}$  reached higher concentrations at site P1 ( $285.1 \mu\text{M}$ ) than P2 ( $198.8 \mu\text{M}$ ) and P3 ( $219.3 \mu\text{M}$ ). Although during the wet season the penetration of the freshwater discharge decreased significantly the pH values, which would enhance the oxyhydroxides dissolution (Otero et al. 2009, Holloway et al. 2016), the highest  $\text{Fe}^{2+}$  concentrations did not show great difference between seasons, probably as a consequence of the high iron supply from the continent (Barreiras Formation, Vilhena et al. 2010). However, the  $\text{Fe}^{2+}$  peaks were typically deeper during the dry season. The low concentrations of  $\text{Fe}^{2+}$  in the top pore water during dry season, while they increased in the surface solid phase is probably due to the  $\text{Fe}^{2+}$  oxidation and precipitation in the form of oxyhydroxides, which is likely related to the high oxygen exposure of sediment during low tide due to lower river discharge. The geochemical transformation between  $\text{Fe}^{2+}$  and amorphous  $\text{Fe(OH)}_3$  can be expressed as:



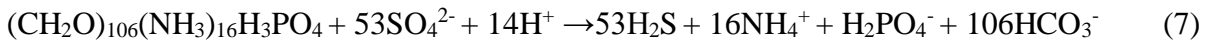
Only pore water  $\text{Mn}^{2+}$  at site P3 showed much lower concentrations during wet season, which is consistent with higher reactive concentrations of  $\text{Mn}_R$  in solid-phase (Fig. 2). In this site, the precipitation of  $\text{Mn}_R$  was probably enhanced by bioturbation activities. Sediment mixing was recorded in the surface sediment layers at site P3 by  $^{210}\text{Pb}$  profiles (Matos et al. 2020), hiding the production of pore water  $\text{Mn}^{2+}$  at the SWI. This bioturbation also can explain the variation in the top pore water  $\text{Fe}^{2+}$  concentrations at site P3. The geochemical transformation of Mn between solid and dissolved phase can be expressed as:



In zone 2 (>15 cm), the concurrent decreases in  $\text{Fe}^{2+}$  and  $\text{Mn}^{2+}$  was accompanied by a steady increase in TA,  $\text{SO}_4^{2-\text{dep}}$ ,  $\text{PO}_4^{3-}$  and  $\text{NH}_4^+$  toward the base of the core, which suggests a anoxic zone, with rapid mineralization of OM in deeper sediment layers (Fig. 4-6). The consumption of  $\text{Fe}^{2+}$  from the pore water in deeper sediments occurs due to the iron sulfide precipitation in a solid phase. Pyrite ( $\text{FeS}_2$ ) was previously observed in Marapanim mangrove sediments (Berrêdo et al. 2008a; Vilhena et al. 2010). The  $\text{Mn}^{2+}$  consumption at deeper layer could likely be associated to coprecipitation with pyrite, as previously reported (Huerta-Diaz J.W. 1992; Otero and Macias 2003; Santos-Echeandia et al. 2009). Therefore, the trend of  $\text{Fe}_R$  and  $\text{Mn}_R$  concentrations to decrease in the solid phase is a result of both the dissolution and precipitation. However, over course of tidal oscillations, multiple reduction-oxidation may occur, and  $\text{Fe}^{2+}$  and  $\text{Mn}^{2+}$  can being removed from the pore water by oxidation to form oxyhydroxides (Liu et al. 2019), which can explain the  $\text{Fe}_R$  and  $\text{Mn}_R$  peaks in the solid phase (Fig. 2). Higher  $\text{Fe}_R$  concentrations during the wet season are likely due to the increasing rainfall that drives weathering rates and sediment transport, and thus influencing the reactive iron supply from surrounding catchments (Kendall et al. 2012; Reithmaier et al. 2020).

In zone 2 (>15 cm), the concurrent decreases in  $\text{Fe}^{2+}$  and  $\text{Mn}^{2+}$  was accompanied by a steady increase in alkalinity and  $\text{SO}_4^{2-\text{dep}}$  toward the base of the core which suggests severe reducing conditions below this sediment depth (Fig. 4-6). These trends are accompanied by higher  $\text{PO}_4^{3-}$  and  $\text{NH}_4^+$  concentrations, indicating rapid mineralization of OM in deeper sediment layers (Fig. 4-6). Higher downcore  $\text{NH}_4^+$  pore water concentrations and more acidic conditions, i.e. higher pH values, during wet season indicate an enhanced early diagenesis of OM as compared to dry season. The removal of  $\text{Fe}^{2+}$  from the pore water in deeper sediments (>12 cm) seems to mark the beginning of the anoxic zone, where dissolved iron is probably fixed as iron sulfide in a solid phase.

Regression analyses between  $\text{SO}_4^{2-\text{Dep}}$  as an estimate for the metabolic amount of SR and TA as a terminal metabolic product were conducted. According to reaction (7), where the OM is sourced from phytoplankton (Redfield et al., 1963; Sholkovitz, 1973), in the case of OM degradation is mainly related to SR, it would be expected a TA: $\text{SO}_4^{2-\text{Dep}}$  ratio of 2.  $\text{SO}_4^{2-\text{Dep}}$  in pore waters is positively correlated to total alkalinity at all sites (see Table 1 and 2). In the studied sites, the TA: $\text{SO}_4^{2-\text{Dep}}$  ratio, revealed by the regression analysis slope, oscillates between 1.0 and 2.6. According to the Redfield ratio, this range indicates sulfate reducing conditions.



Then, the data of pore water profiles here reveals an intensive degradation of OM in the studied mudflats dominated by metals oxide reduction in the upper sediment layers, followed by SR in deeper sediment layers. The interpretation of redox zonation occurring in sediments was assisted by pH and Eh values that decreased because of OM microbial mineralization. This decrease was sharp at the suboxic zone and then tended to be almost constant in the anoxic zone. Seasonal effects, mainly controlled by freshwater discharge, affected the downcore profiles of the  $SO_4^{2-}$ <sub>Dep</sub> in the pore water of these sediments. In the wet season, the sulfate depletion was not appreciable in the layers from the top sediment (< 15 cm) at all sites, due to the dilution-mixing that produces a more efficient removal of the sulfate than bacterial SR in these layers. Below the dilution-mixing layers, however, sulfate depletion increased abruptly. Similar seasonal trends were also observed by Wu et al. (2015) in Pearl River estuary. The SR products (TA,  $NH_4^+$  and  $PO_4^{3-}$ ) indicated no simple mixing trend in the dilution-mixing layer (Fig. 4-6). It suggests that the TA,  $NH_4^+$  and  $PO_4^{3-}$  pore waters are substantially changed by diagenetic reactions, such as Fe and Mn reduction. However, only pore water  $NH_4^+$  showed seasonal variability, with the highest concentrations found in the wet season. A similar phenomenon was recorded by Meiggs and Taillefert (2011), who investigated seasonal effects on biogeochemical processes in estuarine sediments. They report that dilution-mixing does not cause seasonal changes in the SR products.

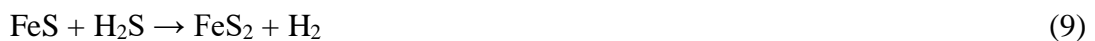
Since the sedimentary OM in the study sites is mainly sourced from marine phytoplankton input (49% to 95%, Matos et al. 2020), which is more labile OM than terrestrial material, the availability of TOC did not control SR. Thus, along these mudflat sediments, the SR was mainly controlled by the pore water  $SO_4^{2-}$ . It has been reported previously that sulfate availability can regulate sulfate reducing activity when concentrations reach low levels < 10 mM (Goldhaber and Kaplan 1974; Naik et al. 2019). During the wet season pore water  $SO_4^{2-}$  concentrations were always below 10 mM, Pore water  $SO_4^{2-}$  reached concentrations above 10 mM only in upper layers in the dry season.

The suboxic to anoxic sediment conditions limits the aerobic decomposition of OM. The IR and SR are energetically less favorable decomposition processes thus enhancing OM burial. As previously observed by Matos et al. (2020), these sites have higher potential to accumulates COT, TN and PT in their sediments, especially in the creek mudflats (P2 and P3). The mudflat sediment in the Marapanim River margin (site P1) reached higher concentrations of terminal

metabolic end-products of OM mineralization, such as  $\text{Fe}^{2+}$ ,  $\text{SO}_4^{2-\text{Dep}}$ ,  $\text{H}_2\text{S}$  and TA, which suggest that the OM of this estuarine mudflat is more susceptible to decomposition compared to the OM on the mangrove creek mudflats. Coarse-textured sediment and higher available labile OM (Matos et al. 2020) certainly contributed to more susceptible OM degradation in the site P1.

#### *4.3 Pyrite formation*

Soluble sulfur compounds ( $\Sigma\text{H}_2\text{S}$ ) produced by sulfate reducing bacteria can react with detrital iron minerals to form iron sulfides, e.g.,  $\text{FeS}$  (Eq. 8) and  $\text{FeS}_2$  (Eq. 9). Pyrite is the main product of sulfate reduction in mangrove sediments (Kristensen et al. 1991; Holmer et al. 1994; Alongi et al. 1998; Sherman et al. 1998; Ding et al. 2014; Reithmaier et al. 2020). However, intensive oxidation of the sediments caused, for instance, by tides can invert that process and reoxidize pyrite to Fe oxy-hydroxides (Eq. 10) (Sherman et al. 1998; Marchand et al. 2005). Elevated  $\text{Fe}_R$  and CRS concentrations (Fig. 7c), and abundant pyrite framboids observed under SEM (Fig. 3) give evidence of the presence of sedimentary pyrite in great amount. CRS showed a good correlation with TS ( $r = 0.65$ , Fig. 7b), which indicates that most of the S is preferably being incorporated into the inorganic matrix (> 90 %). The small size of the framboids indicates a rapid formation of pyrite in this study environment.



The pyrite formation is generally regulated by the availability of sulfate, reactive iron, or labile organic carbon (Berner 1984, Goldhaber 2004). The TOC/CRS values exceeded the empirical TOC/CRS ratio for “normal” marine sediments (~2.8; Berner and Raiswell, 1983), and our results showed a low positive correlation between CRS and TOC contents ( $r^2 = 0.21$ , Fig. 7a), suggesting that the TOC content was not the main limiting factor for pyrite formation at our study sites.  $\text{Fe}_R$  was higher at all sites, with low correlation with CRS ( $r^2 = 0.12$ , Fig. 7c), indicating that  $\text{Fe}_R$  was also not limiting to the pyrite formation. Considering the pore water is devoid of free sulfide at sites P2 and P3, and appear at site P1 only in deeper layers, a tight coupling between sulfide production via SR, and sulfide consumption by pyrite formation may be proposed (Raiswell and Canfield 1998). The  $\Sigma\text{H}_2\text{S}$  produced by SR may be available for

$\text{FeS}_2$  formation, the major end product of SR in mangroves. However, the low  $\Sigma\text{H}_2\text{S}$  and AVS (mainly FeS) contents can also be due to intense oxidation and pore water exchange during the air exposure in the low tides. Further pyrite formation at our study sites may be limited by the low  $\Sigma\text{H}_2\text{S}$  contents, which can be either be due to low sulfate availability or sulfide reoxidation (Berner 1984).

The concentration of CRS varied widely between seasons and between the studied sites. Overall, CRS concentrations in the sediments were highest in the sites with higher TOC concentrations and during the wet period. Lower CRS concentrations during dry season, principally at sites P2 and P3 is probably due to these sites being located in topographically higher areas and their sediments are strongly oxidized especially during dry season, promoting the oxidation of pyrite. Pyrite oxidation was previously observed in Marapanim mangrove sediments by Vilhena et al. (2010), they observed oxidation of pyrite grains surface and the presence of jarosite mineral as a product of pyrite oxidation, which was associated with clay fractions.

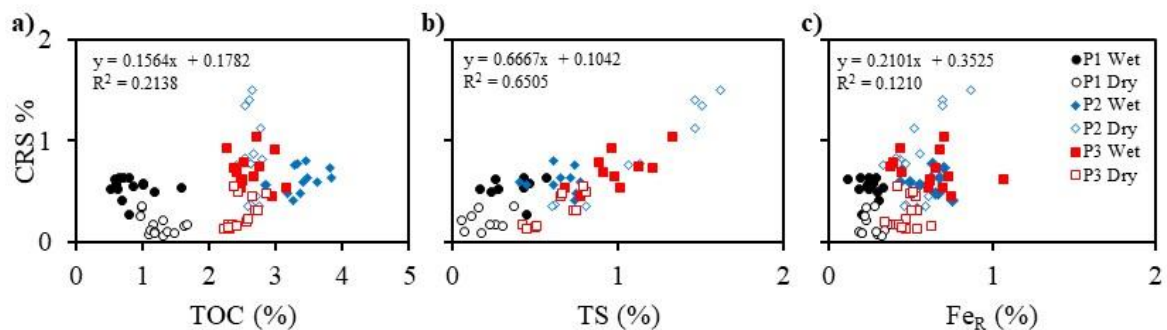


**Fig. 7** CRS against TOC (a), CRS against TS (b), and CRS against  $\text{Fe}_R$  (c)

#### 4.4 Seasonal variability of diffusive fluxes at the SWI

A great amount of  $\text{Fe}^{2+}$  and  $\text{Mn}^{2+}$  are produced by microbial Fe and Mn reduction, respectively, which diffused from the sediment into the overlying water, making the studied mud-flats a source of  $\text{Fe}^{2+}$  and  $\text{Mn}^{2+}$ . The changes in diagenetic processes induced by the increasing in rainfall must have promoted variable diffusive fluxes. In the wet season, the highest concentration of  $\text{Fe}^{2+}$  was found just below SWI, which generated higher fluxes in this period. However, in the dry season,  $\text{Fe}^{2+}$  showed lower concentrations in the top sediment layers, probably because the high oxygen exposure of sediment during low tide enhanced Fe in his oxidized solid phase, which severely limited its diffusion to the overlying water.  $\text{Mn}^{2+}$  fluxes followed the same trend of  $\text{Fe}^{2+}$  fluxes, except to the site P3 that showed lower fluxes in the wet season, as a result sediment mixing promoted lower concentrations of  $\text{Mn}^{2+}$  in the surface sediment.

Marchand et al. (2005) also observed higher dissolved Fe and Mn fluxes during wet than dry season, as a result of vertical oscillations in redox status.

At all sites, the sediment constitutes a source of  $\text{PO}_4^{3-}$  and  $\text{NH}_4^+$  to the water column, and these fluxes are higher during the wet than dry season. As observed by Taillardat et al. (2019), intense rainfall events reduce pore water salinity and enhance OM decomposition, which is likely to increase phosphate and nitrogen mineralization. The high  $\text{NH}_4^+$  pore water concentrations and the good correlation between  $\text{NH}_4^+$  and  $\text{SO}_4^{2-}_{\text{Dep}}$  pore water in both seasons ( $r = 0.61 - 0.70$ , Table 1 and 2) reveals a high OM mineralization (ammonification), that is more intense during the wet season, with higher downcore pore water concentrations. Because no permanent macrophytic vegetation is present in the mudflat to consume the dissolved nutrients (Taillardat et al. 2019), the mudflats are a source of  $\text{NH}_4^+$  that accumulates and becomes available for nitrification or discharge via pore water seepage.

$\text{PO}_4^{3-}$  pore water concentrations also showed a significant positive correlation with  $\text{SO}_4^{2-}_{\text{Dep}}$  pore water in the wet season ( $r = 0.64$ , Table 1), but this positive correlation receded in the dry season ( $r = 0.48$ , Table 2), due to the enhanced  $\text{SO}_4^{2-}_{\text{Dep}}$  in the upper layers, that did not affect downcore pore water  $\text{PO}_4^{3-}$ . Studies have indicated that the release or adsorption of P in coastal sediments is associated with the iron redox cycle (Sherman et al., 1998; Ding et al., 2016). P is potently adsorbed by Fe oxy-hydroxides under more oxidizing conditions. By contrast, more reducing conditions favor its mobility from the sediments to the pore waters (Bava and Seralathan 1999). However, the low remobilisation of  $\text{PO}_4^{3-}$  in the upper layers where the IR occurs implies that the release of  $\text{PO}_4^{3-}$  was not related to Fe-bound P in our study sites. A low negative correlation between  $\text{PO}_4^{3-}$  and  $\text{Fe}^{2+}$ , and significant positive correlations between  $\text{PO}_4^{3-}$  and  $\text{NH}_4^+$  and TA (Table 1 and 2) reinforces the assumption that the release of the  $\text{PO}_4^{3-}$  to pore water was mainly derived through the OM mineralization by SR.

The diffusion fluxes of  $\text{Mn}^{2+}$  and  $\text{Fe}^{2+}$  are on the same order of magnitude as those reported to other mangrove forest (Alongi et al. 2001) and mangrove creek (Holloway et al. 2016). The fluxes of  $\text{NH}_4^+$  and  $\text{PO}_4^{3-}$  are comparable to those measured in other mangrove creek (Tait et al. 2017), but are lower than other mangrove creeks (Gleeson et al. 2013). Although  $\text{PO}_4^{3-}$  and  $\text{NH}_4^+$  pore water reached high concentrations of 343  $\mu\text{M}$  and  $>1000 \mu\text{M}$ , respectively, at depth, their diffusive fluxes appear be retarded in suboxic conditions.

#### 4.5 Pore water solute flux x depositional fluxes

We converting the fluxes in mmol m<sup>-2</sup> d<sup>-1</sup> to g m<sup>-2</sup> yr<sup>-1</sup> to compare with the burial fluxes. Total nitrogen and total phosphorous depositional fluxes were obtained from Matos et al. (2020), and Fe and Mn depositional fluxes were estimated from reactive Fe and Mn concentrations, sediment accumulation and dry bulk density, obtained previously by Matos et al. (2020). The average between the three study sites, propagate to the average between the wet and dry season dataset, of the calculated diffusive fluxes from the pore water to the overlying water column for N (as NH<sub>4</sub><sup>+</sup>), P (as PO<sub>4</sub><sup>3-</sup>), Fe (as Fe<sup>2+</sup>) and Mn (as Mn<sup>2+</sup>) were 2.6, 0.5, 5.7, and 1.6 g m<sup>-2</sup> yr<sup>-1</sup>, respectively. Regarding the total N, P, Fe and Mn the depositional fluxes were 15.3, 3.2, 42.3 and 6.9 g m<sup>-2</sup> yr<sup>-1</sup>, respectively (Table 4). On average, the release of dissolved NH<sub>4</sub><sup>+</sup>, PO<sub>4</sub><sup>3-</sup>, Fe<sup>2+</sup> and Mn<sup>2+</sup> from the pore water to the overlying water corresponds to ~17, 16, 7 and 90 % of the total amount of N, P, Fe and Mn deposited to the sediment, respectively (Table 4).

**Table 4** Upward dissolved fluxes of NH<sub>4</sub><sup>+</sup>, PO<sub>4</sub><sup>3-</sup>, Fe<sup>2+</sup> and Mn<sup>2+</sup>, and depositional fluxes of total N and P and reactive Fe and Mn at sites P1, P2, and P3

Site	Diffusive flux				Depositional flux				Recycling				Burial			
	(g m <sup>-2</sup> yr <sup>-1</sup> )				(g m <sup>-2</sup> yr <sup>-1</sup> )				%				%			
	N	P	Fe	Mn	N	P	Fe	Mn	N	P	Fe	Mn	N	P	Fe	Mn
P1	1.4	0.7	3.8	1.3	11.0	2.7	37.2	1.8	12.8	27.2	9.4	70.2	87.2	72.8	90.6	29.8
P2	5.2	0.4	2.4	1.4	16.4	3.1	42.7	1.6	31.9	11.7	6.9	86.1	68.1	88.3	93.1	13.9
P3	1.1	0.4	2.1	2.1	18.4	3.9	47.0	2.1	5.8	9.4	4.4	112.3	94.2	90.6	95.6	-12.3
Average	<b>2.6</b>	<b>0.5</b>	<b>5.7</b>	<b>1.6</b>	<b>15.3</b>	<b>3.2</b>	<b>42.3</b>	<b>1.8</b>	<b>16.8</b>	<b>16.1</b>	<b>14.7</b>	<b>89.5</b>	<b>83.2</b>	<b>83.9</b>	<b>85.3</b>	<b>10.5</b>

Mangrove Marapanim is characterized to have high concentrations of Fe in its sediment with a mean of 6.5 % (Vilhena et al. 2010). The reactive Fe concentrations found in these mudflat sediments correspond to <10 % to that found in the mangrove forest, this highlights the Fe burial efficiency (85%) of Marapanim mudflats although their high recycling to overlying water. By contrast, Berrêdo et al. (2008) observed lower total Mn concentrations (0.03%) than that we found in this mudflat that reached 0.06%. Therefore, this high potential recycling of ~90 % corroborate with Holloway et al. (2016) that undisturbed mangrove creeks may be a major source of Mn<sup>2+</sup> to the coastal ocean. The N and P burial efficiency (~84 %) is driven by the suboxic conditions, where IR and MnR appear limits PO<sub>4</sub><sup>3-</sup> and NH<sub>4</sub><sup>+</sup> pore water mobilization and their fluxes to overlying surface waters.

Intertidal mudflat sediments are submitted to intense oscillations related to tidal heights, which may enhance loss of nutrients and metals dissolved by lateral tidal drainage, advection or groundwater transport (Sanders et al. 2015; Holloway et al. 2016; Tait et al. 2017). These processes may result in low gradients in pore water concentrations within the dilution-mixing zone, and consequently underestimate the diffusive fluxes. Bioturbation activities may also increases sediment oxygen supply and a fraction of produced  $\text{Fe}^{2+}$ ,  $\text{Mn}^{2+}$  and  $\text{NH}_4^+$  might be oxidized in the upper layers where suboxic conditions can be found. Therefore, diffusive fluxes based only on molecular diffusion and the gradient concentration at the SWI represents just an estimative of how these mudflat sediments can act as a source to water column.

## 5 Conclusions

This study investigated the influence of seasonal rainfall patterns on physicochemical properties, diagenetic process, and nutrient and metals exchange rates in the sediment-water interface (SWI) in three intertidal mudflat sediments fringed by pristine mangroves, located in northern Brazil. From the dry to the wet season, there was a seasonal shift to more acidic and more reducing conditions, a decline in the pore water salinity, and an increase in the concentrations of elements within the pore water and sediments. This change was most likely due to seepage and dilution by rainwater at low tide and by tidal water dilution through increased freshwater runoff. The seasonal variability in rainfall caused strong seasonal changes, especially in the upper surface layer that is referred to dilution-mixed zone. At the three sites, the decrease with the depth of TOC, pH, and Eh, in parallel with the increase of TA,  $\text{SO}_4^{2-\text{dep}}$ ,  $\text{NH}_4^+$  and  $\text{PO}_4^{3-}$  pore water concentrations directly reflect the mineralization of OM during burial and resulting redox reactions. In the dilution-mixing zone, Fe (III) and Mn (IV) reduction are the dominant anaerobic respiratory processes in the sediments. The redox zonation of sediments oscillated in response to the rainfall pattern. In the wet season, the highest concentration of  $\text{Fe}^{2+}$  and  $\text{Mn}^{2+}$  was found just below SWI, which generated higher fluxes in this period. In the dry season, the precipitation of Fe and Mn oxy-hydroxides in the surface sediments limited their diffusion to the water column. Below the dilution-mixing, SR was enhanced significantly. Between of SR products (TA,  $\text{NH}_4^+$  and  $\text{PO}_4^{3-}$ ), only  $\text{NH}_4^+$  pore water showed seasonal variability, with higher concentrations during the wet season. Variations between sites are mainly attributed to topography, OM sources, and sedimentary conditions. The mudflat sediment in the Marapanim River margin (site P1) reached higher concentrations of terminal metabolic end-products of OM mineralization, such as  $\text{Fe}^{2+}$ ,  $\text{SO}_4^{2-\text{Dep}}$ ,  $\text{H}_2\text{S}$  and TA, which suggest that the OM of this

estuarine mudflat is more susceptible to decomposition compared to the OM on the mangrove creek mudflats. Coarse-textured sediment and higher available labile OM certainly contributed to more susceptible OM degradation in the site P1. In addition, temporal variability in pyrite formation revealed that the solid phase retention mechanisms are also susceptible to seasonal effects, with lower concentrations of chromium-reducible sulfur (CRS, mainly pyrite fraction) during the dry season. The sites P2 and P3 located in topographically highest areas were more susceptible to losses in pyrite concentrations during the dry season. Under suboxic conditions, the mudflat sediments constitute a source of  $\text{Fe}^{2+}$ ,  $\text{Mn}^{2+}$ ,  $\text{NH}_4^+$  and  $\text{PO}_4^{3-}$  to the water column, and intense rainfall drives metals and nutrient pore water exchange. Marapanim mudflats are quite effective in retaining nutrients and iron than exporting to the coastal waters, while can potentially be a significant contributor to oceanic Mn cycle. Therefore, this examination of the influence of the Amazonian seasonal rainfall patterns revealed substantial changes of physico-chemical properties and the diagenetic processes, affecting the release of metals and nutrients from the SWI. These finding evidenced the role of mangrove-fringed tidal creeks as biogeochemical reactors, rather than simple conduits of dissolved metals and nutrients between mangrove wetlands and the coastal ocean, which may contribute to determine the metals and nutrients exchanges via mangrove creek water.

### **Acknowledgments**

The authors thank the research grants from the Brazilian Ministry of Education (CAPES) and the Brazilian Research Council (CNPq) to the first author C.R.L. Matos. C.J. Sanders is supported by the Australian Research Council (DE160100443) and E. Metzger by CNRS-EC2CO project Vubleu. W. Machado thanks the CAPES-Print-Feedbacks Project (Proc. No. 88887.310301/2018-00). Rut Diaz from Universidade Federal Fluminense (UFF) is thanked for her assistance with the pyrite analysis. We also acknowledge the Evandro Chagas Institute (IEC) and Museu Goeldi (MPEG) for supplied facilities to use their laboratories.

### **References**

- Alongi D., Sasekumar A, Tirendi F, Dixon P (1998) The influence of stand age on benthic decomposition and recycling of organic matter in managed mangrove forests of Malaysia. *J Exp Mar Bio Ecol* 225:197–218. [https://doi.org/10.1016/S0022-0981\(97\)00223-2](https://doi.org/10.1016/S0022-0981(97)00223-2)
- Alongi DM (1995) Decomposition and recycling of organic matter in muds of the Gulf of Papua, northern Coral Sea. *Cont Shelf Res* 15:1319–1337. <https://doi.org/10.1016/0278-0022-00022-3>

- 4343(94)00087-4
- Alongi DM (2020) Global Significance of Mangrove Blue Carbon in Climate Change Mitigation ( Version 1 ). Sci 2:1–15. <https://doi.org/10.3390/sci2030057>
- Alongi DM, Tirendi F, Dixon P, et al (1999) Mineralization of organic matter in intertidal sediments of a tropical semi-enclosed delta. Estuar Coast Shelf Sci 48:451–467. <https://doi.org/10.1006/ecss.1998.0465>
- Alongi DM, Wattayakorn G, Boyle S, et al (2004) Influence of roots and climate on mineral and trace element storage and flux in tropical mangrove soils. Biogeochemistry 69:105–123. <https://doi.org/10.1023/B:BIOG.0000031043.06245.af>
- Anschutz P, Dedieu K, Desmazes F, Chaillou G (2005) Speciation, oxidation state, and reactivity of particulate manganese in marine sediments. Chem Geol 218:265–279. <https://doi.org/10.1016/j.chemgeo.2005.01.008>
- Bava KA, Seralathan P (1999) Interstitial water and hydrochemistry of a mangrove forest and adjoining water system , south west coast of India. Environ Geol 38:47–52
- Berner RA (1980) Early Diagenesis - A Theoretical Approach. Princeton University Press, New Jersey
- Berner RA (1984) Sedimentary pyrite formation: An update. Geochim Cosmochim Acta 48:605–615. [https://doi.org/10.1016/0016-7037\(84\)90089-9](https://doi.org/10.1016/0016-7037(84)90089-9)
- Berner RA, Raiswel R (1983) Burial of organic carbon and pyrite sulfur in sediments over Phanerozoic time: a new theory. Geochim Cosmochim Acta 47:855–862. [https://doi.org/10.1016/0016-7037\(83\)90151-5](https://doi.org/10.1016/0016-7037(83)90151-5)
- Berrêdo JF, Costa ML da, Vilhena M do PSP, Santos JT dos (2008a) Mineralogia e geoquímica de sedimentos de manguezais da costa amazônica: o exemplo do estuário do rio Marapanim (Pará). Rev Bras Geociências 38:24–35. <https://doi.org/10.25249/0375-7536.20083812435>
- Berrêdo JF, Costa ML da, Vilhena MSP, Matos CRL (2016) Modificações nas propriedades físico-químicas de sedimentos de manguezais submetidos ao clima amazônico Changes in physicochemical properties of mangrove sediments under Amazonian climatic regime. Bol do Mus Para Emílio Goeldi Ciências Nat 11:313–328
- Berrêdo JF, Costa ML, Socorro P (2008b) Efeitos das variações sazonais do clima tropical úmido sobre as águas e sedimentos de manguezais do estuário do rio Marapanim , costa nordeste do Estado do Pará. Acta Amaz 38:473–482. <https://doi.org/http://dx.doi.org/10.1590/S0044-59672008000300012>
- Bouillon S, Middelburg JJ, Dehairs F, et al (2007) Importance of intertidal sediment

- processes and porewater exchange on the water column biogeochemistry in a pristine mangrove creek (Ras Dege, Tanzania). *Biogeosciences* 4:311–322.  
<https://doi.org/10.5194/bg-4-311-2007>
- Breithaupt JL, Smoak JM, Smith III TJ, Sanders CJ (2014) Temporal variability of carbon and nutrient burial, sediment accretion, and mass accumulation over the past century in a carbonate platform mangrove forest of the Florida Everglades. *J Geophys Res Biogeosci* 119:2032–2048. <https://doi.org/10.1002/2014JG002715>.Received
- Cline JD (1969) SPECTROPHOTOMETRIC DETERMINATION OF HYDROGEN SULFIDE IN NATURAL WATERS1. *Limnol Oceanogr* 14:454–458.  
<https://doi.org/10.4319/lo.1969.14.3.0454>
- Ding H, Yao S, Chen J (2014) Authigenic pyrite formation and re-oxidation as an indicator of an unsteady-state redox sedimentary environment: Evidence from the intertidal mangrove sediments of Hainan Island, China. *Cont Shelf Res* 78:85–99.  
<https://doi.org/10.1016/j.csr.2014.02.011>
- Fossing H, Jørgensen B (1989) Measurement of bacterial sulfate reduction in sediments: Evaluation of a single-step chromium reduction method. *Biogeochemistry* 8:205–222.  
<https://doi.org/10.1007/BF00002889>
- Froelich PN, Klinkhammer GP, Bender ML, et al (1979) Early oxidation of organic matter in pelagic sediments of the eastern equatorial Atlantic: suboxic diagenesis. *Geochim Cosmochim Acta* 43:1075–1090. [https://doi.org/10.1016/0016-7037\(79\)90095-4](https://doi.org/10.1016/0016-7037(79)90095-4)
- Gieskes JM, Gamo T, Brumsack H (1991) Chemical Methods for Interstitial Water Analysis aboard JOIDES Resolution
- Glud RN (2008) Oxygen dynamics of marine sediments. *Mar Biol Res* 4:243–289.  
<https://doi.org/10.1080/17451000801888726>
- Hammer Ø, Harper DAT, Ryan PD (2001) PAST : PALEONTOLOGICAL STATISTICS SOFTWARE PACKAGE FOR EDUCATION AND DATA ANALYSIS. *Palaeontol Electron* 4:1–9
- Holloway CJ, Santos IR, Tait DR, et al (2016) Manganese and iron release from mangrove porewaters: A significant component of oceanic budgets? *Mar Chem* 184:43–52.  
<https://doi.org/10.1016/j.marchem.2016.05.013>
- Holmer M, Kristensen E, Banta G, et al (1994) Biogeochemical cycling of sulfur and iron in sediments of a south-east Asian mangrove, Phuket Island, Thailand. *Biogeochemistry* 26:145–161. <https://doi.org/10.1007/BF00002904>
- Huerta-Diaz J.W. MAA-M (1992) Pyritization of trace metals in anoxic marine sediments:

- RN - Geochim. Cosmochim. Acta, v. 56, p. 2681-2702. Geochim Cosmochim Acta 56: Kauffman JB, Bernardino AF, Ferreira TO, et al (2018) Carbon stocks of mangroves and salt marshes of the Amazon region, Brazil. Biol Lett 14:. <https://doi.org/10.1098/rsbl.2018.0208>
- Kendall B, Anbar AD, Kappler A, Konhauser KO (2012) The Global Iron Cycle. In: Fundamentals of Geobiology. John Wiley & Sons, Ltd, Chichester, UK, pp 65–92
- Kostka JE, Luther GW (1994) Partitioning and speciation of solid phase iron in saltmarsh sediments. Geochim Cosmochim Acta 58:1701–1710. [https://doi.org/10.1016/0016-7037\(94\)90531-2](https://doi.org/10.1016/0016-7037(94)90531-2)
- Kristensen E, Holmer M, Bussarawit N (1991) Benthic metabolism and sulfate reduction in a Southeast Asian mangrove swamp. Mar Ecol Prog Ser 73:93–103. <https://doi.org/10.3354/meps073093>
- Kristensen E, King G, Holmer M, et al (1994) Sulfate reduction, acetate turnover and carbon metabolism in sediments of the Ao Nam Bor mangrove, Phuket, Thailand. Mar Ecol Prog Ser 111:245–255. <https://doi.org/10.3354/meps111245>
- Kristensen E, Mangion P, Tang M, et al (2011) Microbial carbon oxidation rates and pathways in sediments of two Tanzanian mangrove forests. Biogeochemistry 103:143–158. <https://doi.org/10.1007/s10533-010-9453-2>
- Ku TCW, Kay J, Browne E, et al (2008) Pyritization of iron in tropical coastal sediments: Implications for the development of iron, sulfur, and carbon diagenetic properties, Saint Lucia, Lesser Antilles. Mar Geol 249:184–205. <https://doi.org/10.1016/j.margeo.2007.12.001>
- Lee RY, Porubsky WP, Feller IC, et al (2008) Porewater biogeochemistry and soil metabolism in dwarf red mangrove habitats (Twin Cays, Belize). Biogeochemistry 87:181–198. <https://doi.org/10.1007/s10533-008-9176-9>
- Li Y-H, Gregory S (1974) Diffusion of ions in sea water and in deep-sea sediments. Geochim Cosmochim Acta 38:703–714. [https://doi.org/10.1016/0016-7037\(74\)90145-8](https://doi.org/10.1016/0016-7037(74)90145-8)
- Liu Y, Not C, Jiao JJ, et al (2019) Tidal induced dynamics and geochemical reactions of trace metals (Fe, Mn, and Sr) in the salinity transition zone of an intertidal aquifer. Sci Total Environ 664:1133–1149. <https://doi.org/10.1016/j.scitotenv.2019.01.374>
- Marchand C, Baltzer F, Lallier-Vergès E, Albéric P (2004) Pore-water chemistry in mangrove sediments: Relationship with species composition and developmental stages (French Guiana). Mar Geol 208:361–381. <https://doi.org/10.1016/j.margeo.2004.04.015>
- Marchand C, Lallier-Vergès E, Allenbach M (2011) Redox conditions and heavy metals

- distribution in mangrove forests receiving effluents from shrimp farms (Teremba Bay, New Caledonia). *J Soils Sediments* 11:529–541. <https://doi.org/10.1007/s11368-010-0330-3>
- Marchand C, Lallier-Vergès E, Baltzer F, et al (2006) Heavy metals distribution in mangrove sediments along the mobile coastline of French Guiana. *Mar Chem* 98:1–17. <https://doi.org/10.1016/j.marchem.2005.06.001>
- Matos CRL, Berrêdo JF, Machado W, et al (2020) Carbon and nutrient accumulation in tropical mangrove creeks, Amazon region. *Mar Geol* 429:. <https://doi.org/10.1016/j.margeo.2020.106317>
- Meiggs D, Taillefert M (2011) The effect of riverine discharge on biogeochemical processes in estuarine sediments. *Limnol Oceanogr* 56:1797–1810. <https://doi.org/10.4319/lo.2011.56.5.1797>
- Naik R, Araujo J, Pratihary A, et al (2019) Sedimentary sulphate reduction and organic matter mineralization across salinity gradient of the Mandovi Estuary, West coast of India. *Estuar Coast Shelf Sci* 221:21–29. <https://doi.org/10.1016/j.ecss.2019.03.005>
- Nascimento WR, Wal P, Proisy C, Lucas RM (2013) Estuarine , Coastal and Shelf Science Mapping changes in the largest continuous Amazonian mangrove belt using object-based classification of multisensor satellite imagery. *Estuar Coast Shelf Sci* 117:83–93. <https://doi.org/10.1016/j.ecss.2012.10.005>
- Otero XL, Macias F (2003) Spatial variation in pyritization of trace metals in salt-marsh soils. *Biogeochemistry* 62:59–86. <https://doi.org/10.1023/A:1021115211165>
- Ovalle ARC, Rezende CE, Lacerda LD, Silva CAR (1990) Factors affecting the hydrochemistry of a mangrove tidal creek, sepetiba bay, Brazil. *Estuar Coast Shelf Sci* 31:639–650. [https://doi.org/10.1016/0272-7714\(90\)90017-L](https://doi.org/10.1016/0272-7714(90)90017-L)
- Pan F, Liu H, Guo Z, et al (2019) Effects of tide and season changes on the iron-sulfur-phosphorus biogeochemistry in sediment porewater of a mangrove coast. *J Hydrol* 568:686–702. <https://doi.org/10.1016/j.jhydrol.2018.11.002>
- Paul JT, Ramaiah N, Sardessai S (2008) Nutrient regimes and their effect on distribution of phytoplankton in the Bay of Bengal. *Mar Environ Res* 66:337–344. <https://doi.org/10.1016/j.marenvres.2008.05.007>
- Raiswell R, Canfield DE (1998) Sources of iron for pyrite formation in marine sediments. *Am J Sci* 298:219–245. <https://doi.org/10.2475/ajs.298.3.219>
- Rao K, Priya N, Ramanathan AL (2018) Impact of seasonality on the nutrient concentrations in Gautami-Godavari Estuarine Mangrove Complex, Andhra Pradesh, India. *Mar Pollut*

- Bull 129:329–335. <https://doi.org/10.1016/j.marpolbul.2018.02.052>
- Reithmaier GMS, Johnston SG, Junginger T, et al (2020) Alkalinity production coupled to pyrite formation represents an unaccounted blue carbon sink Key Points
- Sanders CJ, Eyre BD, Santos IR, et al (2014) Impacted mangrove wetland. *Geophys Res Lett* 2475–2480. <https://doi.org/10.1002/2014GL059789>. Received
- Sanders CJ, Santos IR, Maher DT, et al (2015) Dissolved iron exports from an estuary surrounded by coastal wetlands: Can small estuaries be a significant source of Fe to the ocean? *Mar Chem* 176:75–82. <https://doi.org/10.1016/j.marchem.2015.07.009>
- Santos-Echeandia J, Prego R, Cobelo-García A, Millward GE (2009) Porewater geochemistry in a Galician Ria (NW Iberian Peninsula): Implications for benthic fluxes of dissolved trace elements (Co, Cu, Ni, Pb, V, Zn). *Mar Chem* 117:77–87.  
<https://doi.org/10.1016/j.marchem.2009.05.001>
- Seeberg-Elverfeldt J, Schlüter M, Feseker T, Kölling M (2005) Rhizon sampling of porewaters near the sediment-water interface of aquatic systems. *Limnol Oceanogr Methods* 3:361–371. <https://doi.org/10.4319/lom.2005.3.361>
- Sherman RE, Fahey TJ, Howarth RW (1998) Soil-plant interactions in a neotropical mangrove forest: iron, phosphorus and sulfur dynamics. *Oecologia* 115:553–563.  
<https://doi.org/10.1007/s004420050553>
- Silva CA da, Souza-Filho PWM, Rodrigues SWP (2009) Morphology and modern sedimentary deposits of the macrotidal Marapanim Estuary (Amazon, Brazil). *Cont Shelf Res* 29:619–631. <https://doi.org/10.1016/j.csr.2008.09.018>
- Taillardat P, Willemsen P, Marchand C, et al (2018) Assessing the contribution of porewater discharge in carbon export and CO<sub>2</sub> evasion in a mangrove tidal creek (Can Gio, Vietnam). *J Hydrol* 563:303–318. <https://doi.org/10.1016/j.jhydrol.2018.05.042>
- Taillardat P, Ziegler AD, Friess DA, et al (2019a) Assessing nutrient dynamics in mangrove porewater and adjacent tidal creek using nitrate dual-stable isotopes: A new approach to challenge the Outwelling Hypothesis? *Mar Chem* 214:103662.  
<https://doi.org/10.1016/j.marchem.2019.103662>
- Taillardat P, Ziegler AD, Friess DA, et al (2019b) Assessing nutrient dynamics in mangrove porewater and adjacent tidal creek using nitrate dual-stable isotopes: A new approach to challenge the Outwelling Hypothesis? *Mar Chem* 214:103662.  
<https://doi.org/10.1016/j.marchem.2019.103662>
- Tait DR, Maher DT, Sanders CJ, Santos IR (2017) Radium-derived porewater exchange and dissolved N and P fluxes in mangroves. *Geochim Cosmochim Acta* 200:295–309.

- <https://doi.org/10.1016/j.gca.2016.12.024>
- Thamdrup B, Fossing H, Jørgensen BB (1994) Manganese, iron and sulfur cycling in a coastal marine sediment, Aarhus bay, Denmark. *Geochim Cosmochim Acta* 58:5115–5129. [https://doi.org/10.1016/0016-7037\(94\)90298-4](https://doi.org/10.1016/0016-7037(94)90298-4)
- Thanh-Nho N, Marchand C, Strady E, et al (2019) Metals geochemistry and ecological risk assessment in a tropical mangrove (Can Gio, Vietnam). *Chemosphere* 219:365–382. <https://doi.org/10.1016/j.chemosphere.2018.11.163>
- Vilhena MDPSP, Costa ML Da, Berrêdo JF (2010) Continental and marine contributions to formation of mangrove sediments in an Eastern Amazonian mudplain: The case of the Marapanim Estuary. *J South Am Earth Sci* 29:427–438. <https://doi.org/10.1016/j.jsames.2009.07.005>
- Webb JR, Santos IR, Maher DT, et al (2019) Groundwater as a source of dissolved organic matter to coastal waters: Insights from radon and CDOM observations in 12 shallow coastal systems. *Limnol Oceanogr* 64:182–196. <https://doi.org/10.1002/lno.11028>
- Weston NB, Porubsky WP, Samarkin VA, et al (2006) Porewater stoichiometry of terminal metabolic products, sulfate, and dissolved organic carbon and nitrogen in estuarine intertidal creek-bank sediments. *Biogeochemistry* 77:375–408. <https://doi.org/10.1007/s10533-005-1640-1>
- Wu Z, Zhou H, Ren D, et al (2015) Processes controlling the seasonal and spatial variations in sulfate profiles in the pore water of the sediments surrounding Qi’ao Island, Pearl River Estuary, Southern China. *Cont Shelf Res* 98:26–35. <https://doi.org/10.1016/j.csr.2015.02.001>
- Yasui S, Kanda J, Usui T, Ogawa H (2016) Seasonal variations of dissolved organic matter and nutrients in sediment pore water in the inner part of Tokyo Bay. *J Oceanogr* 72:851–866. <https://doi.org/10.1007/s10872-016-0382-0>

## 7 CONCLUSÕES

Este estudo avaliou o potencial dos sedimentos de canais de maré de manguezais em acumular e exportar carbono, nutrientes (N e P), e metais (Fe e Mn), além de avaliar a influência dos padrões sazonais de chuva nas propriedades físico-químicas, nos processos diagenéticos e nos fluxos de nutrientes e metais na interface sedimento-água (IAS), em três sedimentos de canais de maré de manguezais de Marapanim, localizados no norte do Brasil. Houve uma mudança sazonal para condições mais ácidas e mais redutoras, um declínio na salinidade da água intersticial e um aumento na concentração da maioria dos elementos na água intersticial e sedimentos, da estação de estiagem para a chuvosa. Esta mudança foi provavelmente devido à infiltração e diluição da água da chuva na maré baixa e pelas águas das marés diluídas pelo aumento do escoamento de água doce. A variabilidade sazonal na precipitação causou fortes mudanças sazonais, especialmente na camada superficial superior, que chamamos neste trabalho de zona de mistura-diluição.

Nos três pontos de amostragem, a diminuição com a profundidade de TOC, pH e Eh, em paralelo com o aumento das concentrações TA,  $\text{SO}_4^{2-\text{dep}}$ ,  $\text{NH}_4^+$  and  $\text{PO}_4^{3-}$  na água intersticial refletiu diretamente a mineralização da MO durante o soterramento e as reações redox resultantes. Na zona de mistura-diluição, a redução de Fe (III) e Mn (IV) são os processos respiratórios anaeróbicos dominantes nos sedimentos. O zoneamento redox de sedimentos oscilou em resposta ao padrão de chuva, com maiores concentrações de  $\text{Fe}^{2+}$  e  $\text{Mn}^{2+}$  em uma posição vertical mais profunda na estação seca. Na estação chuvosa, a maior concentração de  $\text{Fe}^{2+}$  e  $\text{Mn}^{2+}$  foi encontrada logo abaixo da IAS, o que gerou fluxos maiores neste período. Na estação seca, a precipitação de oxi-hidróxidos de Fe e Mn nos sedimentos superficiais limitou sua difusão para a coluna d'água. Abaixo da mistura de diluição, a redução de sulfato (SR) foi aumentada significativamente. As concentrações de  $\text{NH}_4^+$  e  $\text{PO}_4^{3-}$  nos perfis de água intersticial estão relacionadas principalmente à mineralização da MO via SR. Entre os produtos da SR (TA,  $\text{NH}_4^+$  e  $\text{PO}_4^{3-}$ ), apenas o  $\text{NH}_4^+$  apresentou variabilidade sazonal na água intersticial, com maiores concentrações durante a estação chuvosa.

As variações entre os pontos de amostragem são principalmente relacionadas às fontes de MO, condições sedimentares, topografia e a susceptibilidade de degradação da MO. O sedimento do canal de maré na margem do rio Marapanim (P1) caracterizado por MO mais lável disponível e com alto teor de areia apresentou menores concentrações, acúmulo e estoque de COT, NT e PT, e alcançou maiores concentrações dos produtos metabólicos terminais da mineralização da MO, como TA,  $\text{SO}_4^{2-\text{dep}}$ ,  $\text{NH}_4^+$  e  $\text{PO}_4^{3-}$ , que sugerem que a MO dessa planície

lamosa é mais suscetível à decomposição em comparação com a MO dos sedimentos de canais de manguezais (P2 e P3), embora as maiores concentrações de  $\text{NH}_4^+$  e  $\text{PO}_4^{3-}$  na água intersticial tenham sido encontradas no canal de manguezal P2, o local com maior concentração de TOC.

A variabilidade temporal na formação da pirita revelou que os mecanismos de retenção da fase sólida também são suscetíveis a efeitos sazonais, com menores concentrações de enxofre redutível ao cromo (CRS, principalmente fração pirita) durante a estação seca. Os locais P2 e P3 localizados em áreas topograficamente mais elevadas foram mais suscetíveis a perdas nas concentrações de pirita durante a estação seca. A variação sazonal também influenciou na concentração das fases reativas de Fe e Mn, com concentrações mais altas durante a estação chuvosa, provavelmente porque o aumento da chuva impulsiona as taxas de intemperismo e transporte de sedimentos e, portanto, influencia o fornecimento de ferro e manganês reativos das bacias circunvizinhas.

Sob condições subóxicas, os sedimentos atuam como uma fonte de  $\text{Fe}^{2+}$ ,  $\text{Mn}^{2+}$ ,  $\text{NH}_4^+$  e  $\text{PO}_4^{3-}$  para a coluna de água, com fluxos mais altos durante a estação chuvosa. Os fluxos difusivos de  $\text{NH}_4^+$  ( $90$  a  $1433 \mu\text{mol m}^{-2} \text{d}^{-1}$ ),  $\text{PO}_4^{3-}$  ( $2$  a  $35 \mu\text{mol m}^{-2} \text{d}^{-1}$ ), Fe ( $6$  a  $723 \mu\text{mol m}^{-2} \text{d}^{-1}$ ) e Mn ( $16$  a  $189 \mu\text{mol m}^{-2} \text{d}^{-1}$ ) correspondem a  $16\%$ ,  $16\%$ ,  $15\%$  e  $90\%$  da deposição de N, P, Fe e Mn nos sedimentos, respectivamente, isto é, os sedimentos dos canais de maré dos manguezais de Marapanim são bastante eficazes na retenção de nutrientes e ferro do que na exportação para as águas costeiras, enquanto contribuem significativamente para o ciclo oceânico de Mn. As taxas de acúmulo de carbono orgânico encontradas nesses sedimentos foram ligeiramente mais altas do que as médias globais estimadas para dentro das florestas de manguezal, sugerindo que esses ambientes não impactados antropicamente são sumidouros de carbono (não contabilizados) relevantes em termos de orçamentos de carbono em zonas costeiras colonizadas por manguezais e tem potencial de ser um local modelo de pesquisa com carbono azul.

Portanto, este trabalho conclui que a variabilidade das precipitações implicou em mudanças substanciais nas propriedades físico-químicas e nos processos diagenéticos, afetando a liberação de metais e nutrientes na IAS e o acúmulo deles no sedimento. Essas descobertas evidenciaram o papel dos canais de maré de manguezais como reatores biogeoquímicos, em vez de simples condutos de metais e nutrientes dissolvidos entre os manguezais e o oceano costeiro.

## REFERÊNCIAS

- Adame M.F., Virdis B., Lovelock C.E. 2010. Effect of geomorphological setting and rainfall on nutrient exchange in mangroves during tidal inundation. *Mar. Freshw. Res.* **61**:1197–1206.
- AgisoftPhotoScan 2018. AgiSoft PhotoScan Professional. Version 1.4.5. *Agisoft LLC*, St. Petersburg, Russia Retrieved from.
- Alongi D.M. 1995. Decomposition and recycling of organic matter in muds of the Gulf of Papua, northern Coral Sea. *Cont. Shelf Res.*, **15**:1319–1337.
- Alongi D.M. 2014. Carbon Cycling and Storage in Mangrove Forests. *Annu. Rev. Mar. Sci.* **6**:195–219.
- Alongi D.M. 2020. Global Significance of Mangrove Blue Carbon in Climate Change Mitigation (Version 1). *Sci*, **2**(57):1–15.
- Alongi D.M., Pfitzner J., Trott L.A., Tirendi F., Dixon P., Klumpp D.W. 2005. Rapid sediment accumulation and microbial mineralization in forests of the mangrove Kandelia candel in the Jiulongjiang Estuary, China. *Estuarine. Coast. Shelf Sci.*, **63**:605–618.
- Alongi D.M., Sasekumar A., Chong V.C., Pfitzner J., Trott L.A., Tirendi F. 2004. Sediment accumulation and organic material flux in a managed mangrove ecosystem: estimates of land-ocean-atmosphere exchange in peninsular Malaysia. *Mar. Geol.* **208**:383–402.
- Alongi D.M., Wattayakorn G., Pfitzner J., Tirendi F., Zagorskis I., Brunskill G.J., Davidson A., Clough B.F. 2001. Organic carbon accumulation and metabolic pathways in sediments of mangrove forests in southern Thailand. *Mar. Geol.*, **179**:85–103.
- Anschutz P., Dedieu K., Desmazes F., Chaillou G. 2005. Speciation, oxidation state, and reactivity of particulate manganese in marine sediments. *Chem. Geol.*, **218**:265–279.
- APHA/AWWA/WEF: Standard Methods for the Examination of Water and Wastewater, 21st. Ed., USA, APHA, 2006.
- Appleby P.G. & Oldfield F. 1992. Application of lead-210 to sedimentation studies. In: Ivanovich M., Harmo, S. (Eds.). *Uranium Series Disequilibrium: Application to Earth, Marine and Environmental Science*, second ed. Oxford Science Publications, p. 731-783.
- Arias-Ortiz A., Masqué P., Garcia-Orellana J., Serrano O., Mazarrasa I., Marbà N., Lovelock C.E., Lavery P.S., Duarte C.M. 2018. Reviews and syntheses:  $^{210}\text{Pb}$ -derived sediment and carbon accumulation rates in vegetated coastal ecosystems – setting the record straight. *Biogeosciences*, **15**: 6791–6818.
- Aspila K.L., Agemian H., Chau A.S.Y. 1976. A semi-automated method for the determination of inorganic, organic and total phosphate in sediments. *Analyst*, **101**:187–197.
- Bayen S. 2012. Occurrence, bioavailability and toxic effects of trace metals and organic contaminants in mangrove ecosystems: a review. *Environ. Int.*, **48**:84–101.

Berrêdo J.F. 2006. *Geoquímica dos sedimentos de manguezais do nordeste do Estado do Pará: O exemplo do estuário do rio Marapanim*. Universidade Federal do Pará, Centro de Geociências (Tese de Doutorado), 185p.

Berrêdo J.F., Costa M.L., Vilhena M.S.P., Santos J.T. 2008. Mineralogia e geoquímica de sedimentos de manguezais da costa amazônica: o exemplo do estuário do rio Marapanim (Pará). *Revista Brasileira de Geociências*, **38**(1):24-35.

Berrêdo J.F., Costa M.L., Vilhena M.S.P., Matos C.R.L. 2016. Modificações nas propriedades físico-químicas de sedimentos de manguezais submetidos ao clima amazônico. *Bol. Mus. Para. Emílio Goeldi. Cienc. Nat.*, Belém, **11**(3): 313-328.

Berner R.A. 1980. *Early Dogenesis*. Princeton University Press, Princeton, 241p.

Berner R.A. 1984. Sedimentary pyrite formation—an Update. *Geochim. Cosmochim. Acta* **48**:605–615.

Blott S.J. & Pye K. 2001. GRADISTAT: a grain size distribution and statistics package for the analysis of unconsolidated sediments. *Earth Surf. Process. Landf.*, **26**:1237–1248.

Bouillon S., Middelburg J.J., Dehairs F., Borges A.V., Abril G., Flindt M.R., Ulomi S., Kristensen E. 2007. Importance of intertidal sediment processes and porewater exchange on the water column biogeochemistry in a pristine mangrove creek (Ras Dege, Tanzania). *Biogeosciences*, **4**:311–322.

Bouillon S., Borges A.V., Castañeda-Moya E., Diele K., Dittmar T., Duke N.C., Kristensen E., Lee S.Y., Marchand C., Middelburg J.J., Rivera-Monroy V.H., Smith T.J., Twilley R.R. 2008. Mangrove production and carbon sinks: A revision of global budget estimates. *Global Biogeochem. Cycles* 22.

Breithaupt J.L., Smoak J.M., Smith T.J., Sanders C.J. 2014. Temporal variability of carbon and nutrient burial, sediment accretion, and mass accumulation over the past century in a carbonate platform mangrove forest of the Florida Everglades. *J. Geophys. Res. Biogeosci.*, **119**.

Canfeld D.E. 1994. Factors influencing organic carbon preservation in marine sediments. *Chem. Geol.*, **114**(3–4):315–329.

Call M., Santos I.R., Dittmar T., de Rezende C.E., Asp N.E., Maher D.T. 2019. High pore-water derived CO<sub>2</sub> and CH<sub>4</sub> emissions from a macro-tidal mangrove creek in the Amazon region. *Geochim. Cosmochim. Acta*, **247**:106–120.

Cline J.D. 1969. Spectrophotometric determination of hydrogen sulfide in natural waters. *Limnology and Oceanography*, **14**:454-458.

Cohen M.C.L., de Souza A.V., Rossetti D.F., Pessenda L.C.R., França, M.C. 2018. Decadal-scale dynamics of an Amazonian mangrove caused by climate and sea level changes: inferences from spatial-temporal analysis and Digital Elevation Models. *Earth Surf. Process. Landf.*, **43**:2876–2888.

Cohen M.C.L., Figueiredo B.L., Oliveira N.N., Fontes N.A., França M.C., Pessenda L.C.R., Lima P. 2019. Impacts of Holocene and modern sea-level changes on estuarine mangroves from Northeastern Brazil. *Earth Surf. Process. Landf.*, esp.4737.

Deborde J., Marchand C., Molnar N., Patrona L.D., Meziane T. 2015. Concentrations and fractionation of carbon, iron, sulfur, nitrogen and phosphorus in mangrove sediments along an intertidal gradient (semi-arid climate, New Caledonia). *Journal of Marine science and Engineering*, **3**:52-72.

Deines P. 1980. The isotopic composition of reduced organic carbon. In: Fritz P., Fontes J.C. (eds.). *Handbook of Environmental Isotope Geochemistry. The Terrestrial Environment.*, 1., A. Elsevier, Amsterdam, p. 329–406.

Ding H., Yao S., Chen J. 2014. Authigenic pyrite formation and re-oxidation as an indicator of an unsteady-state redox sedimentary environment: Evidence from the intertidal mangrove sediments of Hainan Island, China. *Continental Shelf Research*, **78**:85-89.

Dittmar T., Hertkorn N., Kattner G., Lara R.J. 2006. Mangroves, a major source of dissolved organic carbon to the oceans. *Global Biogeochemical Cycles*, **20**:1–7.

Feller I.C., McKee K.L., Whigham D.F., O'Neill J.P. 2003. Nitrogen vs. phosphorus limitation across an ecotonal gradient in a mangrove forest. *Biogeochemistry*, **62**:145-175.

Fernandes M.E.B., Oliveira F.P., Eyzaguirre I.A.L. 2018. Mangroves on the Brazilian Amazon coast: Uses and rehabilitation. In: Makowski, C., Finkl, C. (Eds.), Threats to Mangrove Forests. Coastal Research Library., 25, Springer, Cham.

Fernandes S.O., Bonin P.C., Michotey V.D., Garcia N., LokaBharathi P. 2012. Nitrogen-limited mangrove ecosystems conserve N through dissimilatory nitrate reduction to ammonium. *Scientific reports*, **2**:419.

Ferreira T.O., Otero X.L., Vidal-Torras P., Macias F. 2007. Effects of bioturbation by root and crab activity on iron and sulfur biogeochemistry in mangrove substrate. *Geoderma*, **142**:36–46.

Froelich P.N., Klinkhammer G.P., Bender M.L., Luedtke N.A., Heath G.R., Cullen D., Dauphin P., Hammond D., Hartman B., Maynard V. 1979. Early oxidation of organic matter in pelagic sediments of the eastern equatorial Atlantic: Suboxic diagenesis. *Geochim. Cosmochim. Acta*, **43**:1075-1090.

Gieskes J.M., Gamo T., Brumsack H. 1991. *Chemical Methods for Intersitital Water Analysis aboard JOIDES Resolution*, ODP Technical Note 15. Texas A & M University, p.24-49.

Gleeson J., Santos I.R., Maher D.T., Golsby-Smith L. 2013. Groundwater-surface water exchange in a mangrove tidal creek: Evidence from natural geochemical tracers and implications for nutrient budgets. *Marine Chemistry*, **156**:27-37.

GlobalMapper 2017. (Version 19). Blue Marble Geographics. Hallowell, Maine, United State.

Glud R.N. 2008. Oxygen dynamics of marine sediments. *Mar. Biol. Res.*, **4**:243–289.

Gran G. Determination of the equivalent point in potentiometric titrations. Part II *Analyst* **77**: 661–671.

Goldhaber M.B., Kaplan I.R. 1974. The sulfur cycle. In: Goldberg ED (ed.). *The sea*, 5. Wiley, New York, p. 569–655.

Goldhaber M.B. 2004. Sulfur-rich sediments. In: Mackenzie, F.T. (Ed.), Sediments, diagenesis, and sedimentary rocks. *Treatise on Geochemistry*. Elsevier, Amsterdam, p. 257–288.

Gomes V.J.C., Freitas, P.T.A.; Asp, N.E. 2013. Dynamics and seasonality of the midle sector of a macrotidal estuaries. *Journal of Coastal Research*, Special Issue: 1140–1145.

Grenz C., Denis L., Pringault O., Fichez R. 2010. Spatial and seasonal variability of sediment oxygen consumption and nutrient fluxes at the sediment water interface in a sub-tropical lagoon (New Caledonia). *Mar. Pollut. Bull.*, **61**:399–412.

Glud R.N. 2008. Oxygen dynamics of marine sediments. *Mar. Biol. Res.*, **4**:243–289.

Hedges J.I., Keil R.G., Benner R. 1997. What happens to terrestrial organic matter in the ocean? *Org. Geochem.*, **27**: 195–212.

Henrichs S.M. 1992. Early diagenesis of organic matter in marine sediments: progress and perplexity. *Mar. Chem.*, **39**:119–149.

Holmer M. Kristensen E., Banta G., Hansen K., Jensen M.H., Bussawarit N. 1994. Biogeochemical cycling of sulfur and iron in sediments of a South-East Asian Mangrove, Phuket Island, Thailand. *Biogeochemistry*, **26**:145–161.

Hammer O., Harper D.A.T., Ryan P.D. 2001. PAST: paleontological statistics software package for education and data analysis. *Palaeontol. Electron.*, **4**(1):9.

Holloway C.J., Santos I.R., Tait D.R., Sander C.J., Rose A.L., Schnetger B., Brumsack H-J., Macklin P.A., Sippo J.Z., Maher D.T. 2016. Manganese and iron release from mangrove porewaters: A significant component of oceanic budgets? *Mar. Chem.*, **184**:43–52.

Holmer M, Kristensen E, Banta G, Hansen K, Jensen MH, Bussawarit N. 1994. Biogeochemical cycling of sulfur and iron in sediments of a south-east Asian mangrove, Phuket Island, Thailand. *Biogeochemistry*, **26**:145-161.

Howard J., Hoyt S., Isensee K., Pidgeon E., Telszewski M. 2014. Coastal Blue Carbon: Methods for Assessing Carbon Stocks and Emissions Factors in Mangroves, Tidal Salt Marshes, and Seagrass Meadows, Conserv. Int. Intergov. Oceanogr. Comm. UNESCO, Int. Union Conserv. Nature, Arlington, Virginia, USA. p. 1–180.

ICMBio 2018. *Atlas dos Manguezais do Brasil*. 1st ed. Instituto Chico Mendes de Conservação da Biodiversidade, Brasília.

Jennerjahn T.C., Ittekkot V. 2002. Relevance of mangroves for the production and deposition of organic matter along tropical continental margins, *Naturwissenschaften*, **89**:23–30.

- Kaiser D., Kowalski N., Böttcher M.E., Yan B., Unger D. 2015. Benthic Nutrient Fluxes from Mangrove Sediments of an Anthropogenically Impacted Estuary in Southern China. *J. Mar. Sci. Eng.*, **3**:466–491.
- Kauffman J.B., Bernardino A.F., Ferreira T.O., Giovannoni L.R., De Gomes L.E.O., Romero D.J., Jimenez L.C.Z., Ruiz F. 2018. Carbon stocks of mangroves and salt marshes of the Amazon region, *Brazil. Biol. Lett.*, **14**.
- Kjerve B., Lacerda L.D. 1993. Mangroves of Brazil. In: Conservation and Sustainable Utilization of Mangrove Forests in Latin America and Africa Regions. Part 1: Latin America. ITTO/ISME Project PD114/90(F), p. 245–272.
- Kostka J.E., Luther G.W. 1994. Partitioning and speciation of solid phase iron in saltmarsh sediments. *Geochim. Cosmochim. Acta*, **58**:1701–1710.
- Kristensen E. 2008. Mangrove crabs as ecosystem engineers; with emphasis on sediment processes. *J. Sea Res.*, **59**:30–43.
- Kristensen E., Alongi D.M. 2006. Control by fiddler crabs (*Uca vocans*) and plant roots (*Avicennia marina*) on carbon, iron, and sulfur biogeochemistry in mangrove sediment. *Limnol. Oceanogr.*, **51**:1557–1571.
- Kristensen E., Devol A.H., Ahmed S.I., Saleem M. 1992. Preliminary study of benthic metabolism and sulfate reduction in a mangrove swamp of the Indus Delta, Pakistan. *Marine Ecology Progress Series*, **90**:287–297.
- Kristensen E., Holmer M., Bussawarit, N. 1991. Benthic metabolism and sulfate reduction in a south-east Asian mangrove swamp. *Marine Ecology Progress Series*, **73**:93–103.
- Kristensen E., King G., Holmer M., et al. 1994. Sulfate reduction, acetate turnover and carbon metabolism in sediments of the Ao Nam Bor mangrove, Phuket, Thailand. *Mar. Ecol. Prog. Ser.*, **111**:245–255.
- Kristensen E., Mangion P., Tang M., Flindt M.R., Holmer M., Ulomi S. 2011. Microbial carbon oxidation rates and pathways in sediments of two Tanzanian mangrove forests. *Biogeochemistry*, **103**:143–158.
- Ku T.C.W., Kay J., Browne E., Martini A.M., Peters S.C., Chen M.D. 2008. Pyritization of iron in tropical coastal sediments: Implications for the development of iron, sulfur, and carbon diagenetic properties, Saint Lucia, Lesser Antilles. *Mar. Geol.*, **249**:184–205.
- Kusumaningtyasa M.A., Hutahaean A.A., Fischer H.W., Mayod M.P., Ransby D., Jennerjahn T.C. 2019. Variability in the organic carbon stocks, sources, and accumulation rates of Indonesian mangrove ecosystems. *Estuar. Coast. Shelf Sci.*, **218**:310–323.
- Lamb A.L., Wilson G.P., Leng M.J. 2006. A review of coastal palaeoclimate and relative sea-level reconstructions using  $\delta^{13}\text{C}$  and C/N ratios in organic material. *Earth-Sci. Rev.*, **75**:29–57.

- Lee R.Y., Porubsky W.P., Feller I.C., McKee K.L., Joye S.B. 2008. Porewater biogeochemistry and soil metabolism in dwarf red mangrove habitats (Twin Cays, Belize). *Biogeochemistry*, **87**: 181–198.
- Leopold A., Marchand C., Deborde J., Chaduteau C., Allenbach M. 2013. Influence of mangrove zonation on CO<sub>2</sub> fluxes at the sediment–air interface (New Caledonia). *Geoderma*, **202–203**:62–70.
- Lewis M., Pryor R., Wilking L. 2011. Fate and effects of anthropogenic chemicals in mangrove ecosystems: a review. *Environ. Pollut.*, **159**: 2328–2346.
- Li Y.-H., Gregory S. 1974. Diffusion of ions in sea water and in deep-sea sediments. *Geochim. Cosmochim. Acta*, **38**:703–714.
- Liu D., Li X., Emeis K.C., Wang Y., Richard P. 2015. Distribution and sources of organic matter in surface sediments of Bohai Sea near the Yellow River Estuary, China. *Estuar. Coast. Shelf Sci.*, **165**: 128–136.
- Machado W., Silva-Filho E.V., Oliveira R.R., Lacerda L.D. 2002. Trace metal retention in mangrove ecosystems in Guanabara Bay, SE Brazil. *Mar. Pollut. Bull.*, **44**: 1277–1280.
- Maher D.T., Sippo J.Z., Tait D.R., Holloway C., Santos I.R. 2016. Pristine mangrove creek waters are a sink of nitrous oxide. *Scientific Reports*, **6**.
- Marchand C., Baltzer F., Lallier-Vergès E., Albéric P. 2004. Pore-water chemistry in mangrove sediments: Relationship with species composition and developmental stages (French Guiana). *Mar. Geol.*, **208**: 361–381.
- Marchio D., Savarese M., Bovard B., Mitsch W. 2016. Carbon sequestration and sedimentation in mangrove swamps influenced by hydrogeomorphic conditions and urbanization in Southwest Florida. *Forests*, **7**(12):116.
- Matos C.R.L., Berrêdo J.F., Machado W., Sanders C.J., Metzger E., Cohen M.C.L. 2020. Carbon and nutrient accumulation in tropical mangrove creeks, Amazon region. *Mar. Geol.*, **429**.
- Matos C.R.L., Mendoza U., Diaz R., Moreira M., Belem A.L., Metzger E., Albuquerque A.L.S., Machado W. 2016. Nutrient regeneration susceptibility under contrasting sedimentary conditions from the Rio de Janeiro coast, Brazil. *Mar. Pollut. Bull.*, **108**.
- Marchand C., Lallier-Vergès E., Allenbach M. 2011. Redox conditions and heavy metals distribution in mangrove forests receiving effluents from shrimp farms (Teremba Bay, New Caledonia). *J Soils Sediments*, **11**:529–541.
- Martorano L.G., Pereira L.C., Cezar E.G.M. Pereira I.C.B. 1993. Estudos climáticos do Estado do Pará, classificação climática (Köppen) e deficiência hídrica (Thornthwhite, Mather). Belém, SUDAM/EMBRAPA, SNLCS, 53p.

- Mcleod E., Chmura G.L., Bouillon S., Salm R., Bjork M., Duarte C.M., Lovelock C.E., Schlesinger, W.H. Silliman B.R. 2011. A blueprint for blue carbon: toward an improved understanding of the role of vegetated coastal habitats in sequestering CO<sub>2</sub>. *Front. Ecol. Environ.*, **9**:552–60.
- Meiggs D., Taillefert M. 2011. The effect of riverine discharge on biogeochemical processes in estuarine sediments. *Limnol. Oceanogr.*, **56**:1797–1810.
- Meyers P.A. 1997. Organic geochemical proxies of paleoceanographic, paleolimnologic, and paleoclimatic processes. *Org. Geochem.*, **27**:213–250.
- Meyers P.A. 2003. Applications of organic geochemistry to paleolimnological reconstructions: a summary of examples from the Laurentian Great Lakes. *Org. Geochem.*, **34**:261–289.
- Morse J.W., Millero F.J., Cornwell J.C., Rickard D. 1987. The chemistry of hydrogen sulfide and iron sulfide systems in natural waters. *Earth-Science Reviews*, **24**:1–42.
- Moura, H.T.G.S., Nunes, Z.M.P. 2016. Caracterização sazonal das águas do sistema estuarino do Caeté (Bragança-PA). *Bol. Inst. Pesca*, **42**(4):844–854.
- Nascimento W.R., Wal P., Proisy C., Lucas R.M. 2013. Estuarine , Coastal and Shelf Science Mapping changes in the largest continuous Amazonian mangrove belt using object-based classification of multisensor satellite imagery. *Estuar. Coast. Shelf Sci.* **117**:83–93.
- Nellemann C., Corcoran E., Duarte C.M., Valdrés L., Young C.D., Fonseca L., Grimsditch G. 2009. *Blue Carbon - The Role of Healthy Oceans in Binding Carbon*. UN Environment, GRID-Arendal.
- Otero X.L., Macias F. 2002. Variation with depth and season in metal sulfides in salt marsh soils. *Biogeochemistry*, **61**:247–268.
- Ovalle A.R.C., Rezende C.E., Lacerda L.D., Silva C.A.R. 1990. Factors affecting the hydrochemistry of a mangrove tidal creek, sepetiba bay, Brazil. *Estuar. Coast. Shelf Sci.*, **31**:639–650.
- Pan F., Liu H., Guo Z., Li Z., Wang B., Cai Y., Gao A. 2019. Effects of tide and season changes on the iron-sulfur-phosphorus biogeochemistry in sediment porewater of a mangrove coast. *J. Hydrol.*, **568**:686–702.
- Paul J.T., Ramaiah N., Sardessai S. 2008. Nutrient regimes and their effect on distribution of phytoplankton in the Bay of Bengal. *Mar. Environ. Res.*, **66**:337–344.
- Pérez A., Libardoni B.G., Sanders C.J. 2018. Factors influencing organic carbon accumulation in mangrove ecosystems. *Biol. Lett.*, **14**(10).
- Peterson B.J., Howarth R.W. 1987. Sulfur, carbon, and nitrogen isotopes used to trace organic matter flow in the salt-marsh estuaries of Sapelo Island, Georgia. *Limnol. Oceanogr.*, **32**(6):1195–1213.

- Ranjan R.K., Routh J., Ramanathan A.L., Klump J.V. 2011. Elemental and stable isotope records of organic matter input and its fate in the Pichavaram mangrove–estuarine sediments (Tamil Nadu, India). *Mar. Chem.*, **126**:163–172.
- Rao K., Priya N., Ramanathan A.L. 2018. Impact of seasonality on the nutrient concentrations in Gautami-Godavari Estuarine Mangrove Complex, Andhra Pradesh, India. *Mar. Pollut. Bull.*, **129**:329–335.
- Rigaud S., Radakovitch O., Couture R.M., Deflandre B., Cossa D., Garnier C., Garnier J.M.. 2013. Mobility and fluxes of trace elements and nutrients at the sediment–water interface of a lagoon under contrasting water column oxygenation conditions. *Applied Geochemistry*, **31**:35–51.
- Rivera-Duarte I., Flegal A.R. 1997. Porewater gradients and diffusive benthic fluxes of Co, Ni, Cu, Zn, and Cd in San Francisco Bay. *Croatica Chemica Acta*, **70**(1):389–417.
- Rosentreter J.A., Maher D.T., Erler D.V., Murray R., Eyre B.D. 2018. Seasonal and temporal CO<sub>2</sub> dynamics in three tropical mangrove creeks – a revision of global mangrove CO<sub>2</sub> emissions. *Geochim. Cosmochim. Acta*, **222**: 729–745.
- Sanders C.J., Santos I.R., Barcellos R., Silva Filho E.V. 2012. Elevated concentrations of dissolved Ba, Fe and Mn in a mangrove subterranean estuary: consequence of sea level rise? *Cont. Shelf Res.*, **43**: 86–94.
- Sanders C.J., Eyre B.D., Santos I.R., Machado W., Luiz-silva W., Smoak J.M., Breithaupt J.L., Kettner M.E., Sanders L., Marotta H., Silva-Filho E. 2014. Elevated rates of organic carbon, nitrogen, and phosphorus accumulation in a highly impacted mangrove wetland. *Geophys. Res. Lett.*, **41**:2475–2480.
- Sanders C.J., Santos I. R., Maher D.T., Breithaupt J.L., Smoak J.M., Ketterer M., Call M., Luciana Sanders, Bradley D. Eyre. 2016 Examining <sup>239+240</sup>Pu, <sup>210</sup>Pb and historical events to determine carbon, nitrogen and phosphorus burial in mangrove sediments of Moreton Bay, Australia. *Journal of Environmental Radioactivity*, **151**:623-629.
- Sasmito S.D., Kuzyakov Y., Lubis A.A., Murdiyarso D., Hutley L.B., Bachri S., Friess D.A., Martius C., Borchard N. 2020. Organic carbon burial and sources in soils of coastal mudflat and mangrove ecosystems. *Catena*, **187**:104414.
- Schubert C.J., Ferdelman T.G., Strotmann B. 2000. Organic matter composition and sulfate reduction rates in sediments off Chile. *Org. Geochem.*, **31**(5):351–361
- Schultz D.J., Calder J.A. 1976. Organic carbono <sup>13</sup>C/<sup>12</sup>C variations in estuarine sediments. *Geochim. Cosmochim. Acta*, **40**:381–385.
- Seeberg-Elverfeldt J., Schlüter M., Feseker T., Kölling M. 2005. Rhizon in situ sampler (RISS) for pore water sampling from aquatic sediments. *Limnol. Oceanogr. Meth.*, **3**:361–371.
- Silva C.A. da, Souza-Filho P.W.M., Rodrigues S.W.P. 2009. Morphology and modern sedimentary deposits of the macrotidal Marapanim Estuary (Amazon, Brazil). *Cont. Shelf Res.* **29**:619–631.

- Sippo J.Z., Santos I.R., Sanders C.J., et al. 2020. Reconstructing extreme climatic and geochemical conditions during the largest natural mangrove dieback on record. *Biogeosciences*, **17**:4707–4726.
- Smoak J.M., Breithaupt J.L., Smith T.J., Sanders C.J. 2013. Sediment accretion and organic carbon burial relative to sea-level rise and storm events in two mangrove forests in Everglades National Park. *Catena*, **104**:58–66.
- Sunda W.G. 2002. In: Turner, D.R., Hunter, K.A. (Eds.), In: *The Biogeochemistry of Iron in Seawater*. Wiley, New York, p. 41–84.
- Taillardat P., Willemsen P., Marchand C., Friess D.A., David FW., Baudron P., Truong V.V., Nguyen T-N, Ziegler A.D. 2018. Assessing the contribution of porewater discharge in carbon export and CO<sub>2</sub> evasion in a mangrove tidal creek (Can Gio, Vietnam). *J. Hydrol.*, **563**:303–318.
- Taillardat P., Ziegler A.D., Friess D.A., Widory D., David F., Ohte N., Nakamura T., Evaristo J., Thanh-Nho N., Van Vinh T., Marchand C. 2019. Assessing nutrient dynamics in mangrove porewater and adjacent tidal creek using nitrate dual-stable isotopes: A new approach to challenge the Outwelling Hypothesis? *Mar. Chem.*, **214**:103662.
- Thanh-Nho N., Marchand C., Strady E., Vinh T-V., Nhu-Trang T-T. 2019. Metals geochemistry and ecological risk assessment in a tropical mangrove (Can Gio, Vietnam). *Chemosphere*, **219**:365–382.
- Twilley R.R., Rivera-Monroy V.H. 2009. Ecogeomorphic models of nutrient biogeochemistry for mangrove wetlands. Coastal wetlands: an integrated ecosystem approach. Elsevier, Amsterdam, 641-683.
- Udden J.A. 1914. Mechanical composition of clastic sediments. *Bull. Geol. Soc. Am.*, **25**:655–744.
- Vilhena M.P.S.P., Costa M.L., Berrêdo J.F. 2010. Continental and marine contributions to formation of mangrove sediments in an Eastern Amazonian mudplain: The case of the Marapanim Estuary. *Journal of South American Earth Sciences*, **29**:427–438.
- Vilhena M.P.S.P., Costa M.L., Berrêdo J.F., Paiva R.S., Moreira M.Z. 2018. The sources and accumulation of sedimentary organic matter in two estuaries in the Brazilian Northern coast. *Reg. Stud. Mar. Sci.*, **18**:188–196.
- Watanabe K. & Kuwae T. 2015. How organic carbon derived from multiple sources contributes to carbon sequestration processes in a shallow coastal system? *Glob. Chang. Biol.*, **21**:2612–2623.
- Webb J.R., Santos I.R., Maher D.T., Tait D.R., Cyronia T., Sadat-Noori M., Macklin P., Jeffrey L. C. 2019. Groundwater as a source of dissolved organic matter to coastal waters: Insights from radon and CDOM observations in 12 shallow coastal systems. *Limnol. Oceanogr.*, **64**:182–196.

- Wentworth C.K. 1922. A scale of grade and class terms for clastic sediments. *J. Geol.*, **30**:377–392.
- Wu Z., Zhou H., Ren D., Gao H., Li J. 2015. Processes controlling the seasonal and spatial variations in sulfate profiles in the pore water of the sediments surrounding Qi’ao Island, Pearl River Estuary, Southern China. *Cont. Shelf Res.*, **98**:26–35.
- Zonneveld K.A.F., Versteegh G.J.M., Kasten S., Eglinton T.I., Emeis K.-C., Huguet C., Koch B.P., de Lange G.J., de Leeuw J.W., Middelburg J.J., Mollenhauer G., Prahl F., Rethemeyer J., Wakeham S. 2010. Selective preservation of organic matter in marine environments; processes and impact on the fossil record. *Biogeosciences*, **7**:483–511.
- Yasui S., Kanda J., Usui T., Ogawa H. 2016. Seasonal variations of dissolved organic matter and nutrients in sediment pore water in the inner part of Tokyo Bay. *J. Oceanogr.*, **72**:851–866.



UNIVERSIDADE FEDERAL DO PARÁ  
INSTITUTO DE GEOCIÊNCIAS  
PROGRAMA DE PÓS-GRADUAÇÃO EM GEOLOGIA E GEOQUÍMICA

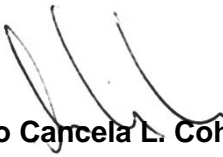
## PARECER

### Sobre a Defesa Pública da Tese de Doutorado de CHRISTIENE RAFAELA LUCAS DE MATOS

A banca examinadora da Tese de Doutorado de **CHRISTIENE RAFAELA LUCAS DE MATOS** orientanda do Prof. Dr. Marcelo Cancela L. Cohen (UFPA), composta pelos professores doutores **Paulo César Fonseca Giannini (Membro externo-USP)**, **Luiz Carlos Ruiz Pessenda (Membro externo-USP)**, **José Augusto Martins Corrêa (Membro interno-UFPA)**, **Nils Edvin Asp Neto (Membro interno-UFPA)**, após apresentação da sua tese intitulada “**ACÚMULO E EXPORTAÇÃO DE CARBONO, NITROGÊNIO, FÓSFORO E METAIS EM CANAIS DE MARÉ DOS MANGUEZAIS DE MARAPANIM, COSTA NORTE BRASILEIRA**”, emite o seguinte parecer:

A candidata realizou sua apresentação de forma clara, bem organizada e segura no tempo estipulado. O trabalho escrito foi apresentado na forma de dois artigos, sendo um já publicado e um submetido, ambos em periódicos de impacto internacional. Foram feitas sugestões variadas pela banca que foram acatadas pela candidata que as incorporará em seus futuros artigos. A banca destaca que a candidata demonstrou desempenho extraordinário durante o desenvolvimento da pesquisa bem como na arguição. Diante do exposto, a banca examinadora decide por unanimidade aprovar a tese de doutorado.

Belém, 18 de dezembro de 2020.

  
**Prof. Dr. Marcelo Cancela L. Cohen (Orientador – UFPA)**

  
**Prof. Dr. Paulo César Fonseca Giannini (Membro externo-USP)**

  
**Prof. Dr. Luiz Carlos Ruiz Pessenda (Membro externo-USP)**

  
**Prof. Dr. José Augusto Martins Corrêa (Membro interno-UFPA)**

  
**Prof. Dr. Nils Edvin Asp Neto (Membro interno-UFPA)**